Analyzing Electronic Correlation Effects in Molecules and Semiconductor Point Defects from First Principles Beyond Density Functional Theory

Anri Karanovich

Dissertation submitted to the Faculty of the
Virginia Polytechnic Institute and State University
in partial fulfillment of the requirements for the degree of

Doctor of Philosophy
in
Physics

Kyungwha Park, Chair
Nicholas Mayhall
Vito Scarola
Victoria Soghomonian

December 11, 2024
Blacksburg, Virginia

Keywords: Density Functional Theory, Electronic Structure, Electronic Correlation,
Self-Interaction Correction, Multireference Methods

Analyzing Electronic Correlation Effects in Molecules and Semiconductor Point Defects from First Principles Beyond Density Functional Theory

Anri Karanovich

(ABSTRACT)

Transition-metal based molecules and point defects in wide-bandgap semiconductors have been of particular interest lately due to their potential quantum information science applications. To accurately calculate the electronic properties of these systems from first principles, it is important to appropriately account for electronic correlation effects. Density functional theory (DFT) has been one of the most popular methods to perform calculations on correlated systems, due to the combination of numerical efficiency and precision in many applications. However, traditional DFT methods fail to accurately calculate the important electronic and magnetic properties, such as bandgaps in semiconductors or magnetic ordering in defects, to name a few. This dissertation focuses on two areas in which traditional DFT methods are likely to produce inaccurate predictions. The first area is connected to an error that is intrinsic to most DFT formulations due to the approximate nature of the exchange-correlation functional, known as the self-interaction error (SIE). It is known to cause the underestimation of bandgaps in solids, underestimated reaction barriers in molecules, and incorrect dissociation curves. The second area is the case where the ground and/or excited states are described by multiconfigurational wavefunctions rather than a single Slater determinant.

Chapter 1 of the thesis provides a brief overview of various electronic-structure methods, as well as the Fermi-Löwdin Orbital Self-Interaction Correction method (FLOSIC) which is used to remedy the SIE in DFT. Chapter 2 reports on the application of the FLOSIC-DFT on a Cu-based molecule, and its effects on the predicted electronic properties. Chapter 3 describes the application of the FLOSIC-DFT to the computation of the hyperfine coupling terms, which are crucial for the realization of spin qubits and for interpreting electron paramagnetic resonance experiments. Chapter 4 turns to the application of a multiconfigurational method to describe the electronic properties of a silicon vacancy in silicon carbide, a potential point-defect qubit.

Analyzing Electronic Correlation Effects in Molecules and Semiconductor Point Defects from First Principles Beyond Density Functional Theory

Anri Karanovich

(GENERAL AUDIENCE ABSTRACT)

Computational electronic structure methods, which attempt to predict optical, electronic, and other properties of molecules and materials just by solving the Schrödinger equation for the wavefunction of the electrons in them, have been instrumental in many areas of research, including the design of semiconductors, drug discovery, improved solar panel design, and discovering systems that can work as qubits for quantum-computing purposes, to name a few. One of the most successful sets of these methods, known as Density Functional Theory (DFT) methods, makes solving for electronic wavefunctions (and from them, other materials properties) computationally efficient, while maintaining the accuracy of such predictions by accounting for the complex quantum-mechanical interactions between the particles. For this, DFT was the subject of the 1998 Nobel Prize in chemistry. However, there are several areas where DFT is typically not successful in producing accurate predictions. One of the areas is connected to the approximated term in all DFT methods that often erroneously accounts for electrons interacting on themselves (an effect known as the self-interaction error). The other area is related to systems that must be described with superposition of several electronic configurations.

Chapter 1 of the thesis provides a brief overview of various electronic-structure methods, as well as the Fermi-Löwdin Orbital Self-Interaction Correction method (FLOSIC) which suggests a modification to the standard DFT methods that aims to remove the self-interaction

error. Chapter 2 reports on the application of the FLOSIC-DFT on a Cu-based molecule, and its effects on the predicted electronic properties. Chapter 3 describes the application of the FLOSIC-DFT to describe the interaction between the magnetic moments of electrons and nuclei, known as the hyperfine coupling, which is crucial for the realization of spin qubits and for interpreting some experimental results. Chapter 4 turns to the application of a multiconfigurational method to describe the electronic properties of a silicon vacancy in silicon carbide, a potential point-defect qubit.

Dedication

This dissertation is dedicated to my family and friends.

Acknowledgments

I am deeply indebted to my graduate supervisor, Prof. Kyungwha Park, for her tremendous help and support throughout the last 6.5 years of my academic journey. I consider myself lucky to have been mentored by someone who is this mindful, wise, understanding, and dedicated to the success of her advisees. The feedback and advice I received from her during our involved research discussions helped me gain the knowledge, discipline, and analytical skills that have made me the scientist I am today.

I also extend my gratitude to the other members of my graduate committee, Prof. Victoria Soghomonian, Prof. Vito Scarola, and Prof. Nicholas Mayhall, for dedicating their time and effort to checking my academic progress, for the insightful questions during the examinations, and for the careful review and constructive feedback for this dissertation. I also thank the graduate program director, Prof. Uwe Täuber, for his contribution to the review of this manuscript, as well as for the hard work ensuring that the Virginia Tech Physics Department is a great place to receive graduate education.

Most of the work presented in this dissertation could not have been done without the extensive help from our external collaborators. I thank Prof. Koblar Alan Jackson from Central Michigan University for providing us with invaluable insight into the principles of the FLOSIC method and for the generous help with using the software for the FLOSIC computations. I also thank Dr. Yoh Yamamoto from the University of Texas at El Paso for also dedicating his time to assisting me with the FLOSIC code.

I thank our former postdoctoral group members, Dr. Aleksander Wysocki, Dr. Karolina Janicka, Dr. Kamal Wagle, and Dr. Churna Bhandari, for their help with other software I needed for my work and for the informal but thoughtful discussions that helped me broaden

my understanding of the methods and subjects of my research.

I am thankful to Betty Wilkins, Jacqueline Woodyard, Katrina Lockhart-Elfeky, Savannah Merrix, and other members of the Physics Department's administrative staff for all their help with administrative work, making it much easier for me to focus on my research and studies. I also thank Roger Link and Travis Heath for all their help with the IT related issues, which was essential to my work as a computational scientist.

I thank all the friends and colleagues that I have had a pleasure to know during my years in Blacksburg: Liev Birman, Doyee Byun, Joseph Camilleri, Garv Chauhan, Luis A. Delgadillo, Sohair Elmeligy, Peter Gartin, Homa Karimi, Vladislav Kokushkin, Olga Kyzylova, Tommy Lam, Varun Mathur, Ruslan Mukhamadiarov, Narayan Pokhrel, Olga Poluyko, Morteza Roostaeinia, Junhui Shi, Ho Lun Tang, Karla Téllez Girón Flores, Arian Vezvaee, Shehla Yasmeen, and many others. Their company and moral support carried me through the graduate school, and all the shared meals, movie nights, board game sessions, and discussions I have had with them have become some of the most memorable experiences. In particular, I thank Tommy Lam for also being an accommodating and supportive roommate during the long days and nights that I spent working on this dissertation.

I will forever be grateful to my family and relatives: parents Alexey and Tatiana, brother Artem, sister-in-law Anna, nephews Alexey and Aleksandr, and uncles Aleksandr and Anton and their families. Their unconditional love, encouragement, belief in my abilities and tremendous support at every stage of my life and career have made possible all my academic achievements, including this dissertation.

Finally, I would like to mention my high school physics teachers, Andrey Kondratyev, Sergey Ryzhikov, Aleksandr Kubyshkin, and Vladimir Mayorov, as well as my undergraduate research advisor, Prof. Yuri Dahnovsky at the University of Wyoming. These people inspired me to study physics in the first place and provided invaluable guidance at the initial stages of my education. Without their early influence, this dissertation would not have been written.

Contents

List of Figures

List of Tables

Attributions

Chapter 2 was previously published. Reprinted from Anri Karanovich, Yoh Yamamoto, Koblar Alan Jackson, and Kyungwha Park, "Electronic structure of mononuclear Cu-based molecule from density-functional theory with self-interaction correction", J. Chem. Phys. 7 July 2021; 155 (1): 014106. https://doi.org/10.1063/5.0054439 [1], with the permission of AIP Publishing. Anri Karanovich (A.K.) performed all calculations and produced all the figures, and wrote the first draft of the methodology, results, and discussion sections of the paper. Dr. Kyungwha Park (K.P.) wrote the first draft of the introduction and conclusion sections, and K.P. and A.K. completed the final version of the paper. Dr. Koblar Alan Jackson substantially contributed to the research discussions, assisted us in learning how to use the FLOSIC code, and revised the final version of the paper. Dr. Yoh Yamamoto (University of Texas at El Paso) assisted us with learning how to use the FLOSIC code and helped us create the density-of-states plots presented in this paper.

Chapter 3 was previously published. Reprinted from Anri Karanovich, Koblar Alan Jackson, and Kyungwha Park, "Hyperfine interactions for small systems including transition-metal elements using self-interaction corrected density-functional theory", J. Chem. Phys.7 July 2024; **161** (1): 014102. https://doi.org/10.1063/5.0209226 [2], with the permission of AIP Publishing. A.K. implemented hyperfine parameter computation within the FLOSIC code, performed all calculations and produced all the figures, and wrote the first draft of the methodology, results, and discussion sections of the paper. K.P. wrote the first draft of the introduction and conclusion sections, and K.P. and A.K. completed the final version of the paper. Dr. Koblar Alan Jackson (Central Michigan University) substantially contributed to the research discussions, assisted us with using the FLOSIC code, and revised the final

version of the paper.

Chapter 4 is based on a manuscript in progress. Dr. Kamal Wagle (Los Alamos National Laboratory) performed preliminary CASSCF calculations on an original set of clusters, while A.K. performed the CASSCF and CASPT2 calculations on a different set of symmetric clusters, using K.W. results as a reference. Dr. Pratibha Dev (Howard University) provided us with the optimized geometry of the defect in a silicon carbide supercell [3]. A.K. created all the figures and wrote the current draft of the manuscript.

Chapter 1

Introduction

1.1 The Many-Body Electron Hamiltonian

The focus of this thesis is the application of the so-called first-principles (or *ab-initio*) methods to the calculations of physical and chemical properties of molecules and point defects. These methods attempt to derive these properties from the electronic structure obtained by directly solving the Schrödinger equation.

We consider an interacting system of electrons with spatial coordinates $\mathbf{r}_i$ and spin σ_i (which can take two values, "up" or "down"), and positive atomic nuclei with coordinates $\mathbf{R}_I$ and spin Σ_I. For each electron (nucleus), we can designate a variable $x_i = \{\mathbf{r}_i, \sigma_i\}$ ($X_I = \{\mathbf{R}_I, \Sigma_I\}$), which combines the three spatial coordinates and one spin index of the particle. Suppose that the "total" wavefunction $\Psi_T(\{\mathbf{X}_I\}, \{\mathbf{x}_i\})$ describes the lowest-energy (ground-state) configuration of this system. Then it must satisfy the time-independent version of the Schrödinger equation [4]:

$$\hat{H}_T \Psi_T = E_T \, \Psi_T \tag{1.1}$$

In the non-relativistic limit and in the absence of magnetic fields, the particles interact with each other only with Coulomb attraction or repulsion, the Hamiltonian becomes:

$$\hat{H}_T = \left[-\sum_i \frac{1}{2}\nabla_i^2 - \frac{1}{2M_I}\sum_I \nabla_I^2 \right] + \left[\sum_{i<j} \frac{1}{|\mathbf{r}_i - \mathbf{r_j}|} + \sum_{I<J} \frac{Z_I Z_J}{|\mathbf{R}_I - \mathbf{R_J}|} - \sum_{i,I} \frac{Z_I}{|\mathbf{r}_i - \mathbf{R}_I|} \right] \quad (1.2)$$

The first two terms in the Hamiltonian above describe the kinetic energies of electrons and nuclei, and the last three terms describe electron-electron, nucleus-nucleus, and electron-nucleus potential energies (note the conditions under the sums are introduced to avoid double-counting). Here and henceforth, we adopt the Hartree atomic units, in which $\hbar = m_e = e = 4\pi\epsilon_0 = 1$ (the reduced Planck's constant, the electron's mass and charge, and the Coulomb's constant are all equated to 1). For a nucleus with subscript I, Z_I is its relative charge, and M_I is the ratio of its mass to electron's mass.

A major simplification of the solution of Eq.1.1 with the Hamiltonian Eq.1.2 comes from the Born-Oppenheimer approximation [5]. Observing that the nuclear masses $M_I \gg 1$, the electrons can be viewed as moving within an almost stationary external potential created by much heavier and slower nuclei. Therefore, the total wavefunction (Ψ_T) can be represented as the product of nuclear (ψ_N) and electronic (Ψ_e) functions:

$$\Psi_T(\{\mathbf{R}_I\}, \{\mathbf{r}_i\}) = \psi_N(\{\mathbf{X}_I\})\ \Psi_e(\{\mathbf{x}_i\}; \{\mathbf{R}_I\}) \quad (1.3)$$

with electronic part satisfying the following equations (for the fixed nuclear positions $\mathbf{R}_I$):

$$\hat{H}_e \Psi_e\left(\{\mathbf{x}_i\}; \{\mathbf{R}_I\}\right) = E_e(\{\mathbf{R}_I\})\ \Psi_e(\{\mathbf{r}_i\}; \{\mathbf{R}_I\}) \quad (1.4)$$

$$\hat{H}_e = -\sum_i \frac{1}{2}\nabla_i^2 + \sum_{i<j} \frac{1}{|\mathbf{r}_i - \mathbf{r}_j|} - \sum_{i,I} \frac{Z_I}{|\mathbf{r}_i - \mathbf{R}_I|} \quad (1.5)$$

The solution to Eq. 1.4 can be used then to determine the nuclear wavefunction:

$$\hat{H}_N \psi_N \left(\{\mathbf{X_I}\}\right) = E_T \ \psi_N \left(\{\mathbf{R}_I\}\right) \tag{1.6}$$

$$\hat{H}_N = -\sum_i \frac{1}{2M_I} \nabla_I^2 + \sum_{I<J} \frac{Z_I Z_J}{|\mathbf{R}_I - \mathbf{R_J}|} + E_e(\{\mathbf{R}_I\}) \tag{1.7}$$

In our work, we focus on solving Eq. 1.4 for the electron part of the wavefunction.

1.2 Wavefunction-Based Methods

1.2.1 Hartree-Fock Approximation

Equation 1.4 determines the total many-body electron wavefunction $\Psi_e(\mathbf{x}_i)$ (further denoted simply as $\Psi(\mathbf{x}_i)$). The number of coordinates on which Ψ depends is proportional to the total number of electrons in the system. For molecules, this number can range in hundreds or thousands. It is therefore evident that solving directly for the total wavefunction Ψ can be computationally challenging. The problem can be simplified if Eq. 1.4 can be transformed into equations for single-electron functions $\phi(\mathbf{x}_i)$, from which the total function can be reconstructed.

A simple ansatz (first proposed by Hartree [6, 7]) would be to have $\Psi(\{\mathbf{x}_i\})$ to be a product of single-electron functions $\phi_i(\mathbf{x}_i)$:

$$\Psi\left(\mathbf{x}_1, \mathbf{x}_2 \ldots \mathbf{x}_N\right) = \phi_1(\mathbf{x}_1)\, \phi_2(\mathbf{x}_2) \ldots \phi_N(\mathbf{x}_N) \tag{1.8}$$

where N is the total number of electrons. However, this approximation does not account for the anti-symmetry property of the total electron wavefunction: exchanging the coordinates

of any two separate electrons must change the sign of Ψ:

$$\Psi\left(\dots \mathbf{x}_i \dots \mathbf{x}_j \dots\right) = -\Psi\left(\dots \mathbf{x}_j \dots \mathbf{x}_i \dots\right) \tag{1.9}$$

This property follows from the spin-statistic theorem [8] for fermions, and facilitates Pauli exclusion principle (no two electrons can occupy the same state/have the same coordinates). However, the ansatz of Eq.1.8 is *not* explicitly antisymmetric: $\phi_i(\mathbf{x}_j)\phi_j(\mathbf{x}_i) \neq -\phi_i(\mathbf{x}_i)\phi_j(\mathbf{x}_j)$ in general.

This can be fixed by considering instead a fully antisymmetric linear combination of the single-electron functions' products, which is represented with a Slater determinant [9]:

$$\Psi_{SD}\left(\mathbf{x}_1, \mathbf{x}_2 \dots \mathbf{x}_N\right) = \frac{1}{\sqrt{N!}} \begin{vmatrix} \phi_1(\mathbf{x}_1) & \phi_1(\mathbf{x}_2) & \dots & \phi_1(\mathbf{x}_N) \\ \phi_2(\mathbf{x}_1) & \phi_2(\mathbf{x}_2) & \dots & \phi_2(\mathbf{x}_N) \\ \dots & \dots & \ddots & \vdots \\ \phi_N(\mathbf{x}_1) & \phi_N(\mathbf{x}_2) & \dots & \phi_N(\mathbf{x}_N) \end{vmatrix} \tag{1.10}$$

The wavefunction given by Eq.1.10 is now explicitly antisymmetric: changing the coordinates of any two electrons ($\mathbf{x}_i$, $\mathbf{x}_j$) is equivalent to switching the columns of the matrix, which changes the sign of the determinant. If any two electrons were in the same state ($\phi_i = \phi_j$), then the matrix would have two identical rows, which would make the determinant and the whole wavefunction equal to 0. This supports the Pauli exclusion principle.

One could use the Slater determinant for some initial guess of the total electron wavefunction Ψ in Eq.1.4. Then, by using the variational principle to find the minimum of the electron energy in Eq.1.4, while keeping the single-electron functions orthonormalized with the La-

grange multipliers ε_i, a set of single-electron Hartree-Fock equations [10, 11] is produced:

$$\hat{F}\phi_i(\mathbf{x}_i) = \varepsilon_i\phi_i(\mathbf{x}_i) \tag{1.11}$$

$$\hat{F} = -\frac{1}{2}\nabla^2 + V_{ext} + V_H + V_x^{i,\sigma} \tag{1.12}$$

$$V_H = \sum_j \int d\mathbf{x}' \frac{\phi_j^*(\mathbf{x}')\phi_j(\mathbf{x}')}{|\mathbf{r}' - \mathbf{r}|} \tag{1.13}$$

$$V_x^{i,\sigma}\ \phi_i(\mathbf{r},\sigma) = -\sum_j \int d\mathbf{r}' \frac{\phi_j^*(\mathbf{r}',\sigma)\phi_i(\mathbf{r}',\sigma)}{|\mathbf{r}' - \mathbf{r}|}\phi_j(\mathbf{r},\sigma) \tag{1.14}$$

$$\tag{1.15}$$

Note that the $V_x^{i,\sigma}$ term depends itself on the ϕ_i, and is known as the exchange term, while V_H, the Hartree term, describes Coulomb interaction of the particle with other particles. Since $V_x^{i,\sigma}$ depends on the orbital, these equations should be solved self-consistently: the previous guess for the orbitals produces the new estimate for the exchange potentials, which in turn produces a new set of orbitals. The process, known as a self-consistent field (SCF) calculation, can be performed until the total energy converges within a pre-set threshold.

1.2.2 Multiconfigurational Methods

The Hartree-Fock approximation can be a good starting point for the electronic structure calculations, since it represents the simplest antisymmetric wavefunction form. However, the electronic wavefunctions in many systems cannot be approximated well with only one Slater determinant. The difference between the properties of the exact solution to Eq. 1.4 and the Hartree-Fock approximation is referred to as the effect of *electronic correlation*.

In general, however, the exact electron wavefunction Ψ can be represented as a linear com-

bination (finite or infinite) of Slater determinants:

$$|\Psi\rangle = \sum_n C_n |\Phi_n\rangle \tag{1.16}$$

where Φ_n are various N-electron Slater determinants, and C_n are expansion coefficients.

For instance, if one has a *complete* basis set of single-electron wavefunctions $\varphi_j(r, \sigma)$, and Φ_n are all possible N-particle Slater determinants from them, then the space spanned by these Φ_n should contain any N-electron antisymmetric wavefunction Ψ.

With a finite basis set, one could still construct all possible N-electron determinants and approximate the total wavefunction as the linear combination of them according to Eq.1.16. This wavefunction form can be used to variationally minimize the Hamiltonian expectation value with respect to C_i, to obtain the ground-state energy and wavefunction. This is, in a nutshell, the full configuration interaction (full CI) method [12]. In practice, it can only be done for small systems, since with the increasing number of electrons, including all possible determinants becomes computationally unfeasible very quickly.

Complete Active Space Self-Consistent Field

In many cases, strongly correlated systems occur when there are several energy eigenstates with very close energies (or degenerate) to the ground state of the system. This is the case in molecules with resonant structures (such as O_3), systems with transition-metal elements (due to the near-degeneracy of configurations with different $3d$ orbital occupations), in processes with chemical bond breaking, etc. In this case, a good description of the system can be achieved by including only a few Slater determinants which describe these near-degenerate configurations.

In these cases, a much more practical approach than the full CI method is the complete active space self-consistent field (CASSCF) method [13, 14, 15, 16]. Unlike the full CI method, it limits the size of the linear combination in Eq.1.16 by only including the Slater determinants that are generated by varying the occupations of a subset of electron orbitals, known as the *active space*, while all other electron orbitals have fixed occupations. Due to this limitation, the resulting wavefunction in Eq.1.16 will depend not only on the expansion coefficients C_n, but also on the selected set of electron orbitals $\varphi_j(r, \sigma)$. Both the coefficients and the orbitals can be varied to minimize the energy.

The resultant procedure for CASSCF is the following:

1. Start with a set of (typically) spin-restricted orbitals (i.e. the spatial part of them is maintained the same for both spin states)

2. Designate three groups of these orbitals: *inactive*, *active*, and *virtual*. All virtual orbitals are empty, all inactive orbitals are doubly-occupied, and active orbitals can have varying occupations (see Fig.1.1). Let the total number of active orbitals be p and total number of electrons in them q

3. Construct all possible Slater determinants with different occupations of p active orbitals by q electrons (with a pre-determined total spin S)

4. Use a linear combination of these Slater determinants as an ansatz for the total wavefunction; minimize the energy by varying both the orbitals $\varphi_j(r, \sigma)$ *and* the expansion coefficients C_n

If the set of active orbitals (i.e., the active space, or AS) included all available electron orbitals, the CASSCF method would reproduce the full CI approach. In general, choosing a larger active space can improve the accuracy of the CASSCF prediction, but will also

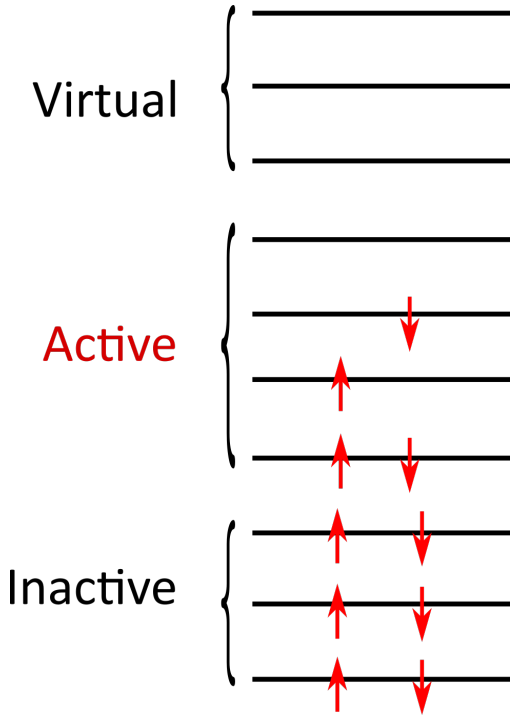

Figure 1.1: Schematic representation of the three sets of orbitals in the CASSCF method. Virtual and inactive have fixed occupations, while active orbitals can have varying occupations

increase the computational cost. Furthermore, the active space must be carefully selected to ensure good performance of the CASSCF calculation. In general, one wants to include the orbitals that can be important for the processes and properties of the system that one wants to compute. For example, systems undergoing bond breaking or formation would require the bonding and antibonding orbitals to be included in AS, while transition-metal systems would need the $3d$ orbitals to be included, etc. In general, however, construction of a good active space is not a trivial task, as it depends on the specific system and properties one wants to study, and typically requires good chemical intuition and/or several trial calculations [13].

1.3 Density Functional Theory

1.3.1 Hohenberg-Kohn Theorems

In 1964, Hohenberg and Kohn [17] formulated the following two theorems connecting the ground-state electron density $n_0(\mathbf{r})$ with other physical observables:

1. **The external potential $V_{ext}(\mathbf{r})$, acting on a system of electrons, is uniquely determined (up to an additive constant) by the ground-state electron density $n_0(\mathbf{r})$;**

2. **There exists a universal functional of electron density $n(\mathbf{r})$, $F_{HK}(n)$, such that the energy functional defined as:**

$$E_{HK}^{V}(n) = F_{HK}(n) + \int d\mathbf{r} V_{ext}(\mathbf{r}) n(\mathbf{r}) \tag{1.17}$$

is minimized at the exact ground-state electron density $n_0(\mathbf{r})$, and has the minimal value of the ground-state energy.

For systems with a non-degenerate ground state, the first theorem can be easily proven by contradiction. The proof utilizes the variational principle, which states that the non-degenerate ground-state wavefunction Ψ_0 minimizes the expectation value of its Hamiltonian, $\langle\Psi_0| H |\Psi_0\rangle$. Therefore, for any different wavefunction $\Psi \neq \Psi_0$, the following inequality holds: $\Psi \neq \Psi_0$, $\langle\Psi| H |\Psi\rangle > \langle\Psi_0| H |\Psi_0\rangle$.

Consider two external potentials that differ more than by a constant, $V_{ext}^{(1)} \neq V_{ext}^{(2)}$. These produce different Hamiltonians $H^{(1)}$ and $H^{(2)}$, resulting in two different ground-state wave-

functions $\Psi^{(1)}$ and $\Psi^{(2)}$. Suppose they produce the same ground state density $n_0(\mathbf{r})$. Then:

$$\begin{aligned} E^{(1)} &= \langle \Psi^{(1)} | \, H^{(1)} \, | \Psi^{(1)} \rangle < \langle \Psi^{(2)} | \, H^{(1)} \, | \Psi^{(2)} \rangle \, ; \\ E^{(1)} &< \langle \Psi^{(2)} | \, H^{(2)} \, | \Psi^{(2)} \rangle + \langle \Psi^{(2)} | \, H^{(1)} - H^{(2)} \, | \Psi^{(2)} \rangle \, ; \\ E^{(1)} &< E^{(2)} + \int d\mathbf{r} \left[V_{ext}^{(1)} - V_{ext}^{(2)} \right] (\mathbf{r}) n_0(\mathbf{r}) \end{aligned} \tag{1.18}$$

However, by performing equivalent steps, a similar inequality can be obtained for $E^{(2)}$ instead of $E^{(1)}$:

$$E^{(2)} < E^{(1)} + \int d\mathbf{r} \left[V_{ext}^{(2)} - V_{ext}^{(1)} \right] (\mathbf{r}) n_0(\mathbf{r}) \tag{1.19}$$

After adding the two inequalities together,

$$E^{(2)} + E^{(1)} < E^{(2)} + E^{(1)} \tag{1.20}$$

which leads to a contradiction. The validity of this theorem has also been established for systems with degenerate ground states [18].

As a corollary to this theorem, since the external potential is sufficient to determine the many-body electron Hamiltonian H_e, it follows that *all properties* of the system are, in theory, uniquely determined by (and are functionals of) $n_0(\mathbf{r})$.

In particular, the ground-state density n_0, through the external potential $V_{ext}(n_0)$, also uniquely fixes the ground-state wavefunction $\Psi(n_0)$, which in turn defines the total electron kinetic energy: $T(n_0) = \langle \Psi(n_0) | -\frac{1}{2} \sum_i \nabla_i^2 \quad | \Psi(n_0) \rangle$; and the Coulomb interaction energy between the electrons $U(n_0) = \langle \Psi(n_0) | \sum_{i,j} \frac{1}{|r_i - r_j|} \; | \Psi(n_0) \rangle$.

Assuming that for a given density n there exists an external potential $V_{ext}(n)$ that produces

it (i.e. n is *V-representable*), the universal functional mentioned in the second theorem is then defined as

$$F_{HK}(n) = T(n) + V_{ee}(n) \tag{1.21}$$

and is equal to the sum of kinetic and interaction energies of electrons in a system with $V_{ext}(n)$. The total electron energy $E^V_{HK}(n)$ in that system is then given by Eq.1.17. Suppose now that a different V-representable n' is produced by V'_{ext}, which in turn produces the wavefunction $\Psi(n')$. Then, if we keep the second term in $E^V_{HK}(n)$ the same (i.e. defined from V_{ext} rather than V'_{ext}), we obtain from the variational principle:

$$E^V_{HK}(n') = \langle \Psi(n') | \, H \, | \Psi(n') \rangle > \langle \Psi(n) | \, H^V_{HK} \, | \Psi(n) \rangle = E^V_{HK}(n) \tag{1.22}$$

(In this form, the theorem assumes that there exists an external potential V_{ext} that has n as the ground-state density, in other words, n is *V-representable*. However, the theorem has been generalized to weaker assumptions [18])

The significance of this theorem is that $F_{HK}(n)$ does not depend on the external density (hence is a universal functional), and if we knew its general form, then we could construct $E^V_{HK}(n)$ from Eq.1.17 and minimize it to find the exact $n_0(\mathbf{r})$, from which all other properties of the system can be determined according to theorem 1. In practice, however, while the Hohenberg-Kohn theorems demonstrate the existence of density functionals for all physical properties, the exact form of these functionals is unknown. In particular, $T(n)$ is not trivial to derive without knowing the explicit wavefunction $\Psi(n)$.

1.3.2 Kohn-Sham equations

Another major development in DFT was introduced by Kohn and Sham in 1965 [19], who proposed a practical method of finding the ground-state electron density.

Instead of working with the original system of interacting electrons with ground-state density $n_0(\mathbf{r})$, the method suggests instead to consider a system of auxiliary non-interacting particles, moving in some effective and local external potential $V_{eff}(\mathbf{r})$, which has the same ground-state density $n_0(\mathbf{r})$ as the original electron system. Since the universal functional $F_{HK}(n)$ and the energy $E^V_{HK}(n)$ depend only on the density, it may be simpler to find the ground-state density for non-interacting particles instead, assuming that an appropriate $V^\sigma_{eff}(\mathbf{r})$ is provided.

The lack of interactions means that the Schrödinger equation can be written separately for each auxiliary single-particle state with spin σ:

$$\hat{H}_{KS}\ \phi_i(\mathbf{r},\sigma) = \left[-\frac{1}{2}\nabla^2 + V^\sigma_{eff}(\mathbf{r})\right]\phi_i(\mathbf{r},\sigma) = \varepsilon^\sigma_i \phi_i(\mathbf{r},\sigma) \tag{1.23}$$

where we assume the effective potential can be different for different spin channels. For the ground state, $N^\uparrow$ ($N^\downarrow$) lowest-energy $\varepsilon^\uparrow_i$ ($\varepsilon^\downarrow_i$) energy eigenstates are populated, and the total wavefunction is represented with a Slater determinant of the occupied $\phi_i(\mathbf{r},\sigma)$ levels. The total density is then given by:

$$n(\mathbf{r}) = \sum_{\sigma\in\{\uparrow,\downarrow\}}\sum_{i}^{N_\sigma} |\phi_i(\mathbf{r},\sigma)|^2 = \sum_{i}^{N_\uparrow} |\phi_i(\mathbf{r},\uparrow)|^2 + \sum_{i}^{N_\downarrow} |\phi_i(\mathbf{r},\downarrow)|^2 = n_\uparrow(\mathbf{r}) + n_\downarrow(\mathbf{r}) \tag{1.24}$$

The energy functional then should be

$$E^V_{HK}(n) = F_{HK}(n) + \int d\mathbf{r} V_{ext}(\mathbf{r}) n(\mathbf{r}) \tag{1.25}$$

$$= T_s(n) + \int d\mathbf{r} \left[V_{ext}(\mathbf{r}) + V_{eff}(\mathbf{r})\right] n(\mathbf{r}) = T_s(n) + E_{ext}(n) + E_H(n) + E_{XC}(n)$$

$$= T(n) + E_{ext}(n) + E_{ee}(n) \tag{1.26}$$

where $T_s(n) = -\frac{1}{2}\sum_\sigma \sum_i \langle \phi_i(\mathbf{r},\sigma)| \nabla^2 |\phi_i(\mathbf{r},\sigma)\rangle$ is the kinetic energy of *auxiliary particles* $E_{ext} = \int d\mathbf{r} V_{ext}(\mathbf{r}) n(\mathbf{r})$ is the energy due to the external potential, and the energy due to the effective potential is divided in two terms: the Hartree energy $E_H(n) = \frac{1}{2}\int\int d\mathbf{r} d\mathbf{r}' \frac{n(\mathbf{r})n(\mathbf{r}')}{|\mathbf{r}-\mathbf{r}'|}$, similar to one in the Hartree-Fock calculations, and so-called *exchange-correlation energy* E_{XC}. On the other hand, E^V_{HK} also describes the total energy in the real electron system, due to the matching ground-state densities; T(n) is the kinetic energy of real electrons, and E_{ee} is their interaction energy. For the auxiliary system, only E_{XC} has to be approximated.

According to the second Hohenberg-Kohn theorem, the correct ground-state density $n_0(\mathbf{r})$ must minimize the $E^V_{HK}(n)$ functional. In turn, the density depends on the auxiliary orbitals via Eq.1.24. By minimizing the energy with respect to the orbitals $\phi_(\mathbf{r},\sigma)$, while keeping the orbitals orthonormal, we obtain an equation similar to 1.23, but with the following effective potential

$$V_{eff}(\mathbf{r}) = V_{ext}(\mathbf{r}) + V_H(\mathbf{r}) + V^\sigma_{XC}(\mathbf{r}) \tag{1.27}$$

where each potential term is defined as a functional derivative of the corresponding energy term with respect to density, for example $V_H(\mathbf{r}) = \frac{\delta E_H[n(\mathbf{r})]}{\delta n(\mathbf{r})}$.

Finally, a density optimization scheme is obtained. First, for some initial guess of the auxiliary orbitals $\phi_i(\mathbf{r},\sigma)$, the density $n(\mathbf{r})$ (or $n_\sigma(\mathbf{r})$) is obtained. The energy terms in eq. 1.25, as well as potentials, are then recalculated based on the new density. Equations 1.23

are solved, based on the new potentials, and the updated solutions for $\phi_i(\mathbf{r}, \sigma)$ are used again to recompute the electron density and repeat the process. The self-consistent field procedure here runs until some convergence criteria are met, for example until the consecutive energies do not differ more than some threshold.

As mentioned above, the only term that needs to be approximated here is the exchange-correlation energy E_{XC} and potential V_{XC}. One of the biggest challenges in the development of DFT methods has been constructing good approximations for these terms. Some of the most common approaches to evaluate the E_{XC} terms are as follows:

- Local (spin) density approximation (LSDA), where the electron density is assumed to vary sufficiently slowly so that the total E_{XC} energy can be approximated as

$$E_{XC}^{LSDA}(n_\uparrow, n_\downarrow) = \int d\mathbf{r} n(\mathbf{r}) \varepsilon_{XC} \left[n_\uparrow(\mathbf{r}), n_\downarrow(\mathbf{r}) \right] \tag{1.28}$$

  where the exchange-correlation energy density is assumed to only depend on the local values of the electron spin-up and spin-down densities. Usually the form of ε_{XC} here is derived from the homogeneous electron gas model. Widely-used examples of approximations of this kind are the Perdew-Wang (PW92) [20] and Vosko, Wilk and Nusair (VWN) [21] functionals.

- Generalized gradient approximation (GGA) where the XC energy density can also depend on the gradient of the electron density in both spin channels:

$$E_{XC}^{GGA}(n_\uparrow, n_\downarrow) = \int d\mathbf{r} n(\mathbf{r}) \varepsilon_{XC} \left[n_\uparrow(\mathbf{r}), \nabla n_\uparrow(\mathbf{r}), n_\downarrow(\mathbf{r}), \nabla n_\downarrow(\mathbf{r}) \right] \tag{1.29}$$

  Widely-used examples of the exchange-correlation functionals of these types are Perdew-Wang (PW91) [20, 22] and Perdew-Burke-Ernzerhof (PBE) [23] functionals.

1.3.3 Self-interaction Errors

The Kohn-Sham approach to DFT has been demonstrated to be very successful in many areas, which has earned Walter Kohn a Nobel prize in chemistry in 1998 (shared with John Pople). However, there are some situations where Kohn-Sham DFT does not predict the electronic properties correctly. These include the underestimation of band gaps in semiconductors and solids [24, 25], underestimated energy reaction barriers [26], overestimated exchange coupling constants [27], and many other effects.

Such discrepancies have been associated with the presence of the so-called self-interaction error (SIE) in DFT. This is related to the fact that the electron-electron interaction term in Eq.1.27, $V_H(n(\mathbf{r})) + V_{XC}^{\sigma}(n(\mathbf{r}))$, does not in general distinguish the contributions to the electron density of the given orbital ϕ_i from the contributions of other orbitals. As a result, a Kohn-Sham state ϕ_i may experience a nonphysical interaction with itself.

In particular, let us consider a system consisting of only one (spin-up) electron, with orbital $\psi_{i,\alpha}(\mathbf{r})$, which produces the density $n_{i,\alpha}(\mathbf{r})$. The corresponding single-particle Kohn-Sham energy would be

$$E_{KS}(n_{i,\alpha}) = T_s(n_{i,\alpha}) + E_{ext}(n_{i,\alpha}) + E_H(n_{i,\alpha}) + E_{XC}^{\sigma}(n_{i,\alpha}, 0) \tag{1.30}$$

where E_{XC}^{σ} is considered to be a functional of $n_{\uparrow}$ and $n_{\downarrow}$. The sum of the third and fourth terms on the right-hand side of Eq.1.30 should be equal to zero, since the single particle should not experience a Coulomb repulsion from itself. In Hartree-Fock theory, the self-Hartree term cancels out by the self-exchange term. However, in Kohn-Sham FT, their sum is not zero because the E_{XC} term is approximated.

This discrepancy is known as the SIE. Since he electron essentially feels repulsion from itself,

the predicted orbitals and densities are delocalized by SIE.

Perdew-Zunger Self-Interaction Correction

One of the most well-known schemes to counteract the self-interaction error was proposed by Perdew and Zunger in 1981 [28]. Their proposal was to subtract all the self-interaction energies for a given set of orbitals $\{\psi_{i,\sigma}(\mathbf{r})\}$ from the total energy functional:

$$E_{PZ-SIC}(n, \{\psi_{i,\sigma}\}) = E_{KS}(n) - \sum_{\sigma}^{} \sum_{i}^{N_\sigma} [E_H(n_{i,\sigma}) + E_{XC}(n_{i,\sigma}, 0)] \tag{1.31}$$

Note that this corrected expression for energy would be exact for one-electron systems, and the magnitude of the correction in general would be zero for the exact (non-approximate) E_{XC} functional. Also note that the correction term depends explicitly on the choice of the orbital set, $\{\psi_{i,\sigma}(\mathbf{r})\}$. This makes the total Perdew-Zunger self-interaction correction PZ-SIC energy expression in depend not only on the density, but also on the choice of orbitals representing that density as well. For example, a unitary transformation within the space of occupied orbitals does not change the electron density, but it may increase or decrease the value of E_{PZ-SIC}. Another issue with the energy definition in Eq.1.31 is that if delocalized orbitals are used for the correction, the energy is not size-extensive [28]. For instance, the correction would vanish for solids if the Kohn-Sham orbitals are used, and it would be a maximum for localized orbitals.

Considering the discussion above, one can obtain the proper ground-state energy for Eq.1.31 by minimizing the energy functional with respect to both the electron density and the parameters of a unitary transformation between the occupied electron orbitals. It has been shown[24, 29, 30] that such variational minimum is achieved if the orbitals also satisfy a set

of localization equations:

$$\langle \phi_{i,\sigma} | \, V_{i,\sigma}^{SIC}(\mathbf{r}) - V_{j,\sigma}^{SIC}(\mathbf{r}) \, | \phi_{j,\sigma} \rangle = 0 \tag{1.32}$$

$$V_{i,\sigma}^{SIC}(\mathbf{r}) = \frac{\delta E_H[n_{i,\sigma}(\mathbf{r})] + E_{XC}[n_{i,\sigma}(\mathbf{r}), 0]}{\delta n_{i,\sigma}(\mathbf{r})} \tag{1.33}$$

in addition to N Kohn-Sham-like equations. Hence, to solve for the PZ-SIC functional for N electrons, about N^2 equations must be satisfied, which makes this method computationally expensive.

Fermi–Löwdin Orbital Self-Interaction Correction

In 2014, Pederson, Ruzsinszky and Perdew [31] proposed to compute the correction term in the PZ-SIC energy, defined by Eq. 1.31, by using Fermi-Löwdin orbitals. First, a set of Fermi orbitals is defined as

$$F_{i\sigma}(\boldsymbol{r}) = \frac{\sum_\alpha \psi_{\alpha\sigma}(\boldsymbol{a}_{i\sigma})\psi_{\alpha\sigma}(\boldsymbol{r})}{\sqrt{\sum_\alpha |\psi_{\alpha\sigma}(\boldsymbol{a}_{i\sigma})|^2}}, \tag{1.34}$$

where $\psi_{\alpha\sigma}$ are some initial set of orbitals (e.g. Kohn-Sham orbitals, or any other type), and $a_{i,\sigma}$ are spatial positions known as the *Fermi orbital descriptors* (FODs). Orbitals defined by equation 1.34 can be shown to be invariant under unitary transformations within the occupied orbital space, and they are defined only by the corresponding FOD and the electron density. Furthermore, Fermi orbitals are localized and normalized. However, they are not orthogonal yet.

The Fermi orbitals are then orthogonalized using the Löwdin [32] orthogonalization scheme, to produce Fermi-Löwdin orbitals (FLOs) $\phi_{i,\sigma}^{FLO}$, whose densities $n_{i,\sigma}^{FLO}$ are then plugged in

the PZ-SIC energy functional:

$$E_{FLOSIC}(n, \{a_{i,\sigma}\}) = E_{KS}(n) - \sum_{\sigma} \sum_{i}^{N_\sigma} \left[E_H(n_{i,\sigma}^{FLO}) + E_{XC}(n_{i,\sigma}^{FLO}, 0) \right] \tag{1.35}$$

Note that the FLOSIC energy for a given set of FODs is defined in terms of FLOs and is therefore invariant under the unitary transformations with respect to the original starting set of occupied orbitals $\psi_{\alpha\sigma}$. Since FLOs are localized, the size-extensivity problem also goes away.

The FLOSIC energy must be optimized both with respect to both the density n and the set of FODs. For the latter, some initial guess FODs are produced, which are then optimized during energy minimization procedures, by using the analytic FOD forces [33]. The optimized FOD positions have been shown to follow the bonding patterns in molecules and electron-shell filling patterns in single atoms or for core orbitals [34]. For example, a Ne atom's optimal FODs would consist of a pair of spin-up and spin-down FODs at the atomic position, corresponding to the filled $1s^2$-shell, and four spin-up and four spin-down FODs around the atomic center in tetrahedral configurations, corresponding to $2s^2 2p^6$ shell. The FOD optimization procedure is described in more detail in Chapters 2 and 3 of this thesis.

Chapter 2

Electronic Structure of Mononuclear Cu-based Molecule from FLOSIC-DFT

This chapter was previously published. Reprinted from Anri Karanovich, Yoh Yamamoto, Koblar Alan Jackson, and Kyungwha Park, "Electronic structure of mononuclear Cu-based molecule from density-functional theory with self-interaction correction", J. Chem. Phys. 7 July 2021; 155 (1): 014106. https://doi.org/10.1063/5.0054439 [1] *, with the permission of AIP Publishing.*

In this chapter, we investigate the electronic structure of a planar mononuclear Cu-based molecule $[Cu(C_6H_4S_2)_2]^z$ in two oxidation states (z=−2, −1) using density-functional theory (DFT) with the Fermi-Löwdin orbital (FLO) self-interaction correction (SIC). The dianionic Cu-based molecule was proposed to be a promising qubit candidate. Self-interaction error within approximate DFT functionals renders severe delocalization of electron and spin densities arising from 3d orbitals. The FLO-SIC method relies on optimization of Fermi-Löwdin orbital descriptors (FODs) with which localized occupied orbitals are constructed to create the SIC potentials. Starting with many initial sets of FODs, we employ a frozen-density loop algorithm within the FLO-SIC method to study the Cu-based molecule. We find that the electronic structure of the molecule remains unchanged despite somewhat different final

FOD configurations. In the dianionic state (spin $S = 1/2$), FLO-SIC spin density originates from the Cu d and S p orbitals with an approximate ratio of 2:1, in quantitative agreement with multireference calculations, while in the case of SIC-free DFT, the orbital ratio is reversed. Overall, FLO-SIC lowers the energies of the occupied orbitals and in particular the $3d$ orbitals unhybridized with the ligands significantly, which substantially increases the energy gap between the highest occupied molecular orbital (HOMO) and the lowest unoccupied molecular orbital (LUMO) compared to SIC-free DFT results. The FLO-SIC HOMO-LUMO gap of the dianionic state is larger than that of the monoionic state, which is consistent with experiment. Our results suggest a positive outlook of the FLO-SIC method in the description of magnetic exchange coupling within $3d$-element based systems.

2.1 Introduction

Systems including $3d$ transition-metal elements are difficult to study using density-functional theory (DFT) due to strong electron correlation involving the localized d orbitals. The approximate nature of the exchange-correlation functional within the DFT formalism limits an accurate description of multiconfigurational/multireference features of strongly correlated systems. In addition, such nature allows significant Coulomb interactions of electrons with themselves, referred to as self-interaction error (SIE) [28], which results in an underestimate of the band gap or gap between the highest occupied molecular orbital (HOMO) and the lowest unoccupied molecular orbital (LUMO) as well as an overestimate of exchange interaction between $3d$ transition-metal centers, to name a few. An introduction of on-site Coulomb repulsion U within the DFT formalism [35, 36] aligns with an effort to compensate for SIE. Although standard multireference quantum chemistry methods can describe mononuclear transition-metal-based molecules, they are not practical for multinuclear magnetic molecules

due to extremely high computational cost.

As an alternative, one can consider an application of DFT with self-interaction correction (SIC) to $3d$ transition-metal systems. Perdew and Zunger (PZ) proposed a systematic method to impose the SIC to any spin-density-functional approximation [28]. This PZ-SIC formalism was successfully applied within the local spin density approximation (LSDA) to atoms and molecules [28, 29] and solids [24]. However, the PZ-SIC method adds a set of N^2 conditions that need to be satisfied to reach a minimum energy and the SIC energy is not necessarily size-consistent, where N is the total number of electrons. Recently, a new practical SIC scheme adapted from the PZ-SIC formalism has been proposed using localized Fermi-Löwdin orbitals (FLO) [31, 37]. In this scheme referred to as FLO-SIC, $3N$ conditions have to be satisfied and the SIC energy is size-consistent. The FLO-SIC method was applied to various non-magnetic molecules [38, 39, 40, 41, 42, 43, 44], giving rise to improvement of ionization energies of organic molecules [39] and vertical detachment energies of water clusters [40]. However, applications of the FLO-SIC method to $3d$ transition-metal systems have been limited [41, 43, 45]. Small mononuclear $3d$ transition-metal-based molecules would be ideal to gauge an applicability of the FLO-SIC method, the results of which provide insight into employment of the FLO-SIC method to multinuclear $3d$ transition-metal systems.

Recently, a crystal of small Cu-based magnetic molecules, $[Cu(C_6H_4S_2)_2]^{-2}$ (or $[Cu(II)(bdt^{2-})_2]^{-2}$), has been shown to have long spin-lattice and spin-spin relaxation times at room temperature attributed to small spin-orbit coupling, to the well-separated ground doublet, and to strong metal-ligand covalency [46], which renders the molecule a promising candidate for quantum information science applications. The electronic structure of the dianionic Cu-based molecule was investigated using electron paramagnetic resonance (EPR) experiments [46, 47], and it was also calculated using multireference quantum chemistry methods [46], time-dependent DFT (TDDFT) [47], and DFT with a hybrid functional [47]. Interestingly, Ref. [47] sug-

gested that two competing electronic structures (where the spin density is mostly carried by either the Cu or the S ligands) coexist in the dianionic Cu-based molecule, although such a scenario was not reported in the multireference study [46]. On the other hand, the monoanionic Cu-based molecule, $[Cu(C_6H_4S_2)_2]^{1-}$, was observed to be non-magnetic with its UV-visible absorption peak at somewhat lower energy than the dianionic molecule [47]. Derivatives of the monoanionic Cu-based molecule were also synthesized and their properties including optical absorption spectra were characterized [48, 49]. The electronic structures of the monoanionic molecule and one of the derivatives, $[Cu(III)(C_{14}H_{20}S_2)_2]^{1-}$, were calculated using DFT with a hybrid functional [47, 48].

In this work, we systematically investigate the electronic structure of the dianionic and monoanionic mononuclear Cu-based molecules, $[Cu(C_6H_4S_2)_2]^z$ ($z = -2, -1$), using the FLO-SIC method. Starting with many Fermi-Löwdin orbital descriptor (FOD) configurations for a given molecular structure and charge state, we optimize them in order to obtain the optimal FLO-SIC energy for each FLO configuration. For comparison, we also do SIC-free (standard) DFT and self-interaction free wave function calculations at the unrestricted Hartree-Fock (UHF) and multiconfigurational levels. Since the FLO-SIC potential lowers energies of the occupied Cu d orbitals much more than the occupied ligand orbitals, the FLO-SIC HOMO energy is greatly shifted downward which results in a large HOMO-LUMO gap. In addition, characteristics of the FLO-SIC HOMO significantly differ from those of the standard DFT and multiconfigurational/multireference calculations. The FLO-SIC spin density for the dianonic case quantitatively agrees well with the multiconfigurational/multireference result and it is consistent with EPR experimental data [47]. The FLO-SIC HOMO-LUMO gap of the monoanionic molecule is significantly smaller than that of the dianionic molecule, which may be in line with the experimental UV-optical absorption spectra.

In Sec. 2.2 we present the geometries of the dianionic and monoanionic Cu-based molecules

that we use. In Sec. 2.3 we discuss our systematic applications of the FLO-SIC method to the molecules using a frozen-density loop algorithm, molecular symmetries and previous FLO-SIC results from atoms [34]. Then we show the FLO-SIC charge and spin density of states as well as the HOMO and LUMO characteristics for the two charge states compared to our UHF, standard (SIC-free) DFT, and multiconfigurational calculations as well as other groups' studies [46, 47, 48] in Secs. 2.4 and 2.5. In Sec. 2.6 we make conclusions and provide outlook.

2.2 Geometries of Cu-based molecules

Figure 2.1 shows the molecular geometry of $[Cu(C_6H_4S_2)_2]^{2-}$ (referred to as **Q-2**) derived from the experimental data [47]. The molecule has almost planar structure in the xy plane with inversion symmetry up to precision of $\sim 10^{-4}$Å. There is an approximate D_{2h} symmetry. The Cu-S bond lengths are 2.294 and 2.265 Å, and the S-Cu-S angles are 89.6 and 90.4°. A nominal ionic picture dictates that the Cu^{2+} ion ($3d^9$) carries the spin $S = 1/2$, while the four S atoms, each of which has an oxidation state of -1, do not carry spin. However, the experimental data [46, 47] strongly suggests covalent bonding between the Cu and the S atoms. In our study, we use the experimental geometry of **Q-2** [47] with C-H bond lengths modified to be a standard value of 1.09 Å, without further geometry relaxation. The coordinates of the molecular geometry are listed in Table 2.6 in the Appendix 2.8.1.

The experimental geometry of the monoanionic molecule, $[Cu(C_6H_4S_2)_2]^{1-}$ (referred to as **Q-1**), is not available. Therefore, we separately optimize the molecular geometry of **Q-1** for the triplet ($S = 1$) and singlet state ($S = 0$) without symmetry constraints until the root mean square of the force is less than 1 mHa/a_B (where a_B is Bohr radius) within the Perdew-Burke-Ernzerhof (PBE) generalized-gradient approximation (GGA) [23] using

the NRLMOL code [50, 51, 52]. Our DFT calculation without SIC shows that the singlet state has a lower energy than the triplet state (by 0.39 eV). This trend agrees with the literature [47]. The optimized singlet structure has slightly reduced Cu-S bond lengths such as 2.223 and 2.228 Å(compared to those for **Q-2**) with the S-Cu-S angles of 89.3 and 90.7°. An experimental crystallographic data on a similar monoanionic Cu-based molecule, $[Cu(C_{14}H_{20}S_2)_2]^{1-}$ suggests that the Cu-S bond lengths are 2.16 and 2.17 Å in the singlet state [48], which agrees with the reported experimental Cu-S bond lengths in **Q-1** [47]. In our study, we use the PBE-GGA-optimized geometry for **Q-1** that has inversion symmetry up to the precision of $\sim 10^{-4}$Å and approximate D_{2h} symmetry. The coordinates of the optimized geometry are listed in Table 2.7 in the Appendix 2.8.1.

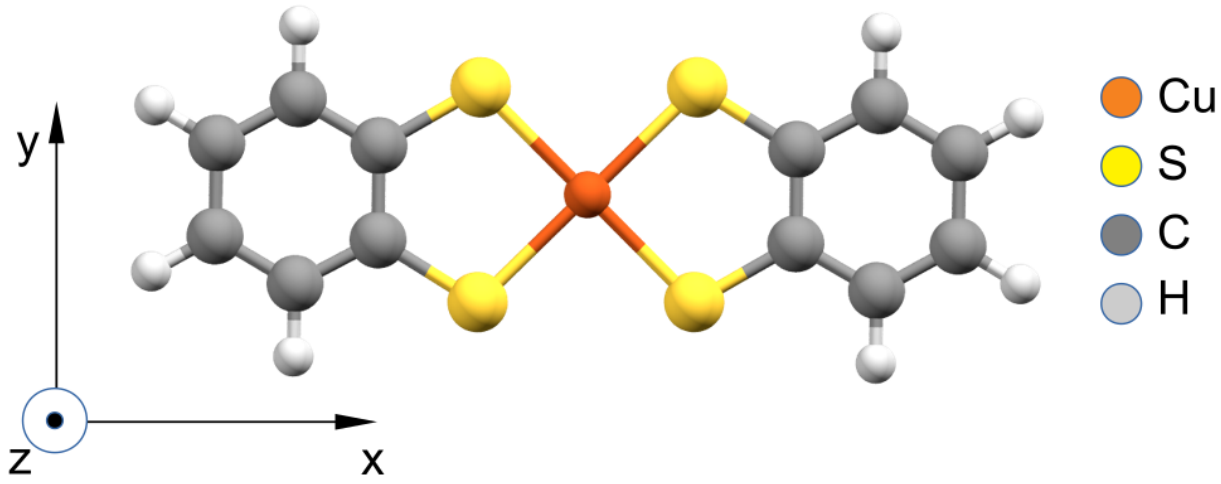

Figure 2.1: Molecular geometry of $[Cu(C_6H_4S_2)_2]^{2-}$ (**Q-2**) from the experimental data [47]. The molecule is almost planar in the xy plane. **Q-1** has a similar molecular geometry to **Q-2**.

2.3 FLO-SIC Methods

2.3.1 FLO-SIC formulation

In order to include the SIC in an approximate exchange-correlation energy $E_{\rm xc}^{\rm app}[n_\uparrow, n_\downarrow]$, Perdew and Zunger [28] considered the following self-interaction corrected exchange-correlation energy $E_{\rm xc}^{\rm SIC}$:

$$E_{\rm xc}^{\rm SIC} = E_{\rm xc}^{\rm app}[n_\uparrow, n_\downarrow] - \sum_{i,\sigma}(U^{\rm s}[n_{i\sigma}] + E_{\rm xc}^{\rm app}[n_{i\sigma}, 0]), \tag{2.1}$$

$$n_\sigma(\boldsymbol{r}) = \sum_i |\phi_{i\sigma}(\boldsymbol{r})|^2 = \sum_\alpha |\psi_{\alpha\sigma}(\boldsymbol{r})|^2, \tag{2.2}$$

where $\phi_{i\sigma}(\boldsymbol{r})$ and $\psi_{\alpha\sigma}(\boldsymbol{r})$ are localized occupied orbitals and canonical (Kohn-Sham) orbitals, respectively, and $n_{i\sigma=\uparrow,\downarrow}(\boldsymbol{r}) = |\phi_{i\sigma}(\boldsymbol{r})|^2$. By definition, the self-direct Coulomb energy $U^{\rm s}[n_{i\sigma}]$ of a single fully occupied electron must completely cancel its exact exchange-correlation energy $E_{\rm xc}[n_{i\sigma}, 0]$. However, the exact cancellation is not achieved within approximate exchange-correlation functionals, and Eq. (3.7) takes care of the incomplete cancellation. The SIC energy $E_{\rm xc}^{\rm SIC}$ depends on both the electron density and the orbitals rather than just the electron density.

In the FLO-SIC method [31, 33, 37], in order to maintain unitary invariance of the SIC energy with respect to orbital transformations, Eq. (3.7), a set of Fermi orbitals $F_{i\sigma}(\boldsymbol{r})$ are constructed from an initial set of Kohn-Sham orbitals $\psi_{\alpha\sigma}(\boldsymbol{r})$ as follows:

$$F_{i\sigma}(\boldsymbol{r}) = \frac{\sum_\alpha \psi_{\alpha\sigma}(\boldsymbol{a}_{i\sigma})\psi_{\alpha\sigma}(\boldsymbol{r})}{\sqrt{\sum_\alpha |\psi_{\alpha\sigma}(\boldsymbol{a}_{i\sigma})|^2}}, \tag{2.3}$$

where the index i runs over all occupied orbitals. Here $\boldsymbol{a}_{i\sigma}$ are three-dimensional spatial coordinates assigned to each occupied orbital i with spin σ, which are referred to as Fermi-

orbital descriptor (FOD). Unitary invariance is assured since any set of orthonormal orbitals that span the occupied space can be used in Eq. (3.9). Note that chemical properties of systems are reflected in the optimized FODs. Equation (3.9) ensures localization and the Löwdin scheme [32] guarantees orthonormality of orbitals. The constructed orbitals are referred to as Fermi-Löwdin orbitals (FLO). The localized orbitals are used to ensure size consistency of the SIC energy. The total energy including the SIC energy must be minimized both with respect to the density, through standard self-consistent calculations, and with respect to FOD positions.

The FLO-SIC calculations are performed using the FLOSIC 0.2 program [53], which is based on the NRLMOL code [50, 51, 52]. We use the Gaussian-type basis sets optimized by Pederson and Porezag [54]. Typically, a SIC-free DFT calculation within the L(S)DA-PW92 [20] or PBE-GGA exchange-correlation functional is first carried out to obtain the converged electron density and an initial set of Kohn-Sham orbitals. Then for the given electron density, an initial set of FLOs is constructed using the Kohn-Sham orbitals and an initial set of FODs [Eq. (3.9)]. Next the SIC energy is computed and the electron density is updated in a self-consistent-field (SCF) loop within the L(S)DA-PW92 exchange-correlation functional including the one-electron SIC potentials. Using the updated electron density, the set of the FOD positions is updated with a gradient-based optimization algorithm using analytic FOD forces [37]. This procedure is repeated until the total energy including the SIC energy reaches a minimum and the maximum force on the FODs is less than a tolerance.

2.3.2 Frozen-density loop method

For large molecules especially including transition-metal elements, many starting sets of FODs may need to be considered in FLO-SIC calculations, and the convergence of the total

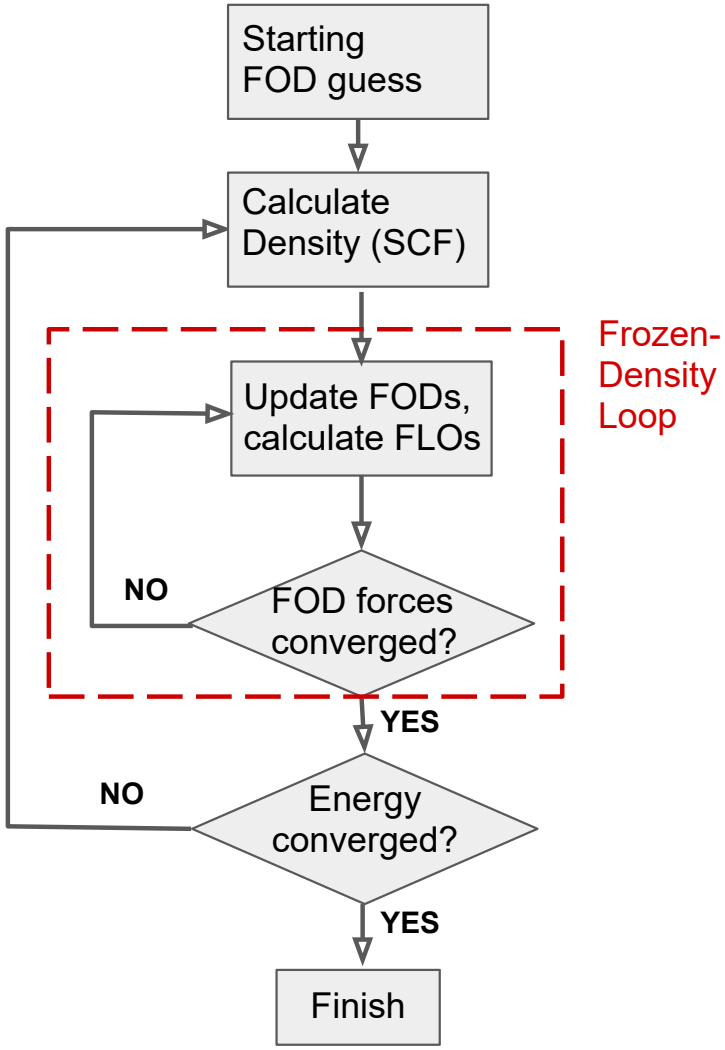

Figure 2.2: Schematic flow chart of the frozen-density loop procedure within the FLO-SIC method.

energy with respect to the FODs is known to be much slower than the electronic convergence of a SIC-free DFT SCF run. Therefore, there is a great demand for expediting FLO-SIC calculations. We apply the following modification to the FLO-SIC method. Instead of re-optimizing the electron density within a SCF loop after every FOD update, the density is held fixed (frozen) while the SIC energy is minimized with respect to FOD positions only. When the FOD geometry converges with the given FOD force tolerance (0.5 mHa/a_B) in

our calculations, the electron density is recalculated self-consistently with the new converged FOD positions, and the procedure is repeated until the total energy converges. In this method referred to as frozen-density loop algorithm (Fig. 2.2), a full FOD optimization is performed for each SCF density. We find the frozen density scheme to be significantly more efficient, saving up to a factor of six in total computational effort for the dianonic Cu-based molecule consisting of 175 electrons. The saving does not result from a decrease in the number of steps in the gradient optimization of the FODs, which is roughly the same in each approach. Instead, it derives from taking many fewer density optimization steps overall in the frozen density approach.

2.3.3 Starting sets of FODs for the Q-2 molecule

Multiple local minima in total energy may be possible in the FOD optimization [34]. In order to ensure that we reach the minimum-energy FOD configuration, we consider multiple starting sets of FODs described in this subsection. Since the number of three-dimensional FOD position vectors equals the number of electrons, we need 175 initial FOD vectors for the **Q-2** molecule which consists of 88 spin-up (majority-spin) and 87 spin-down (minority-spin) FODs. Previous FLO-SIC studies showed that starting sets of FODs of ligands (i.e., *s*- and *p*-electron systems) generated by the Monte-Carlo-based fodMC code [44] converge rapidly to the minimum SIC energy, whereas effectiveness of the fodMC code for transition-metal systems is not guaranteed. FOD positions associated with or around the transition-metal centers are also known to converge extremely slowly despite the fact that these FOD forces are largest. Therefore, for the starting sets of FODs, it makes sense to treat Cu and ligand FODs separately.

We assign the initial FODs of the ligands using the fodMC code. Considering the Cu-S

bonding, we place four spin-up and four spin-down FODs at the same positions along the Cu-S bonding directions. This assignment is consistent with the majority of the spin density from the Cu center. There is one ambiguity related to the delocalized p-electrons on the benzene-like rings. One obvious way to put FODs there is to follow a classical single-double bond picture, and assign one FOD of each species to each single bond and two FODs to each double bond. Another way is to alternate, such that one C-C bond in the ring has 2 spin-up FODs and 1 spin-down FOD, and the next bond has 1 spin-up FOD and 2 spin-down FOD. The latter alternating picture is related to Linnett double-quartet theory and has been shown to achieve slightly lower energy than the former scheme [55]. Therefore, the alternating FOD pattern is used for the ligands. These starting ligand FODs are used for all the FOD configurations of the same charge state, which differ only in the Cu starting FODs.

Since the fodMC program does not guarantee good starting FOD positions for transition-metal centers, a different strategy should be used. One possibility is to use a set of pre-converged single-atom results by Kao et.al [34]. Although this could be a good starting point, it has several disadvantages. Firstly, the electronic structure of the bonded, oxidized atom differs from that of an isolated one, and so significant re-optimization of the starting positions may be expected. Secondly, it is not clear which FODs from the optimized neutral atom should be removed to create the expected oxidation state. Finally, this approach provides few possibilities to systematically probe the space of initial FOD geometries.

Another, more systematic approach is based on the following considerations. It is known from single-atom results [34] that FODs tend to group by the principal quantum numbers of orbitals they represent. For instance, in Ar atom, for each spin channel there is one FOD at the center corresponding to $1s$ orbital, 4 FODs in a shape of tetrahedron centered at the atom (for $2s$ and $2p$ orbitals), and another 4 FODs in a tetrahedron but of larger dimensions for $3s$ and $3p$ orbitals. The molecular symmetry needs to be reflected in the initial FOD

geometries. Considering that the Cu-S bond angles are close to 90°, there is an approximate 4-fold rotational symmetry of Cu atom with respect to Cu-S bonds.

Based on the above considerations, the following procedure is used for systematic generation of 12 initial Cu FODs (see Fig. 2.3):

- Identify three groups of FODs around the Cu center, distinct by the their distances to the center, following the single-atom Cu FOD result [34].
- Using these distances, consider the following number of FODs at concentric spherical shells: 1 spin-up and 1 spin-down FOD at the center ($n = 1$); 4 spin-up and 4 spin-down FODs at a smaller ($n = 2$) sphere; and 9 spin-up and 8 spin-down at the larger ($n = 3$) sphere.
- Place these FODs in a 4-fold symmetric fashion as shown in Fig. 2.3. For the $n = 2$ shell, 4 FODs are placed at the vertices of opposing tetrahedra, in each of which two edges are parallel to the molecular plane either oriented along the x and y axes or along the diagonals (i.e. Cu-S bonds); For the $n = 3$ shell, 4 FODs are above the molecular plane, forming a square, while 4 FODs are below the plane in a rhombus, with 1 spin-up FOD directly on top of the Cu site.

2.3.4 Starting sets of FODs for the Q-1 molecule

For generation of initial FODs for the **Q-1** molecule, a similar scheme to that of the **Q-2** molecule is used. The initial Cu FODs that we consider are shown in Fig. 2.4. Since the **Q-1** molecule is in a singlet state, we perform spin-unpolarized FLO-SIC calculations, where spin-up and spin-down FODs must occupy the same positions. This reduces the number of FODs and computational time by half. The results shown in Sec. 2.5 are obtained using

spin-unpolarized FLO-SIC calculations. In all other aspects, the procedure on the **Q-1** is the same as on the **Q-2** molecule.

2.4 FLO-SIC Results for the Q-2 Molecule

2.4.1 Converged FODs and energy convergence

For the 12 starting FOD configurations (Fig. 2.3) with the same DFT-converged electron density, FLO-SIC calculations are carried out using the frozen-density loop method (Fig. 2.2). After the first frozen-density loop cycle, converged FODs starting from configuration 9-12 are found to have similar total energies and similar FOD positions to FOD configuration 1-4, respectively. After the second frozen-density loop cycle, FOD configuration 1 is found to reach the same converged energy and same FOD positions as FOD configuration 4. Therefore, we continue to relax the FOD positions and the electron density only for the remaining 7 FOD configurations (configuration 2-8). After completion of 6 cycles of the frozen-density loop, we find that the SCF total energy converges within below or up to 1 mHa. Figure 2.5 shows the convergence of the SCF total energy versus FOD iteration number for configuration 2-5. The sudden drops in the energy correspond to switches between frozen-density loop cycles. Although different FOD configurations converge at different rates, configuration 2-4 seem to converge to the same total energy.

The total energy changes by about 1 mHa or less than 1 mHa after the 6-th frozen-density loop cycle compared to the energy after the 5-th cycle (see the ΔE values in Table 2.1). Therefore, we analyze our FLO-SIC results using the data obtained after the 6-th cycle. Each cycle consists of many FOD updates or iterations as shown in Fig. 2.5. Table 2.1 lists the converged total energies and maximum force components after the 6 frozen-density loop

Table 2.1: Converged SCF total energies E and maximum final force components $F_{\max}$ after the 6 frozen-density loops, and energy differences ΔE between the 6-th and 5-th frozen-density loop cycles for the configuration 2-8 (labeled in Fig. 2.3) of the **Q-2** molecule. Each frozen-density loop cycle consists of many FOD updates. For example, for the FOD configuration 2, there are 609 updates or iterations of the FODs after the 6 frozen-density loop cycles.

FOD Conf	E (Ha)	$F_{\max}$ (mHa/a_{B})	ΔE (mHa)
2	-3703.28420	0.48	-0.43
3	-3703.28421	0.48	-0.37
4	-3703.28422	0.36	-0.35
5	-3703.28054	0.37	-1.30
6	-3703.28189	0.32	-0.53
7	-3703.28401	0.42	-0.77
8	-3703.28273	0.39	-0.60

cycles. FOD configuration 4 gives the lowest energy, but the energy differences among the different FOD configurations are on the order of mHa at most. The maximum force component $F_{\max}$ is about 0.3-0.5 mHa/a_{B}, while the maximum electric dipole moment component is about 0.006-0.007 in atomic units (and the maximum dipole moment component from the SIC-free PBE-GGA is about 0.001 in atomic units).

Figure 2.6 shows the converged FOD positions of configuration 4 after the 6-th frozen-density loop cycle. The initial spin-down FOD positions significantly change upon relaxation compared to the initial spin-up FOD positions. The converged spin-up and spin-down FOD positions (starting from configuration 4) are listed in Tables 2.8 and 2.9 in the Appendix 2.8.3. Henceforth, we examine the FLO-SIC calculated electronic structure of the molecule using the electron density obtained from this converged FOD configuration. We confirm that the FLO-SIC electronic structure from the other converged FOD configurations 2, 3, 5, 6, 7, and 8 is very close to that from the converged FOD configuration 4, within our numerical accuracy (Table 2.11 in the Appendix), although the final configurations of the core and valence FODs somewhat differ from one another. We also check that the electronic

structure does not change with further relaxations of the FODs beyond the threshold and/or with further decrease of the electric dipole moment.

2.4.2 FLOSIC-calculated electronic structure

Using the FLO-SIC result, we calculate Mulliken spin populations of the Cu atom, all four S atoms, and all C atoms of the **Q-2** molecule ($S = 1/2$). We find that the majority of the spin density (67%) arises from the Cu center and the rest from the S atoms (33%) and from the C atoms (-3%). These FLO-SIC calculated values are close to the values from our UHF calculation (Table 2.2). (Different basis sets are used for the FLO-SIC and the UHF calculations as shown in Table 2.2.) Although electron correlation is not included in the UHF calculation, there is no SIE in it. Therefore, this indicates that the SIC is properly taken care of in our FLO-SIC calculation. The FLO-SIC spin populations are also close to our multiconfigurational complete active space self-consistent field (CASSCF) result, as well as a previous multireference result [46] based on complete active space second-order perturbation theory (CASPT2). Since CASPT2 includes both static and dynamic correlations, our FLO-SIC result is very encouraging. The detail of our CASSCF and UHF calculations is described in the Appendix 2.8.2.

Now we compare the FLO-SIC spin populations to those from our SIC-free DFT calculations (Table 2.2). Both LSDA-PW92 and PBE-GGA exchange correlation functionals without the SIC give rise to much more delocalized spin density with a large contribution from the S atoms (about 70%) and a much smaller contribution from the Cu center (about 30%).

We compute the energy levels of the HOMO and LUMO using the FLO-SIC result (see Table 2.3) for the **Q-2** molecule, finding that the HOMO energy is negative. This indicates that the dianionic form of the molecule can exist, which is consistent with the experimental

Table 2.2: Calculated Mulliken spin populations of the Cu, all four S and all C atoms (in units of Bohr magneton μ_B) of the **Q-2** molecule ($S = 1/2$) using different levels of computational methods with the basis sets specified below. In the CASPT2 calculation [46], the C spin population was not reported, while in the EPR experiment [47], only the spin density from the Cu d_{xy} orbital was reported. The Cu, S, and C spin populations from the FLO-SIC and SIC-free DFT calculations do not add up to 1.00 μ_B due to very small spin populations on the H atoms. All of the values are our results unless specified otherwise.

Method	Cu	S	C	Basis sets
FLO-SIC	0.67	0.33	-0.03	NRLMOL (Cu:7s5p5d, S:6s5p4d, C:5s5p4d, H: 4s4p2d)[54]
Unrestricted Hartree Fock	0.79	0.22	-0.01	ANO-RCC-VDZ (Cu:5s4p2d, S:4s3p, C:3s2p, H:2s)
CASSCF(11,11)	0.70	0.29	0.01	ANO-RCC-VDZ
CASPT2 (Ref.[46])	0.76	0.24	N/A	ANO-RCC (Cu:6s5p3d2f1g, S:5s4p2d1s, C:3s2p1d, H:1s)
SIC-free DFT (LSDA-PW92)	0.31	0.72	-0.08	NRLMOL
SIC-free DFT (PBE-GGA)	0.32	0.73	-0.12	NRLMOL
B3LYP DFT (Ref.[47])	0.24	0.76	0.00	Cu:LANL2DZ basis set & pseudopotential [56], S, C, H:6-31G*+
EPR experiment (Ref.[47])	0.51	N/A	N/A	N/A

synthesis of the dianionic **Q-2** molecule [46, 47]. The SIC-free PBE-GGA calculation provides a positive HOMO energy. The comparison between the FLO-SIC and the SIC-free DFT results shows that the SIC shifts the HOMO level downward by 5.07 eV, while it shifts the LUMO level upward by 0.71 eV. The FLO-SIC HOMO-LUMO gap is about 6.34 eV, while the corresponding gap from the SIC-free DFT is about 0.57 eV. Since the SIC potential energy is typically negative, it lowers the energies of the occupied orbitals. As a result, the HOMO-LUMO gap increases with the SIC. The small change of the LUMO level with the SIC is due to the orbital relaxation effect.

Figure 2.7 shows the HOMO and LUMO and a few other *canonical* orbitals of the **Q-2** molecule calculated from the FLO-SIC method in comparison to the PBE-GGA orbitals. The FLO-SIC HOMO looks similar to the SIC-free DFT HOMO-2, while the FLO-SIC HOMO-2 looks similar to the SIC-free DFT HOMO. The other occupied orbitals do not

Table 2.3: Contributions of the Cu d, all S p, and all C p orbitals to the HOMO and LUMO of the **Q-2** (charge $Q = -2$, $S = 1/2$) molecule calculated using the FLO-SIC method in comparison to our SIC-free PBE-GGA calculations as well as an earlier B3LYP result [47] where the orbital decomposition was not reported. In our calculations (PBE-GGA, FLO-SIC), the HOMO arises from the spin-up (majority-spin) orbital and the LUMO from the spin-down (minority-spin) orbital (see Fig. 2.7), while in the B3LYP calculation [47], both HOMO and LUMO are from the spin-down orbitals.

Method	Level	Energy(eV)	Cu d	S p	C p
FLO-SIC	HOMO	-1.99	2.2%	74%	23%
	LUMO	4.35	85%	11%	0.5%
PBE-GGA	HOMO	3.08	49%	46%	1.4%
	LUMO	3.65	57%	37%	1.5%
B3LYP [47]	HOMO	∼3.3	-	-	-
	LUMO	∼5.3	-	-	-

seem to change their overall shapes other than the energies and Cu contributions. Table 2.3 lists quantitative characteristics of the HOMO and LUMO using the FLO-SIC method and the PBE-GGA. The FLO-SIC calculation shows that the HOMO arises mainly from the spin-up S $p_{x,y}$ orbitals with significant contributions from the spin-up C $p_{x,y}$ orbitals and a tiny contribution from the spin-up Cu d_{xy} orbitals, whereas the LUMO consists of a major contribution from the spin-down Cu d_{xy} and some contributions from the spin-down S $p_{x,y}$ orbitals. These orbital characteristics are very different from those obtained using the SIC-free DFT. For the latter, both the HOMO and LUMO consist of large contributions from the Cu d_{xy} and S $p_{x,y}$ orbitals. The FLO-SIC LUMO and the SIC-free DFT HOMO and LUMO shown in Fig. 2.7 can be identified as antibonding orbitals which are combinations of the Cu d_{xy} and the S $p_{x,y}$ orbitals. The CASSCF calculation shows that the singly occupied active orbital of the lowest-energy configuration has the character of the majority-spin (spin-up) Cu-S antibonding orbital (molecular orbital 6 in Fig. 2.12) and it can be viewed as the HOMO at the single-electron picture.

In order to understand the effect of FLO-SIC on the HOMO and other occupied orbitals, we plot the densities of states (DOS) projected onto spin-up and spin-down Cu d, S p, and C p

orbitals, as shown in Fig. 2.8. From the comparison between the FLO-SIC and the SIC-free DFT DOS plots, we find that the SIC lowers the occupied S p and C p orbitals by about 5 eV and the occupied Cu spin-up $3d$ orbitals by about 14-15 eV. The SIC effect is expected to be stronger for the $3d$ orbitals than for the p orbitals since the $3d$ orbitals are more strongly localized, i.e., larger self-interaction energy in the SIC-free DFT result. The highest occupied spin-down Cu d orbital energy is lowered by only about 6.5 eV, which is much smaller than the case of the corresponding spin-up orbital energy due to hybridization of the spin-down Cu orbital with the spin-down S p orbital. This is consistent with the PZ-SIC results of the $3d$ transition metal atoms [28] which are attributed to a more attractive exchange-correlation potential seen by the spin-up $3d$ orbitals. The characteristics of the HOMO qualitatively changes with the SIC because of the much larger downward shift of the spin-up Cu d orbitals than the S p orbitals.

2.4.3 Comparison with previous work

Experimental data [46] on the **Q-2** molecule indicates a strong covalent nature of Cu-S bonding which leads to long spin relaxation and coherence times. EPR experiments [47] imply that about 51% of the spin density arises from the Cu d_{xy} orbitals for **Q-2**. The CASPT2 calculation from Ref. [46] shows that 76% (24%) of the spin density originates from the Cu (S) atoms. Both the experimental data and the CASPT2 result suggest a majority contribution of the Cu d orbitals to the spin density, which is in line with our FLO-SIC and CASSCF spin populations. Especially, the CASPT2 [46] and our CASSCF spin populations quantitatively agree with our FLO-SIC values (see Table 2.2).

However, recent DFT calculations [47] using a hybrid functional such as Becke, 3-parameter, Lee-Yang-Parr (B3LYP) [21, 57, 58, 59], indicate that the Cu d (S p) orbitals carry 24%

(76%) of the total spin density and that both the HOMO and LUMO are from the spin-down (minority-spin) channel. The positive HOMO energy (Table 2.3) is consistent with our SIC-free PBE-GGA result. The B3LYP Cu spin density is somewhat smaller than our SIC-free DFT results, although it is expected to fall between the SIC-free DFT and the FLO-SIC values due to inclusion of a fraction of exact exchange. The deviation from this expection could arise from the fact that the B3LYP calculation [47] was done using a Cu pseudopotential [56] with different basis sets (see Table 2.2). These B3LYP results mostly do not agree even qualitatively with the experimental data or our FLO-SIC results. Note that our CASSCF result is not in line with the B3LYP result, either. In order to reconcile the discrepancy between the EPR experimental data [47] and the B3LYP result and to explain the oxidation pathway to **Q-1**, Ref. [47] alternatively proposed co-existence of the two competing iso-electronic states for Q-2 using TDDFT: $[\mathrm{Cu^{I}(bdt_2, 4S^{3-\star)}}]^{2-}$ and $[\mathrm{Cu^{II}(bdt_2, 4S^{4-}}]^2$. In the former, the four S atoms give rise to spin $S = 1/2$, while in the latter the Cu atom carries one unpaired electron. Our FLO-SIC results and multiconfigurational/multireference calculations as well as experimental data [46] support the latter state rather than the proposed co-existent states.

2.5 FLO-SIC Results for the Q-1 Molecule

Our SIC-free DFT calculations and experiments [47] on **Q-1** suggest that the singlet state has a lower energy than the triplet state. Therefore, we consider only the singlet state in the FLO-SIC calculations.

2.5.1 Converged FODs

The FLO-SIC procedure for studies of the **Q-1** molecule is similar to that described for **Q-2**. Since we carry out spin-unpolarized FLO-SIC calculations, the total number of FODs is now reduced to 87. We start with 4 initial spin-unpolarized FOD configurations as illustrated in Fig. 2.4, similarly to the case of **Q-2**. We converge the 4 initial FOD configurations through 6 individual frozen-density loop cycles. Table 2.4 lists the converged total energies and maximum force components after the 6 cycles. FOD configuration 2 gives the lowest energy, but the energy differences among the different FOD configurations are on the order of 0.1 mHa. The maximum force component $F_{\max}$ is about 1 mHa/a_{B}, while the maximum electric dipole moment component is about 0.009-0.01 in atomic units. The dipole moment is slightly larger than that for the **Q-2** molecule, which is consistent with the fact that the molecular geometry of **Q-1** was optimized without symmetry constraints. The converged FODs of configuration 2 are shown in Fig. 2.9 and the FOD positions are listed in the Appendix 2.8.3 (Table 2.10). We confirm that the FLO-SIC electronic structure from the other converged FOD configurations 1, 3, and 4 is very close to that from the converged FOD configuration 2, within our numerical accuracy (see Table 2.12 in the Appendix 2.8.4), although the final FOD configurations are somewhat different from one another. Henceforth, we analyze the FLO-SIC electronic structure obtained from the converged FOD configuration 2. Again, we check that the electronic structure does not change with further FOD relaxations or with further decrease of the dipole moment.

2.5.2 FLO-SIC calculated electronic structure

Table 2.5 shows the energies of the HOMO and LUMO of the **Q-1** molecule calculated from the FLO-SIC method. We find that the HOMO energy is -5.90 eV, which is 3.91 eV

Table 2.4: Converged SCF total energies E and maximum final force components $F_{\max}$ after the 6 frozen-density loop cycles, and energy differences ΔE between the 6-th and 5-th frozen-density loops for configuration 1-4 (labeled in Fig. 2.4) of the **Q-1** molecule. Each frozen-density loop consists of many FOD updates.

FOD Conf	E (Ha)	$F_{\max}$ (mHa/a_{B})	ΔE (mHa)
1	-3703.29260	0.35	-0.75
2	-3703.29262	0.34	-0.89
3	-3703.29231	0.28	-2.10
4	-3703.29250	0.38	-1.04

Table 2.5: Contributions of the Cu d, all S p, and all C p orbitals to the HOMO and LUMO of the **Q-1** (charge $Q = -1$, $S = 0$) molecule calculated using the FLO-SIC method compared to our SIC-free PBE-GGA calculation as well as two B3LYP results [47, 48]. In the former B3LYP calculation, the orbital decomposition was not quantified, while the latter B3LYP result is for a monoanionic Cu-based molecule with similar (slightly different) ligands, $[\mathrm{Cu(III)}(\mathrm{C_{14}H_{20}S_2})_2]^{1-}$, [48], where the HOMO and LUMO energies were not reported. See Fig. 2.10) for the HOMO and LUMO from the FLO-SIC and PBE-GGA calculations.

Method	Level	Energy(eV)	Cu d	S p	C p
FLO-SIC	HOMO	-5.90	1.6%	67%	31%
	LUMO	-1.22	68%	27%	0.8%
PBE-GGA	HOMO	-1.29	15%	60%	24%
	LUMO	-0.75	43%	51%	1.7%
B3LYP [47]	HOMO	$\sim$-1.5	-	-	-
	LUMO	$\sim$-0.5	-	-	-
B3LYP [48]	HOMO	-	11%	58%	27%
	LUMO	-	33%	58%	4%

lower than the HOMO energy of the **Q-2** molecule. The SIC shifts the HOMO (LUMO) level downward by 4.61 (0.67) eV in comparison to the SIC-free DFT results, such that it increases the HOMO-LUMO gap to 4.68 eV.

Figure 2.10 shows the HOMO and LUMO and a few other *canonical* orbitals of the **Q-1** molecule calculated from the FLO-SIC method compared to the SIC-free PBE-GGA orbitals. The overall orbital shapes do not change much upon the FLO-SIC. The FLO-SIC calculation shows that the major contributions to the HOMO originate from the S p_z and C p_z orbitals at

a ratio of almost 2:1 with a very small contribution from the Cu d orbitals, while a majority contribution to the LUMO arises from the Cu d_{xy} and S $p_{x,y}$ orbitals with an approximate ratio of 2:1 (see Table 2.5). These characteristics somewhat differ from those of the SIC-free PBE-GGA results where the HOMO carries a significant contribution from the Cu d_{xz} orbitals and the LUMO originates from almost equal contributions of Cu d and S p orbitals. The canonical orbitals away from the HOMO and LUMO from the FLO-SIC method are very similar to those from the SIC-free PBE-GGA (Fig. 2.10).

We plot the DOS projected onto Cu d, S p, and C p orbitals obtained using the FLO-SIC method and the SIC-free DFT (see Fig. 2.11). We find that the SIC lowers the occupied S p and C p orbitals by about 5 eV and most of the Cu $3d$ orbitals by 14-15 eV, which is similar to the case of **Q-2**. Interestingly, for the occupied Cu d orbitals hybridized with the ligands, the energy shift by the SIC is smaller, 9 eV. For **Q-1**, the HOMO character obtained from the FLO-SIC is similar to that from the SIC-free DFT because a much smaller contribution of the Cu d orbitals to the HOMO.

2.5.3 Comparison with previous work

We now compare our FLO-SIC calculated results with the previous experimental and theoretical work [47, 48] for **Q-1**. The characteristics and energies of the FLO-SIC HOMO and LUMO are quite different from the B3LYP results [47] (see Table 2.5) which are closer to the SIC-free PBE-GGA calculation. Interestingly, the B3LYP HOMO-LUMO gap for **Q-1** is smaller than that for **Q-2** by about 1 eV. This feature is similar to the FLO-SIC result, although the gap difference is larger in the FLO-SIC case ($\sim$1.66 eV). The experimental UV-optical absorption spectra [47] show a maximum peak at 398 nm (3.1 eV) for **Q-1** and a peak at 348 nm (3.6 eV) and possible peaks below 270 nm (4.6 eV) for **Q-2**. Although the optical

gap is not equivalent to the HOMO-LUMO gap [60], it does provide some indication of the gap size. The difference in the observed gaps is thus consistent with the FLO-SIC HOMO-LUMO gap being smaller in **Q-1**. Our results are also compared with the monoanionic Cu-based molecule with similar (slightly different) ligands such as $[Cu(III)(C_{14}H_{20}S_2)_2]^{1-}$ [48]. A previous B3LYP DFT calculation [48] on this monoanionic molecule with the scalar relativistic zero-order regular approximation (ZORA) showed that the HOMO consists of Cu d_{xz} (11%), S p_z (58%), and C p_z (27%), while the LUMO consists of Cu d_{xy} (33%), S p_z (58%), and C p_z (4%). Despite slightly different ligands, this orbital decomposition is consistent with our SIC-free PBE-GGA result (see Table 2.5).

2.6 Conclusions and Outlook

We have investigated the dianionic and monoanionic states of the mononuclear Cu-based molecule which has potential applications for quantum information science, using the FLO-SIC method. Starting with the SIC-free DFT-converged electron density and with multiple initial sets of FODs within the frozen-density loop approach, we determined optimal FLOs with which the SIC energy was obtained self-consistently. Although different initial sets of FODs converged to somewhat different final FOD positions (core and valence FODs), the electronic and magnetic properties obtained from the multiple final converged FODs are very similar to one another within our numerical accuracy. This may suggest an importance of the starting electron density in the FLO-SIC calculations.

As expected, the SIC potential in the FLO-SIC method remedies the severe delocalization of electric charge and spin density caused by the SIE. The FLO-SIC calculations show that in the dianionic case, about 67% of the spin density arises from the Cu d orbitals and about 33% of the spin density is from the S p orbitals. This feature quantitatively agrees with the

multireference result [46] and our multiconfigurational calculation, while the SIC-free PBE-GGA and B3LYP functionals severely underestimate the spin density of the Cu d orbitals. The trend that we found needs to be checked for other transition-metal based molecules with covalent or ionic metal-ligand bonding. It is known that discrepancy between experimental and DFT exchange coupling constants in $3d$ transition-metal systems, especially overestimation (without sign flip), may be mainly attributed to highly delocalized spin density of the transition-metal d orbitals [61]. Considering this, our results suggest that the FLO-SIC method may be overall effective in accurately describing the magnetic exchange coupling between $3d$ transition metal centers within multinuclear magnetic systems [41, 43].

The SIC potential lowers the energies of the Cu d orbitals by a large amount, which ended up with large changes of the HOMO character compared to the SIC-free DFT result. Whether the FLO-SIC HOMO character is adequate or not requires further studies using more advanced FLO-SIC methods. Utilization of complex orbitals in FLO-SIC calculations [62, 63] may improve the FOD optimization process and provide a better description of systems involving transition metals. It is shown that local scaling SIC appears important in preventing overcorrection of some properties such as polarizabilities and atomization energies [64]. However, there has been so far no studies of the local scaling SIC effect on the characteristics of the HOMO, which would be also interesting to investigate.

2.7 Acknowledgements

This work was funded by the Department of Energy Basic Energy Sciences grant numbers DE-SC0019033 and DE-SC0018331. The computational support was provided by the Virginia Tech Advanced Research Computing and the Extreme Science and Engineering Discovery Environment (XSEDE) under Project number DMR060009N, which is supported

by the National Science Foundation Grant number ACI-1548562. We are grateful to Mark Pederson, Tunna Baruah, and Rajendra Zope for their extensive help in using and troubleshooting the FLOSIC code. We are also grateful to Kai Trepte for the discussion and for providing us with the frozen-density loop functionality and the fodMC code, and we thank Aleksander Wysocki for helping us set up the CASSCF calculation.

Data Availability

The data that support the findings of this study are available within the article and the Appendices.

2.8 Appendix

2.8.1 Molecular Geometries

Tables 2.6 and 2.7 provide the coordinates for the dianionic (Q-2 and)the monoanionic mole (Q-1c)ules, respectively.

2.8.2 CASSCF and UHF calculations for Q-2

We perform CASSCF calculations of the **Q-2** molecule in the doublet state ($S = 1/2$) with the active space consisting of 11 electrons and 11 orbitals using *ab-initio* code MOLCAS version 8.2 [65]. The 11 active orbitals comprise five Cu 3d orbitals, five Cu 4d (or *d-shell) orbitals, and one Cu-S bonding orbital. Among the five Cu 3d orbitals, one Cu-S antibonding orbital is included. The total number of electrons in the active space is counted considering

Table 2.6: Geometry of the dianionic Cu-based molecule in units of a_B.

Species	x	y	z
Cu	0.0000	0.0000	0.0000
S	-3.0951	-3.0344	0.0000
S	-3.0190	3.0345	0.0000
S	3.0952	3.0345	0.0000
S	3.0191	-3.0344	0.0000
C	-5.9033	-1.2856	-0.1936
C	-5.8796	1.3796	-0.1871
C	-10.4423	1.4295	-0.5952
C	-8.2349	-2.5282	-0.3794
C	-8.1540	2.6950	-0.3968
C	-10.4902	-1.1919	-0.5795
C	5.9034	1.2857	0.1936
C	5.8797	-1.3794	0.1872
C	10.4424	-1.4294	0.5952
C	8.2350	2.5284	0.3794
C	8.1540	-2.6948	0.3968
C	10.4903	1.1920	0.5795
H	-12.1979	2.4933	-0.7648
H	-8.2819	-4.5875	-0.3674
H	-8.1318	4.7546	-0.4054
H	-12.2829	-2.1959	-0.7228
H	12.1981	-2.4933	0.7647
H	8.2820	4.5877	0.3675
H	8.1319	-4.7545	0.4054
H	12.2830	2.1960	0.7228

the doubly occupied Cu-S bonding orbital (Cu $3d_{xy}$ and S $3p_{x,y}$) and nine electrons from the five Cu $3d$. The 11 active molecular orbitals with their state-averaged occupation numbers are shown in Fig. 2.12. Scalar relativistic effects are included based on the Douglas-Kroll-Hess Hamiltonian [66, 67] using relativistically contracted atomic natural orbital (ANO-RCC) basis sets [68, 69]. For all elements, we use the valence double-ζ quality (ANO-RCC-VDZ) basis sets provided in MOLCAS code. Considering the five possibilities of creating a hole in the $3d$ orbitals, we carried out the state average over 5 roots. From the CASSCF(11,11) calculations, we find that the ground state (lowest-energy root) has a configuration of the

Table 2.7: Optimized geometry of the monoanionic Cu-based molecule in units of a_B.

Species	x	y	z
Cu	0.0000	0.0000	0.0000
S	-2.9880	-2.9518	-0.0110
S	-2.9198	3.0322	-0.0118
S	2.9882	2.9518	0.0110
S	2.9199	-3.0323	0.0119
C	-5.8516	-1.2592	-0.2332
C	-5.8220	1.4049	-0.2436
C	-10.4096	1.4425	-0.5731
C	-8.1679	-2.5462	-0.3861
C	-8.1134	2.7386	-0.4114
C	-10.4360	-1.2061	-0.5607
C	5.8517	1.2592	0.2332
C	5.8221	-1.4050	0.2436
C	10.4096	-1.4425	0.5730
C	8.1680	2.5461	0.3861
C	8.1136	-2.7387	0.4113
C	10.4361	1.2060	0.5607
H	-12.1754	2.5014	-0.7241
H	-8.1697	-4.6106	-0.3740
H	-8.0702	4.8022	-0.4181
H	-12.2161	-2.2373	-0.7134
H	12.1755	-2.5014	0.7241
H	8.1698	4.6106	0.3740
H	8.0703	-4.8023	0.4181
H	12.2161	2.2373	0.7134

doubly occupied Cu-S bonding orbital (MO 1: Cu $3d_{xy}$ and S $3p_{x,y}$), the four doubly occupied Cu $3d$ orbitals (MO 2-5: d_{z^2}, $d_{x^2-y^2}$, d_{yz}, d_{xz}), the singly occupied Cu-S antibonding orbital (MO 6: Cu $3d_{xy}$ and S $3p_{x,y}$), and empty Cu $4d$ orbitals (MO 7-11).

Unrestricted Hartree-Fock (UHF) calculations are performed for the **Q-2** molecule in the doublet state ($S = 1/2$) using MOLCAS version 8.2 [65]. We use ANO-RCC-VDZ basis sets for all the atoms.

2.8.3 Converged FOD Geometries

Dianionic molecule: FOD Configuration 4

Table 2.8: Converged geometry of spin-up FODs (configuration 4) for **Q-2** in units of a_B.

Spin UP			
Orb. Type	x	y	z
Cu 1s	0.000000	0.000000	0.000000
Cu 2sp	0.140437	-0.006153	0.121301
	-0.147459	0.008121	0.111994
	0.011429	0.166278	-0.123538
	-0.004199	-0.168263	-0.121273
Cu 3spd	0.533382	0.563552	0.363919
	-0.548512	-0.557042	0.344983
	-0.500887	0.606451	0.338860
	0.483260	-0.600871	0.370400
	0.721904	-0.035822	-0.585479
	-0.694333	0.026664	-0.625292
	0.027308	0.407041	-0.382308
	-0.008506	-0.412614	-0.377110
	-0.015814	0.004469	0.728797

Continued on the next column

Continuation of Table 2.8			
Orb. Type	x	y	z
Cu-S bonds	-2.111473	-1.842142	0.068512
	-2.076545	1.810656	0.109787
	2.099305	1.864911	0.265062
	2.068580	-1.828072	0.242089
Ligands	-3.095100	-3.034400	0.000000
	-3.101429	-2.765981	-0.391111
	-2.723407	-3.305934	0.045615
	-3.429507	-3.361022	0.015010
	-3.128710	-2.693342	0.330667
	-4.562630	-2.068162	-0.111434
	-3.208291	-3.910813	-1.368258
	-3.322393	-3.873760	1.378195
	-3.019000	3.034500	0.000000
	-3.056048	2.695316	0.332578
	-2.644963	3.302568	0.042083
	-3.025741	2.766809	-0.391055
	-3.352441	3.361822	0.017076
	-4.515427	2.118259	-0.105528
	-3.208008	3.914183	1.359502
	-3.085594	3.878898	-1.394130
	-5.903300	-1.285600	-0.193600
	-5.834331	0.047515	-1.226000

Continued on the next column

Continuation of Table 2.8

Orb. Type	x	y	z
	-6.046157	0.049012	0.975923
	-7.017290	-2.002031	-0.273916
	-5.879600	1.379600	-0.187100
	-6.963985	2.128132	-0.275508
	-10.442300	1.429500	-0.595200
	-9.253654	1.997210	-1.351158
	-9.399692	1.987056	0.359386
	-10.613748	0.121326	-0.590620
	-11.901501	2.120958	-0.748147
	-8.234900	-2.528200	-0.379400
	-9.324935	-1.804501	-1.340106
	-9.455418	-1.771954	0.364704
	-8.109587	-4.142157	-0.371431
	-8.154000	2.695000	-0.396800
	-7.974475	4.304984	-0.405633
	-10.490200	-1.191900	-0.579500
	-11.975389	-1.834973	-0.715014
	3.095200	3.034500	0.000000
	3.118318	2.776295	0.397660
	2.721877	3.298697	-0.061242
	3.431148	3.358185	-0.005696
	3.112116	2.694790	-0.327862

Continued on the next column

Continuation of Table 2.8			
Orb. Type	x	y	z
	4.567332	2.067120	0.092021
	3.239123	4.127233	1.197780
	3.281845	3.624508	-1.524598
	3.019100	-3.034400	0.000000
	3.036860	-2.694898	-0.329390
	2.644071	-3.296117	-0.061708
	3.044641	-2.776198	0.398150
	3.354005	-3.359786	-0.004370
	4.517107	-2.116384	0.083802
	3.183481	-3.654536	-1.512668
	3.105700	-4.110867	1.215247
	5.903400	1.285700	0.193600
	5.855322	-0.047856	1.271607
	6.013191	-0.048392	-0.924280
	7.016180	2.002949	0.282524
	5.879700	-1.379400	0.187200
	6.963033	-2.128481	0.284354
	10.442400	-1.429400	0.595200
	9.247638	-1.983879	1.356095
	9.406294	-1.999631	-0.356898
	10.611694	-0.121133	0.600671
	11.901929	-2.122664	0.730683

Continued on the next column

Continuation of Table 2.8			
Orb. Type	x	y	z
	8.235000	2.528400	0.379400
	9.318521	1.791676	1.345438
	9.462484	1.784652	-0.362645
	8.111172	4.141376	0.353021
	8.154000	-2.694800	0.396800
	7.976123	-4.304237	0.387162
	10.490300	1.192000	0.579500
	11.975580	1.836666	0.697490

Table 2.9: Converged geometry of spin-down FODs (configuration 4) for **Q-2** in units of a_{B}.

Spin DOWN			
Orb. Type	x	y	z
Cu 1s	0.000000	0.000000	0.000000
Cu 2sp	0.130298	-0.027391	-0.156584
	-0.174223	-0.026294	-0.059652
	0.016902	0.176076	0.058717
	0.031878	-0.127228	0.157324
Cu 3spd	0.840120	0.011401	0.249996
	-0.755827	-0.015060	0.262829
Continued on the next column			

Continuation of Table 2.9			
Orb. Type	x	y	z
Cu 3spd	-0.034422	0.415893	0.654691
	0.011549	-0.310753	0.473532
	0.310661	-0.011339	-0.470749
	-0.421930	0.035834	-0.668717
	0.012690	0.749680	-0.259756
	-0.003356	-0.840355	-0.247173
Cu-S bonds	-1.944906	-1.856133	-0.108011
	-1.889778	1.810019	-0.024370
	1.968248	1.831567	0.075125
	1.869221	-1.791551	0.012073
Ligands	-3.095100	-3.034400	0.000000
	-3.104623	-2.792723	-0.399787
	-2.713020	-3.281980	0.047461
	-3.124771	-2.714818	0.339812
	-3.442438	-3.342633	0.012001
	-3.091948	-3.953547	-1.367253
	-3.249423	-3.711402	1.507150
	-3.019000	3.034500	0.000000
	-3.031520	2.795520	-0.397043
	-2.635299	3.275305	0.043065
	-3.050727	2.720721	0.340219
	-3.362062	3.341376	0.013373

Continued on the next column

Continuation of Table 2.9

Orb. Type	x	y	z
	-3.146003	3.787235	1.500560
	-3.013779	3.960913	-1.402001
	-5.903300	-1.285600	-0.193600
	-4.577437	-1.995539	-0.094181
	-5.879600	1.379600	-0.187100
	-4.545042	2.045505	-0.094045
	-5.696598	0.044912	-0.172740
	-10.442300	1.429500	-0.595200
	-8.234900	-2.528200	-0.379400
	-7.105984	-1.905376	-1.234125
	-7.251680	-1.911673	0.660927
	-8.154000	2.695000	-0.396800
	-7.045929	2.032268	-1.250852
	-7.201763	2.052201	0.650728
	-9.338694	2.135280	-0.499804
	-10.490200	-1.191900	-0.579500
	-10.535883	0.126545	0.369795
	-10.359909	0.108835	-1.541474
	-9.405401	-1.931696	-0.482550
	-11.761447	2.344416	-0.719292
	-8.373172	-4.109167	-0.374801
	-8.236908	4.279416	-0.407785

Continued on the next column

Continuation of Table 2.9			
Orb. Type	x	y	z
	-11.841502	-2.063441	-0.684648
	3.095200	3.034500	0.000000
	3.099965	2.792682	0.399867
	2.712265	3.281476	-0.043372
	3.129430	2.716851	-0.341432
	3.443544	3.341366	-0.014693
	3.092415	3.916495	1.391044
	3.253715	3.761675	-1.484140
	3.019100	-3.034400	0.000000
	3.028511	-2.795451	0.395219
	2.635777	-3.274514	-0.039840
	3.054223	-2.722745	-0.339478
	3.361099	-3.340366	-0.015591
	3.161725	-3.825869	-1.487450
	3.012624	-3.937765	1.421397
	5.903400	1.285700	0.193600
	4.569765	1.992810	0.093496
	5.879700	-1.379400	0.187200
	4.548281	-2.047422	0.089451
	5.696742	-0.044162	0.173826
	10.442400	-1.429400	0.595200
	8.235000	2.528400	0.379400

Continued on the next column

Continuation of Table 2.9			
Orb. Type	x	y	z
	7.103359	1.906668	1.225390
	7.256631	1.910027	-0.670244
	8.154000	-2.694800	0.396800
	7.043586	-2.032815	1.243270
	7.205103	-2.051525	-0.660238
	9.338475	-2.134622	0.499690
	10.490300	1.192000	0.579500
	10.534110	-0.126374	-0.372469
	10.362186	-0.109057	1.541334
	9.405378	1.931580	0.482034
	11.761808	-2.343494	0.721289
	8.372809	4.109440	0.375394
	8.235965	-4.279196	0.407798
	11.841594	2.062818	0.686736

Monoanionic molecule: FOD Configuration 2

Table 2.10: Converged FOD geometry of configuration 2 for **Q-1** in units of a_B

Orb. Type	x	y	z
Cu 1s	0.000000	0.000000	0.000000
Cu 2sp	0.171963	-0.021944	0.068097
	-0.132286	-0.023862	0.154110
	-0.014376	0.173357	-0.067050
	-0.027987	-0.130181	-0.155197
Cu 3spd	0.394996	0.024379	0.617239
	-0.001482	-0.823311	0.249773
	-0.310798	-0.007790	0.469381
	0.746606	-0.016562	-0.261254
	0.036822	0.396496	-0.614567
	-0.820871	0.023746	-0.252955
	0.003839	0.744894	0.262968
	-0.014743	-0.308952	-0.470619
Cu-S bonds	-1.781915	-1.691625	-0.018311
	-1.791331	1.782652	-0.109085
	1.797969	1.710358	0.008900
	1.780486	-1.790712	0.093198
Ligands	-2.987407	-2.951645	-0.010186
	-3.345872	-3.242831	0.004111
	-2.595029	-3.173913	0.026158
	-3.025560	-2.657471	0.339888

Continued on the next column

Continuation of Table 2.10

Orb. Type	x	y	z
	-2.992640	-2.732125	-0.416618
	-4.531494	-2.019853	-0.133993
	-2.878634	-3.750841	-1.469355
	-3.044755	-3.598620	1.526392
	-2.919038	3.032393	-0.012400
	-2.941888	2.746792	-0.376666
	-2.568019	3.319207	0.041078
	-3.224241	3.386509	0.003995
	-2.952933	2.675032	0.286776
	-4.460880	2.143257	-0.118220
	-3.009789	3.607845	1.520725
	-2.720682	3.775947	-1.449289
	2.988705	2.951802	0.010166
	3.347068	3.240376	-0.003442
	2.991387	2.733508	0.418910
	3.025331	2.658371	-0.342131
	2.591924	3.173543	-0.026491
	4.529326	2.017766	0.138384
	2.876767	3.741768	1.470373
	3.030660	3.589093	-1.525161
	2.920530	-3.032262	0.012655
	3.218776	-3.389315	0.002669

Continued on the next column

Continuation of Table 2.10			
Orb. Type	x	y	z
	2.945682	-2.672171	-0.283756
	2.949366	-2.744008	0.373499
	2.568700	-3.323262	-0.047971
	4.460029	-2.132216	0.126484
	2.992370	-3.624563	-1.510985
	2.728562	-3.793353	1.438725
	-5.868791	-1.332683	-0.231923
	-5.922333	0.079014	0.794537
	-5.786270	0.069544	-1.306878
	-6.937767	-2.009568	-0.306224
	-5.839102	1.478004	-0.244650
	-6.898334	2.169549	-0.327058
	-10.459506	1.390212	-0.575636
	-9.194208	2.012593	-1.360434
	-9.329891	2.028817	0.374653
	-10.513841	0.119294	-0.572553
	-11.835054	2.173869	-0.687385
	-8.099575	-2.565909	-0.382148
	-9.372209	-1.804942	0.398234
	-9.233172	-1.806713	-1.329643
	-8.025888	-4.128546	-0.360571
	-8.044570	2.756914	-0.406001

Continued on the next column

Continuation of Table 2.10

Orb. Type	x	y	z
	-7.944740	4.321873	-0.402115
	-10.484763	-1.152881	-0.565010
	-11.874154	-1.913766	-0.673746
	5.869096	1.332206	0.231920
	5.925368	-0.080192	-0.804028
	5.783175	-0.070854	1.316307
	6.938917	2.008504	0.304771
	5.839239	-1.478021	0.244374
	6.901224	-2.165487	0.325413
	10.459557	-1.390233	0.575542
	9.328372	-2.027619	-0.377502
	9.193831	-2.013564	1.364061
	10.513699	-0.119602	0.571584
	11.835639	-2.173955	0.689013
	8.099563	2.565841	0.382213
	9.234255	1.807794	1.329987
	9.371656	1.803899	-0.398104
	8.025786	4.128456	0.362188
	8.044535	-2.756844	0.405958
	7.950583	-4.325674	0.404086
	10.484870	1.152872	0.565014
	11.873725	1.914077	0.675239

2.8.4 Final FOD-configuration dependence of HOMO-LUMO gap and spin density for Q-2 and Q-1

Table 2.11: Final FOD dependence of the electronic structure such as the HOMO and LUMO energies, HOMO-LUMO gap, and Mulliken spin population on the Cu and S atoms for **Q-2**. The final converged FOD configurations starting from FOD configuration 2-8 are used for the calculation.

Property	Conf.2	Conf.3	Conf.4	Conf.5	Conf.6	Conf.7	Conf.8
HOMO energy (eV)	-1.99	-1.99	-1.99	-1.99	-1.99	-1.99	-1.99
LUMO energy (eV)	4.35	4.35	4.35	4.37	4.38	4.34	4.34
HOMO-LUMO gap (eV)	6.34	6.34	6.34	6.36	6.37	6.33	6.34
Spin Cu (μ_B)	0.666	0.666	0.665	0.660	0.658	0.670	0.674
Spin S (μ_B)	0.333	0.333	0.334	0.337	0.340	0.326	0.321

Table 2.12: Final FOD dependence of the electronic structure such as the HOMO and LUMO energies and HOMO-LUMO gap for **Q-1**. The final converged FOD configurations starting from FOD configuration 1-4 are used for the calculations.

Property	Conf.1	Conf.2	Conf.3	Conf.4
HOMO energy (eV)	-5.90	-5.90	-5.90	-5.90
LUMO energy (eV)	-1.22	-1.22	-1.22	-1.22
HOMO-LUMO gap (eV)	4.68	4.68	4.68	4.68

FOD Conf.	n=2 shell		n=3 shell	
	spin-up	spin-dn	spin-up	spin-dn
1			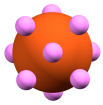	
2			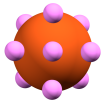	
3			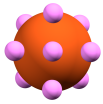	
4			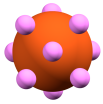	
5			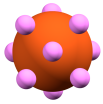	
6			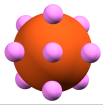	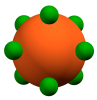
7			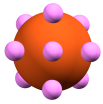	
8			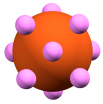	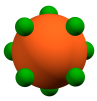
9			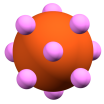	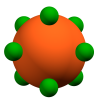
10			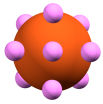	
11			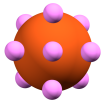	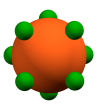
12			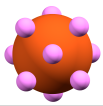	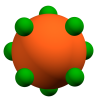

Figure 2.3: Schematic depiction of 12 starting FOD geometries associated with Cu in the **Q-2** molecule. Orange spheres represent concentric spheres around the Cu atom where magenta (green) dots are for spin-up (spin-down) FODs.

FOD Conf.	n=2 shell	n=3 shell
1		
2		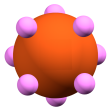
3		
4		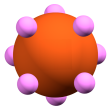

Figure 2.4: Schematic depiction of 4 starting spin-unpolarized FOD geometries associated with Cu in the **Q-1** molecule. Orange spheres represent concentric spheres around the Cu atom where magenta dots are for FODs.

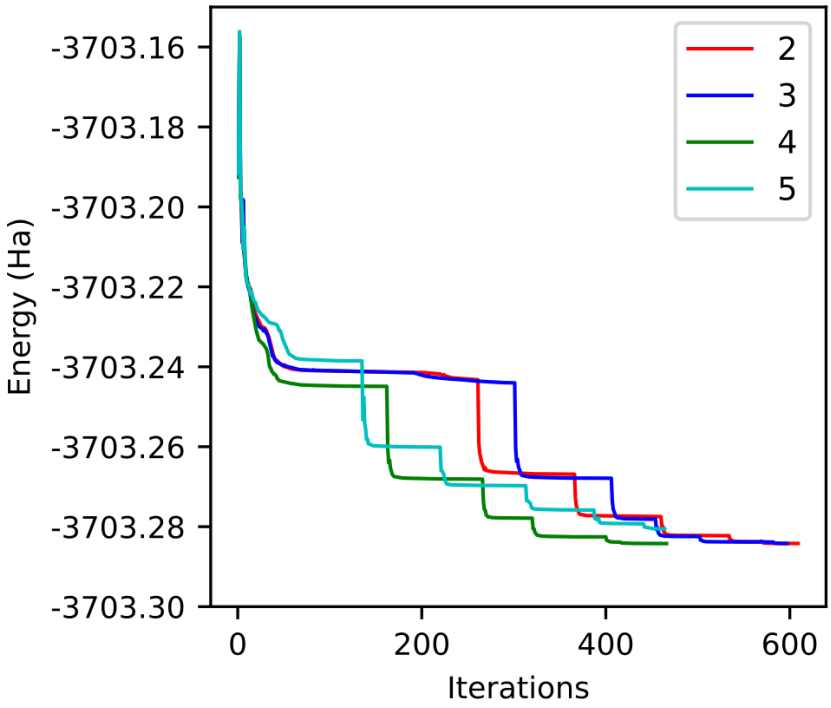

Figure 2.5: Total energy versus FOD update or iteration number for FOD configuration 2-5 (labeled in Fig. 2.3) of the **Q-2** molecule. After the initial steep relaxation of the energy, the step-function-like abrupt jump occurs whenever the electron density is updated after each frozen-density loop converges. Here 6 frozen-density loop cycles are shown.

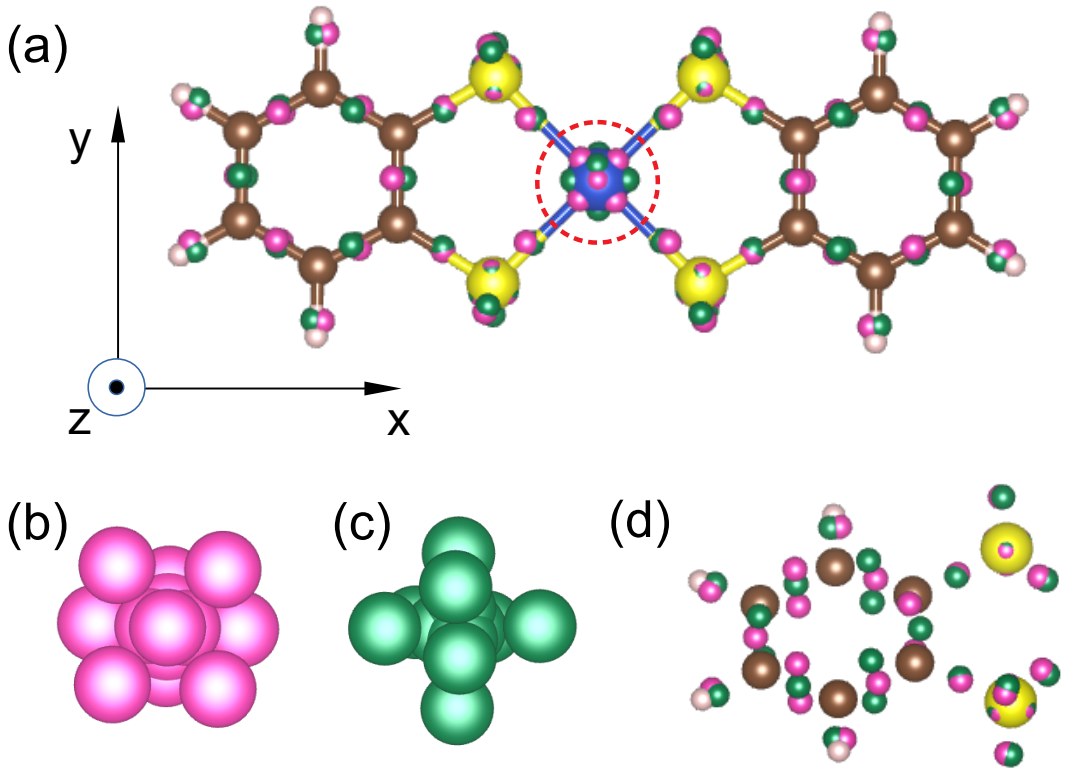

Figure 2.6: (a) Final converged FOD positions for configuration 4 of the **Q-2** molecule with magenta (green) color for spin-up (spin-down) FODs. (b) and (c) Zoom-in of the spin-up and spin-down FODs near the Cu atom. (d) Zoom-in of the spin-up and spin-down FODs near the ligands. The zoom-in region is indicated as a red dashed circle in (a).

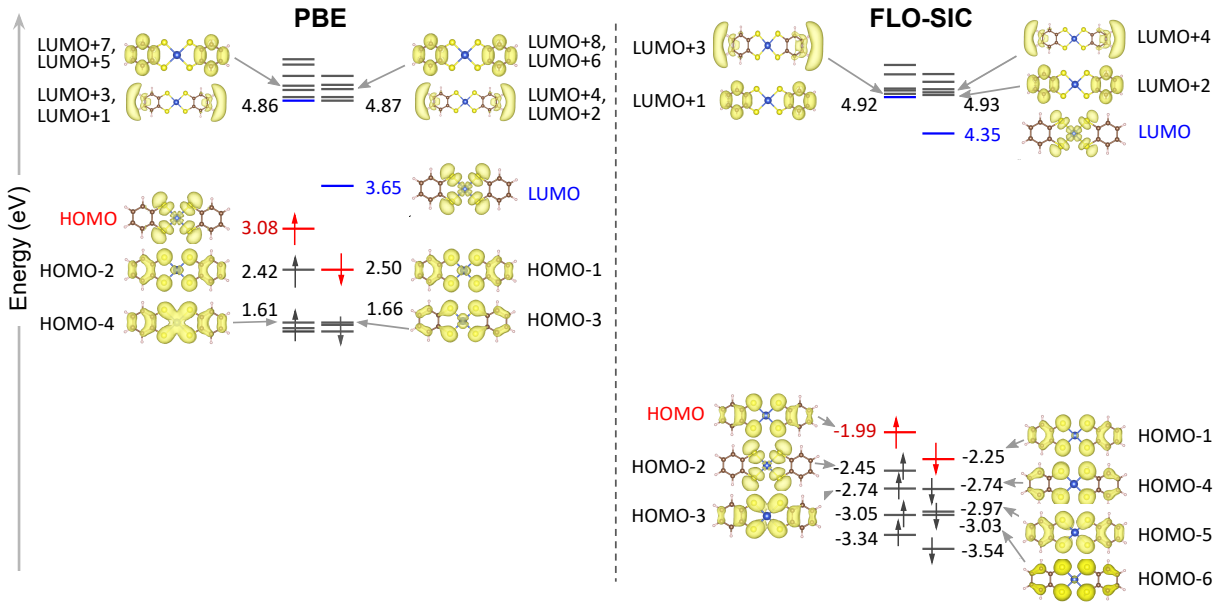

Figure 2.7: Energy levels and corresponding canonical orbitals of the **Q-2** molecule from the SIC-free PBE-GGA and FLO-SIC calculations

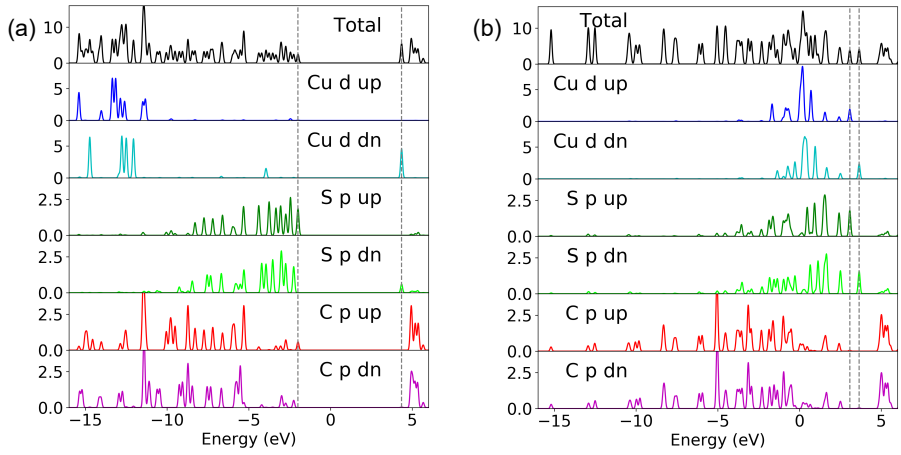

Figure 2.8: (a) FLO-SIC and (b) SIC-free DFT calculated densities of states (DOS) projected onto spin-up and spin-down Cu d, S p, and C p orbitals of the **Q-2** molecule where the left and right vertical dashed lines indicate the HOMO and LUMO levels. The FLO-SIC HOMO-LUMO gap is 6.34 eV, while the SIC-free DFT HOMO-LUMO gap is 0.56 eV.

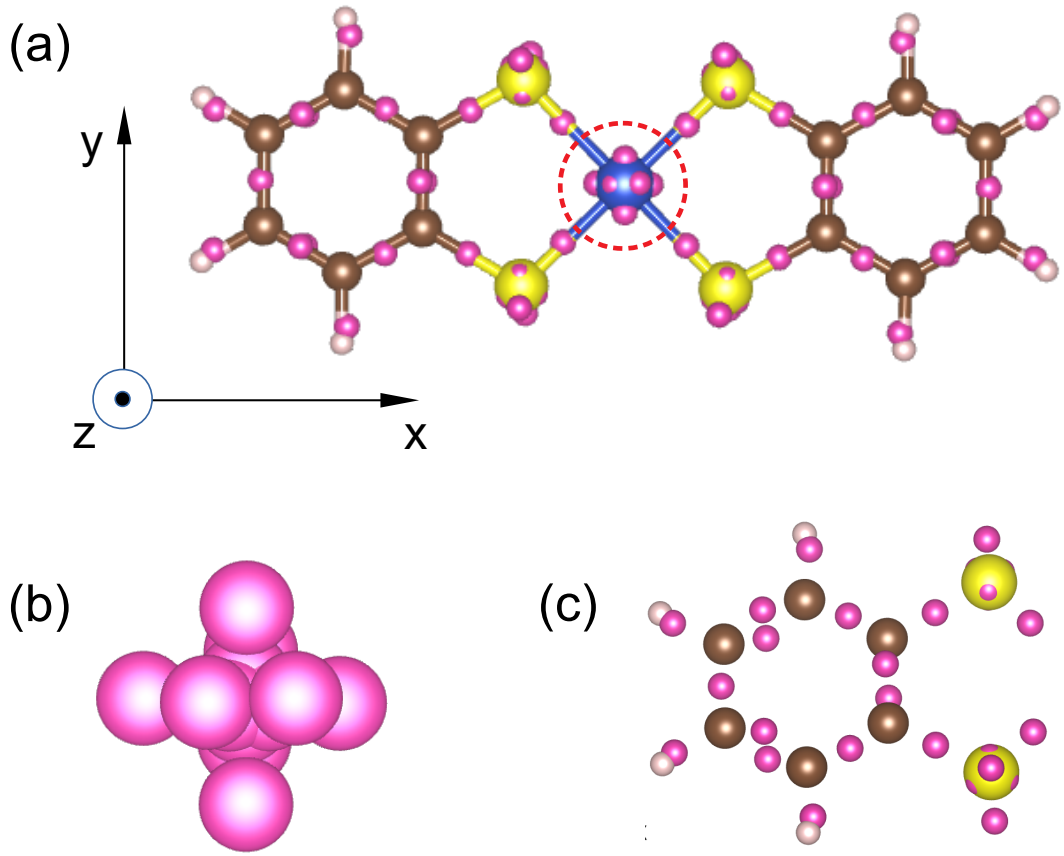

Figure 2.9: (a) Converged spin-unpolarized FOD positions from configuration 2 for the **Q-1** molecule. (b) Zoom-in of the FODs near the Cu atom and (c) zoom-in of the FODs near the ligands.

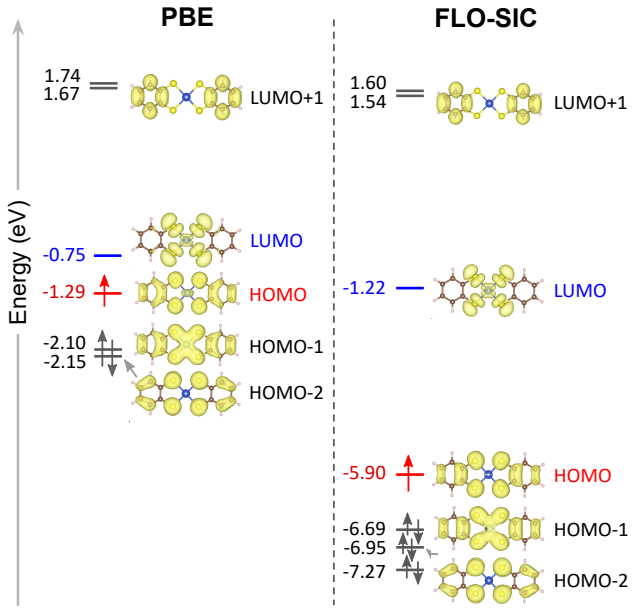

Figure 2.10: Energy levels and corresponding canonical orbitals of the **Q-1** molecule from the FLO-SIC and SIC-free PBE-GGA calculations

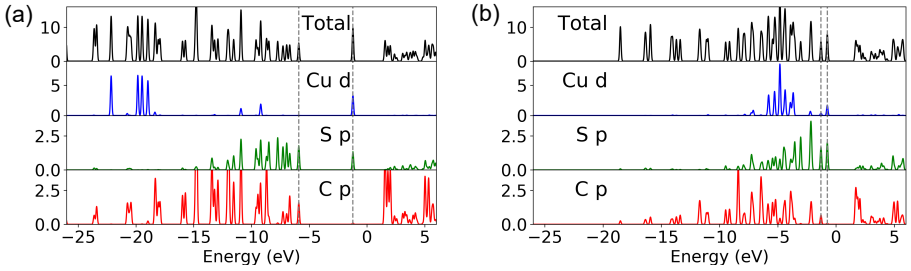

Figure 2.11: (a) FLO-SIC and (b) SIC-free DFT calculated densities of states (DOS) projected onto the Cu d, S p, and C p orbitals of the **Q-1** molecule where the left and right vertical dashed lines indicate the HOMO and LUMO levels. The FLO-SIC HOMO-LUMO gap is 4.68 eV, while the SIC-free DFT HOMO-LUMO gap is 0.54 eV.

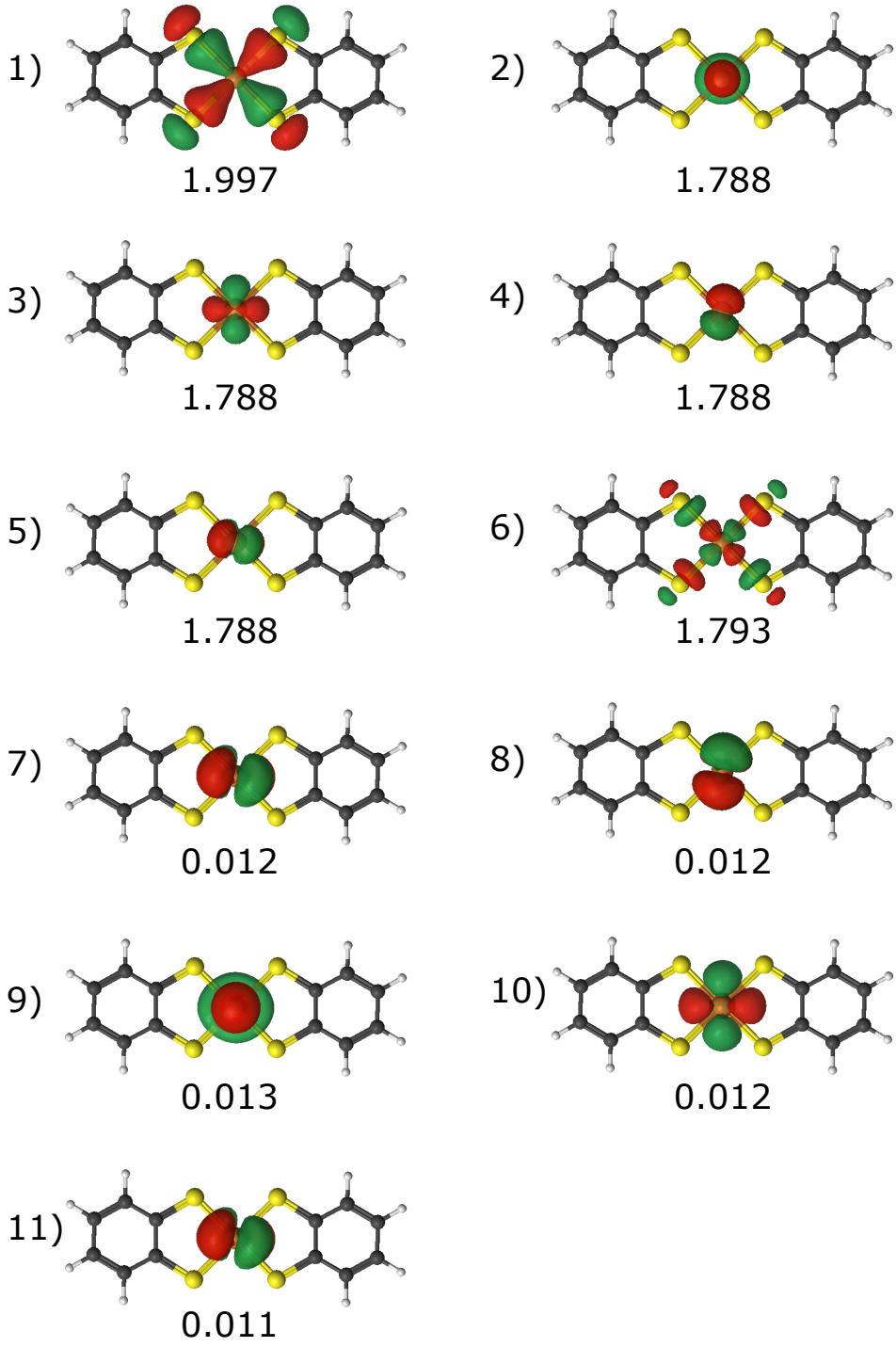

Figure 2.12: Molecular orbitals (MO) and state-averaged occupation numbers in the active space for our CASSCF(11,11) calculation of the **Q-2** molecule. The ground-state configuration consists of doubly occupied MO 1-5, singly occupied MO 6, and empty MO 7-11.

Chapter 3

Hyperfine Interactions for Small Systems including Transition-Metal Elements using FLO-SIC DFT

*This chapter was previously published. Reprinted from Anri Karanovich, Koblar Alan Jackson, and Kyungwha Park, "Hyperfine interactions for small systems including transition-metal elements using self-interaction corrected density-functional theory", J. Chem. Phys.7 July 2024; **161** (1): 014102. https://doi.org/10.1063/5.0209226* [2] *, with the permission of AIP Publishing.*

The interactions between the electronic magnetic moment and the nuclear spin moment, i.e., magnetic hyperfine (HF) interactions, play an important role in understanding electronic properties of magnetic systems and in realizing platforms for quantum information science applications. We investigate the HF interactions for atomic systems and small molecules including Ti or Mn, by using Fermi-Löwdin orbital (FLO) based self-interaction corrected (SIC) density-functional theory (DFT). We calculate the Fermi contact (FC) and spin-dipole terms for the systems within the local density approximation (LDA) in the FLO-SIC method and compare them with the corresponding values without SIC within the LDA and generalized-gradient approximation (GGA), as well as experimental data. For the moderately heavy atomic systems (atomic number $Z \leq 25$), we find that the mean absolute error of the FLO-

SIC FC term is about 27 MHz (percentage error is 6.4%), while that of the LDA and GGA results is almost double that. Therefore, in this case, the FLO-SIC results are in better agreement with the experimental data. For the non-transition-metal molecules, the FLO-SIC FC term has the mean absolute error of 68 MHz which is comparable to both the LDA and GGA results without SIC. For the seven transition-metal-based molecules, the FLO-SIC mean absolute error is 59 MHz, whereas the corresponding LDA and GGA errors are 101 and 82 MHz, respectively. Therefore, for the transition-metal-based molecules, the FLO-SIC FC term agrees better with experiment than the LDA and GGA results. We observe that the FC term from the FLO-SIC calculation is *not* necessarily larger than that from the LDA or GGA for all the considered systems due to the core spin polarization, in contrast to the expectation that SIC would increase the spin density near atomic nuclei, leading to larger FC terms.

3.1 Introduction

The interaction between the nuclear spin moment and the electronic magnetic moment, i.e., magnetic hyperfine (HF) interaction, is many orders of magnitude weaker than electronic interactions. The magnetic HF interaction can be measured by nuclear magnetic resonance [70] or electron paramagnetic resonance experiments [71, 72]. Despite the small energy scale, the magnetic HF interaction has been shown to play a crucial role in understanding electronic and magnetic properties of molecules and solids [70, 71, 72], in experimental realizations of molecular spin qubits [73, 74, 75] and quantum registers [76], and in the generations of efficient quantum sensors [77].

The magnetic HF interaction for atomic and molecular systems has been studied at different

levels of *ab-initio* theories ranging from density-functional theory (DFT) [78, 79, 80, 81], projected Hartree-Fock theory [82], coupled-cluster theory [78, 83], and multiconfigurational and multireference theories [84, 85, 86, 87, 88, 89], with or without relativistic treatment of the HF coupling Hamiltonian. One of the most popular methods for investigating the HF interaction is DFT using various exchange-correlation functionals such as local-density approximation (LDA) [17, 19, 20], BP86 generalized-gradient approximation (GGA), [90, 91], Perdew-Burke-Ernzerhof (PBE)-GGA [23], B3LYP hybrid functional [57**?**], and strongly constrained and appropriately normed (SCAN) semi-local approximation [92]. Although B3LYP and SCAN functionals have been shown to be superior in describing electronic and magnetic properties over LDA and GGA functionals for many systems including transition-metal (TM) elements [93, 94, 95, 96, 97, 98], this superiority does not necessarily hold for the HF coupling parameters [80, 81]. For example, Ref. [81] reported that the isotropic HF parameter for the TM center in ScO and TiF_3 calculated using the SCAN functional carries the opposite sign from the experimental data [99, 100]. Regarding the B3LYP functional, in most non-TM and TM systems, the calculated HF parameters are in good agreement with experimental data. However, for the ^{55}Mn center in MnO_3, Ref. [80] showed the B3LYP-calculated isotropic HF parameter has negative sign, while Ref. [81] obtained positive sign which is consistent with the experimental data [101] and the SCAN calculated result [81].

Recently, there has been a lot of progress in studies of electronic and magnetic properties of atomic and molecular systems based on DFT by including self-interaction correction (SIC) to the LDA or PBE-GGA exchange-correlation functional. Perdew and Zunger [28] proposed effective methods for the SIC to the exchange-correlation energy, which are not size-extensive. Recently, Pederson and his collaborators [31, 33, 37] suggested a size-extensive SIC scheme based on a set of localized Fermi orbitals. The proposed SIC approaches successfully explained binding energies of charge-negative systems [28] and the interaction between anionic

solute and solvent molecules [102], an increased gap between the highest occupied molecular orbital (HOMO) and the lowest unoccupied molecular orbital (LUMO) [1, 103], and enhanced spin polarization of TM sites for TM-based molecules that are comparable to the values computed from multiconfigurational methods [1], to name a few improvements. The spin polarization at the nuclear site is one of the major contributions to the isotropic HF interaction. Therefore, it would be interesting to investigate the HF interaction using one of the SIC methods and to see if SIC to the exchange-correlation energy provides HF coupling parameters which agree better with experimental data.

Here we calculate the HF coupling parameter for atomic systems and small non-TM and TM molecules by applying the Fermi-Löwdin orbital (FLO) based self-interaction corrected DFT [31, 33, 37], and compare the results with SIC-free PW92-LDA [20] and PBE-GGA calculations as well as experimental data. Scalar relativistic effects and spin-orbit coupling are *not* included in the FLO-SIC formalism [31, 33, 37]. For the atomic systems of light to intermediate elements ($Z \leq 25$) where relativistic effects are negligible, the FLO-SIC HF coupling parameter (i.e., Fermi contact term) agrees better with the experimental value. The same trend is found for the Ti-based and Mn-based molecules of interest. For the non-TM molecules, the accuracy of the FLO-SIC HF coupling parameter (i.e., Fermi contact term) is comparable to that of the LDA or GGA results.

3.2 Theory

3.2.1 Magnetic Hyperfine Interaction

Let us consider an electron with linear momentum $\hat{\mathbf{p}}$ and spin magnetic moment $\hat{\mathbf{m}}_s$ ($=-g_e\mu_B\hat{\mathbf{s}}$) moving in the presence of a point-like nucleus at the origin, where g_e, μ_B, and $\hat{\mathbf{s}}$ are the elec-

tron g-factor, Bohr magneton, and electron spin operator, respectively. (Here we ignore the electron's orbital magnetic moment since the atomic and molecular systems that we consider do not have significant orbital magnetic moments.) This electron experiences a magnetic field generated by the nucleus, $\nabla \times \hat{\mathbf{A}}_{\mathrm{N}}$, where $\hat{\mathbf{A}}_{\mathrm{N}}$ is a vector potential arising from the nuclear spin moment $\hat{\mathbf{m}}_N$ ($=g_n\mu_n\hat{\mathbf{I}}$), where g_n, μ_n, and $\hat{\mathbf{I}}$ are the nucleus g-factor, nuclear magneton, and nuclear spin operator, respectively. The microscopic non-relativistic Hamiltonian for such an electron [71] is written as

$$\hat{H} = \frac{1}{2m}\left(\hat{\mathbf{p}} + e\hat{\mathbf{A}}_{\mathrm{N}}\right)^2 - \hat{\mathbf{m}}_s \cdot \{\nabla \times \hat{\mathbf{A}}_{\mathrm{N}}\}, \tag{3.1}$$

where m is the electron mass. Keeping only the linear terms in the nuclear vector potential and dropping the electron kinetic energy, the above Hamiltonian can be mapped into the following effective HF interaction Hamiltonian:

$$\hat{H}_{\mathrm{HF}} = \hat{\mathbf{S}} \cdot \mathbf{A} \cdot \hat{\mathbf{I}}, \tag{3.2}$$

where $\hat{\mathbf{S}}$ is a total effective electron spin operator. The HF coupling tensor, $\mathbf{A}$, can be decomposed into two contributions [84, 87]:

$$\mathbf{A} = \mathbf{A}^{FC} + \mathbf{A}^{SD}. \tag{3.3}$$

The first term in Eq.(3.3), $\mathbf{A}^{FC}$, is referred to as the Fermi contact term which describes the contact interaction between the nuclear spin and the total electron spin at the nuclear site. For a point-like nucleus in the non-relativistic limit, the Fermi contact contribution to the

HF interaction Hamiltonian can be expressed as

$$\hat{H}_{\mathrm{FC}} = -\frac{8\pi}{3}\alpha^2 \hat{\mathbf{m}}_s \cdot \hat{\mathbf{m}}_N \delta(\mathbf{R_n}), \tag{3.4}$$

where $\delta(\mathbf{R_n})$ is the Dirac delta function and $\mathbf{R_n}$ is the nuclear position. Here α is the fine structure constant. The kl component of the Fermi contact contribution to the HF coupling tensor can be written as [104]

$$[\mathbf{A}^{FC}]_{kl} = \frac{4\pi}{3}\frac{g_n g_e \mu_n \mu_B}{\langle S_z \rangle} n_s(\mathbf{R_n})\delta_{kl}, \tag{3.5}$$

where k and l run through (x, y, z) and δ_{kl} represents the Kronecker delta function. The electron spin density $n_s(\mathbf{r})$ at the electron position vector $\mathbf{r}$, is simply computed from the difference between the spin-up and spin-down electron densities, $n_\uparrow(\mathbf{r}) - n_\downarrow(\mathbf{r})$ in DFT calculations. $\langle S_z \rangle$ is the expectation value of the z-component of the total electron spin operator. The Fermi contact contribution is isotropic. A singly-occupied valence-shell s-orbital obviously contributes to the Fermi contact contribution. In addition, core-shell occupied orbitals can contribute to the Fermi contact term since the valence orbital(s) can spin-polarize them, which is referred to as core spin polarization. Spin-up and spin-down occupied orbitals in different core shells have different degrees of radial contribution, which induces a non-zero spin density at the nuclear site.

The second term in Eq.(3.3), $\mathbf{A}^{SD}$, is referred to as spin-dipole term and it describes the dipole interaction between the non-relativistic electron spin and the point-like nuclear spin. The kl component of $\mathbf{A}^{SD}$ can be written as[104]:

$$[\mathbf{A}^{SD}]_{kl} = \frac{g_n g_e \mu_n \mu_B}{2\langle S_z \rangle} \int d\mathbf{r} \frac{3r_k r_l - r^2 \delta_{kl}}{r^5} n_s(\mathbf{r}), \tag{3.6}$$

where the integral runs over the spin density over all space. By definition, the $\mathbf{A}^{SD}$ tensor is traceless, and the symmetry of the system is reflected in the tensor. For example, for a molecule with C_n rotational symmetry ($n > 2$), taking the symmetry axis as the z axis, we know that $A_{xx}^{SD} = A_{yy}^{SD} = -A_{zz}^{SD}/2$ must be satisfied.

3.2.2 FLO-SIC Method

To compensate for self-interaction error (SIE) in approximate exchange-correlation functionals $E_{\rm xc}^{\rm app}[n_\uparrow, n_\downarrow]$, Perdew and Zunger [28] suggested the following SIC to the exchange-correlation energy:

$$E_{\rm xc}^{\rm SIC} = E_{\rm xc}^{\rm app}[n_\uparrow, n_\downarrow] - \sum_{i,\sigma}(U^{\rm s}[n_{i\sigma}] + E_{\rm xc}^{\rm app}[n_{i\sigma}, 0]), \tag{3.7}$$

$$n_\sigma(\boldsymbol{r}) = \sum_i |\phi_{i\sigma}(\boldsymbol{r})|^2 = \sum_\alpha |\psi_{\alpha\sigma}(\boldsymbol{r})|^2, \tag{3.8}$$

where $\phi_{i\sigma}(\boldsymbol{r})$ and $\psi_{\alpha\sigma}(\boldsymbol{r})$ are occupied localized orbitals and occupied canonical (Kohn-Sham) orbitals, respectively, and $n_{i\sigma}(\boldsymbol{r}) = |\phi_{i\sigma}(\boldsymbol{r})|^2$ ($\sigma = \uparrow, \downarrow$). For the exact, but unknown E_{xc}, the summation in Eq. (3.7) would vanish. However, for an approximate E_{xc}, this term should compensate for an incomplete cancellation. Note that the energy in Eq. (3.7) is not invariant under unitary transformations of the occupied orbitals. Therefore, the total energy should be minimized with respect to *both* electron density $n_\sigma(\boldsymbol{r})$ *and* and the specific set of $\phi_{\alpha\sigma}(\boldsymbol{r})$ used to evaluate the SIC term. Furthermore, in the formulation of Eq. (3.7), the total energy is not necessarily size-extensive[28].

In the FLO-SIC method [31, 33, 37], a set of localized Fermi orbitals is constructed from the

occupied Kohn-Sham orbitals as follows:

$$F_{i\sigma}(\boldsymbol{r}) = \frac{\sum_\alpha \psi_{\alpha\sigma}(\boldsymbol{a}_{i\sigma})\psi_{\alpha\sigma}(\boldsymbol{r})}{\sqrt{\sum_\alpha |\psi_{\alpha\sigma}(\boldsymbol{a}_{i\sigma})|^2}}, \tag{3.9}$$

where the index i goes from one to the number of occupied orbitals. These Fermi orbitals are defined in terms of three-dimensional spatial coordinates $\boldsymbol{a}_{i\sigma}$, called the Fermi orbitals descriptors (FODs). After subsequent orthogonalization using the Löwdin scheme [32], the resulting Fermi-Löwdin orbitals (FLOs) are both localized (ensuring size-consistency) and invariant under the unitary transformations of the underlying $\psi_{\alpha\sigma}$. These FLOs are then used to define the SIC correction of E_{xc} in Eq. 3.7. The FLO-SIC method has a formal computational advantage compared to the Perdew-Zunger SIC method [28], since the total energy optimization requires solving $3N$ equations for FODs coordinates, rather than $O(N^2)$ equations for occupied orbitals $\psi_{\alpha\sigma}$ with localization equation constraints [29]. The optimized FOD positions have been shown to generally follow the predicted chemical bonding pattern in molecules.

3.3 Computational Details

3.3.1 Hyperfine Coupling Tensor

All calculations are performed using the `FLOSIC` version 0.2 code[53], which is based on the UTEP version of the `NRLMOL` program[50, 51, 52, 105]. We use the default `NRLMOL` Gaussian-type basis sets [54]. To compute the HF coupling parameters, $\mathbf{A}^{FC}$ and $\mathbf{A}^{SD}$, we add several modifications the FLO-SIC source code. For the Fermi-contact term, an additional mesh point (with zero volume element) is added at the atom centers such that nuclear-centered spin densities can be calculated. For the spin-dipole term, the integral in Eq. (3.6) can be

readily calculated using the electron densities computed at each SCF step. The integration is represented in the code as a weighted sum over the mesh points. In the FLO-SIC program the mesh is varied or refined until the desired numerical accuracy for a set of test integrands is achieved [50].

3.3.2 Setup and Optimization Process

All molecular geometries are optimized with the PBE-GGA functional until the root mean square of the atomic forces dropped below 1 mHa/a_B (a_B is the Bohr radius). The optimized geometries for the molecules are provided in the Supplementary material. The SIC-free DFT calculations are performed for the optimized geometries using the PBE-GGA [23] and PW92-L(S)DA [20] functional, and then the HF coupling parameters are computed. The FLO-SIC correction is applied to the PW92-L(S)DA functional. The starting density and Kohn-Sham orbitals for these calculations are typically taken from a converged SIC-free PW92-L(S)DA or PBE-GGA result. Based on this density and a starting FOD set (see the next section), an initial set of FLOs, Eq. (3.9), is constructed, and the SIC-corrected energy, Eq. (3.7), is computed. This energy is then optimized self-consistently with respect to both electron density $n(\boldsymbol{r})$ and the FOD positions $\boldsymbol{a}_{i\sigma}$. We employ the "frozen-density loop" optimization method because it has been shown to be more efficient than the traditional optimization scheme (simultaneous optimization of FODs and density) for transition-metal based molecules [1]. For every update of $n(\boldsymbol{r})$, the FODs are first fully optimized with the density fixed, until the FOD force tolerance of 0.5 mHa/a_B is achieved. Self-consistent updates of $n(\boldsymbol{r})$ are performed until the total energy converges within the accuracy of 10^{-6} Ha and the Fermi contact term value converges within 1 MHz.

3.3.3 Starting FOD sets

An important step in setting up a FLO-SIC calculation is to generate the initial FOD set. For molecules with light elements, initial FOD configurations can be generated based on expected molecular bonding patterns. For molecules with moderately heavy elements including TM elements, the SIC energy may have multiple local minima with respect to FOD positions and so several initial FOD configurations may need to be tried in order to find a global minimum upon optimization. Based on these considerations, we adopt the following methods of starting FOD generation for different systems.

Single Atoms and Ions

The pre-converged FOD results for neutral single atoms have been already published by Kao et al.[34] For all atoms and ions except Cu, we use these results as starting points for re-optimization, to ensure to satisfy our own convergence criteria. In all cases, the re-optimization converges within 10 frozen-density loops. The single-atom FODs are grouped roughly into concentric spherical shells based on the electron principal quantum numbers. For example, in the Mn neutral atom with configuration $[Ar]3d^5 4s^2$, we have one spin-up and one spin-down FODs placed nearly at the center of the atom (for the $1s^2$ electrons), four spin-up and four spin-down FODs at an average of 0.24 a_B from the center (for $2s^2 2p^6$), nine spin-up and four spin-down at an average of 0.91 a_B (for $3s^2 3p^6 3d^5$), and one spin-up and one spin-down at about 6 and 4 a_B, respectively (for $4s^2$). Regarding the starting FOD geometry for the cation Mn^+, we simply remove the $4s$ spin-down FOD from the Mn published FOD set, as described above.

In the case of the Cu atom, we found an alternative FOD set that results in a lower final FLO-SIC energy (by about 4 mHa) than the original FOD geometry found by Kao et al.

[34]. As in the original geometry, the FODs in the new set group into concentric spherical shells by electron principal quantum numbers. The main difference is that the FODs within these shells are positioned such that the new configuration has C_S symmetry, which was not present in the original set. These FODs were optimized with the same convergence criteria as used for other atoms. We report the results obtained from the new Cu FODs in this work. For other atoms and ions, we did not find any symmetrized starting FOD arrangements that improved the final energy after optimization. For the exact final FOD geometries of all studied systems, see the Supplementary material.

Molecules without Transition Metal Atoms (CH_3, SiH_3, HCO, $(H_2CO)^+$, HSiO, NF_2)

For light-element molecules sufficiently good initial FODs can be generated by using the Monte-Carlo based fodMC program[44], and they rapidly converge to the minimum of the SIC energy. First, a Lewis structure is drawn for each molecule, assuming that the unpaired electron is located at one of the atomic centers, i.e., the symmetry center of the molecule. Then, the fodMC code automatically creates the starting FOD set based on the prescribed bonding picture: one FOD pair (spin-up and spin-down) is assigned for each single bond and lone pair, and two FOD pairs are for double bonds etc. Core FODs are placed on concentric shells, similarly to the results of single-atom calculations. One exception is HSiO. In this case, better starting FODs are obtained from the natural bond orbital (NBO) analysis [106] (see the next section for details). The FLO-SIC calculations for all these molecules converge within 10 or fewer frozen-density loops.

Transition-metal Based Systems (TiF_3, MnF, MnF_2, MnO, MnO_2, MnO_3 $[Mn(H_2O)_6]^{2+}$):

For molecules with TM elements the procedure of creating the starting FOD sets is similar to that outlined for non-TM-based molecules in the previous section. However, there are some important nuances and complications. For example, the utility of the fodMC code is not guaranteed for TM-based systems because (i) final FOD positions from the fodMC code do not necessarily follow the symmetries of the molecules and (ii) there is a large number of valence electrons at the $3d$ sites. In the former case the valence FODs are placed by hand at concentric shells around their corresponding centers following the symmetry of the molecule as closely as possible. Furthermore, as mentioned before, several initial FOD guesses may be needed to ensure the global minimum upon optimization. For TM-based molecules the optimal bonding picture is not always straightforward, and optimized FODs are not always associated with Lewis structures.

To assist the search for alternative FOD configurations, we employ the NBO analysis implemented in the `NBO` version 7.0 code[106]. Natural bond orbitals are defined as a localized and orthonormal set of maximum-occupancy molecular orbitals that describes an optimal Lewis-like structure. These orbitals are derived from the one-particle reduced density matrix and so they are uniquely associated with the given electron density $n(\mathbf{r})$ of a molecule. This input density can be obtained from a preliminary SIC-free DFT calculation by using a subroutine of the `FLOSIC` code which generates a native `NBO` input file. However, for molecules with strong multiconfigurational character (such as MnO_3), the input density is generated from a preliminary complete active space self-consistent field (CASSCF) calculation using the `MOLCAS` version 8.2 code [65]. The details of the CASSCF calculation for MnO_3 are discussed in Appendix 3.9.2. The `MOLCAS` output is converted to an `NBO` input file using the `Molden2AIM` utility program [107]. Once the optimal Lewis-like structure is generated, it is used to initialize FODs for the FLO-SIC calculation. For open-shell systems the above NBO-

based procedure is done separately for spin-up and spin-down electron densities. Therefore, the bond order on the two spin channels can be different from each other for a given atomic pair in some cases. On the other hand, that is not the case for the Lewis-structure-based FODs. This is one of the main reasons that NBO-based FODs would differ from Lewis-structure-based FODs. (Note that the starting density for the FLO-SIC computation still comes from an SIC-free DFT calculation, regardless of the density used for the NBO analysis.) If the molecular electronic structure cannot be described sufficiently well with a single bonding picture, we fit it with a weighted linear combination of idealized Lewis-like configurations, by using a modified version of the NBO method referred to as natural resonance theory (NRT) [108, 109, 110] implemented in the `NBO` version 7.0 code. In our application of NRT to the molecules, structures with more dominant weights are chosen as a basis for the single initial FOD set. (Our current methodology allows only one bonding picture to be chosen as a starting FOD set in each case.) If none of the aforementioned methods (Lewis structure, NBO, NRT) can provide a desirable bonding picture (i.e., reflecting the molecular symmetry in the FLO-SIC density), or if several core-FOD arrangements are equally probable based on the aforementioned criteria, then direct trial-and-error FOD placements are also attempted to achieve a satisfactory initial FOD structure. In general, when several structures are considered for a given molecule, we select the lowest-energy structure upon optimization for further calculations of the HF interaction as long as it preserves the symmetry of the electron density and molecule to a great extent. To examine the symmetry of the electron density, we compute the Mulliken spin population of each atom and the Fermi-contact term of the corresponding atom. Schematic starting FOD configurations for TM-based molecules that we consider are shown in Appendix 3.9.1.

3.3.4 Basis Set Contraction and Size Effects

For an accurate DFT calculation of the HF interaction with and without SIC, it is important to be able to describe the electron spin density very near the nuclear site since the Fermi contact contribution arises from the spin density at the nuclear site. It was shown than uncontracted augmented basis sets are more suitable than contracted basis sets for the calculation of the HF coupling tensor due to their flexibility to accommodate the electron density and spin density in close proximity to the nuclear site [111]. We perform the following basis set tests after computation of the densities and Fermi contact terms using the standard `NRLMOL` contracted Gaussian basis sets:

1. Uncontract the `NRLMOL` default Gaussian basis sets; re-calculate the density, energy, and Fermi contact term with the uncontracted basis sets for each system;

2. Augment the uncontracted basis sets with more narrow Gaussian functions (five total); re-calculate the density, energy, and Fermi contact term with the augmented basis sets for each system.

The first step can be done with a simple modification of the basis-set files for each system (which results in a larger number of total functions since each Gaussian is a separate basis function now). For the second step, we need to generate five additional narrow-Gaussian exponents for each element in every system. After reviewing the other basis sets, we decide to add new exponent values in an even-tempered way: each newly-added exponent is proportional to the previous one, up-scaled by the same constant. The value of this constant for each element is determined as the ratio between the two highest ones from the original (default) basis set. Since each new exponent has larger magnitude than the previous one, it describes a more narrow Gaussian function. The exact values of the added exponent are shown in Appendix 3.9.3. The largest value for each element ranges from $\sim 10^6$ for the H

atom to $\sim 10^{11}$ for the Cu atom. As we uncontract and augment the original basis set, we re-evaluate the electron density, energy, and Fermi contact term. For this calculation, we use the converged FODs from the default-basis FLO-SIC calculations as the starting point for the new uncontracted augmented basis ones, assuming that the optimal FODs are not affected noticeably by the utilization of the new basis sets.

The results for modified basis sets are shown in Section 3.7 and Appendix 3.9.3. In general, the effect of adding narrower Gaussian basis functions on the hyperfine parameters is much smaller than the effect of uncontracting the default basis set. This suggests that the standard `NRLMOL` basis set already contains sufficiently large Gaussian exponents to adequately describe the electron density at the nuclear positions for the systems of our study.

3.4 Optimized FODs of molecules

3.4.1 Molecules without transition-metal elements

The optimized FOD positions in CH_3, SiH_3, and NF_2 molecules are consistent with Lewis bonding pictures: there are single bonds to the H and F atoms, and unpaired electrons are located at the centers of symmetry (C, Si, and N). In $(H_2CO)^+$ the FOD positions also reflect the Lewis structure (single C-H bonds and a double C-O bond) with an unpaired electron residing on the O atom, as confirmed by the Mulliken spin populations from DFT calculations. The bonding pictures from the NBO analysis for CH_3, SiH_3, NF_2, and $(H_2CO)^+$ coincide with Lewis structure predictions.

Less trivial cases are found in HCO and HSiO molecules. Figure 3.1 shows bonding structures, initial and converged FLO-SIC energies, and starting FOD structures for HCO and HSiO molecules calculated from the Lewis theory and the NBO analysis. In our prediction

a)

HCO		Lewis Theory	NBO Prediction
# of spin-*up* FODs		8	8
# of spin-*down* FODs		7	7
Starting Valence FODs		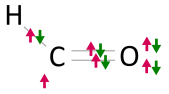	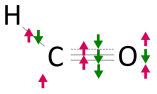
Formal Charges		**C:** 0 **O:** 0 **H:** 0	**C:** -0.5 **O:** 0.5 **H:** 0
PBE-NBO Non-Lewis Occupation	**UP:**	0.06 (0.8% of 8)	0.06 (0.8% of 8)
	DN:	**0.29 (4.2% of 7)**	**0.01 (0.2% of 7)**
Initial FLO-SIC Energy (Ha)		-114.183123	-114.187023
Initial **C** Fermi Contact term (MHz)		440.8	362.3
Converged FLO-SIC Energy (Ha)		**-114.207690**	**-114.207996**
Final **C** Fermi Contact term (MHz)		**458.6**	**461.7**

b)

HSiO		Lewis Theory	NBO Prediction
# of spin-*up* FODs		12	12
# of spin-*down* FODs		11	11
Starting Valence FODs			
Formal Charges		**Si:** 0 **O:** 0 **H:** 0	**Si:** -0.5 **O:** 0.5 **H:** 0
PBE-NBO Non-Lewis Occupation	**UP:**	0.06 (0.5% of 12)	0.06 (0.5% of 12)
	DN:	**0.20 (1.8% of 11)**	**0.06 (0.5% of 11)**
Initial FLO-SIC Energy (Ha)		-366.102103	-366.100620
Initial **Si** Fermi Contact term (MHz)		-669.1	-523.7
Converged FLO-SIC Energy (Ha)		**-366.134111**	**-366.136964**
Final **Si** Fermi Contact term (MHz)		**-734.3**	**-565.8**

Figure 3.1: Bonding pictures, initial and converged FLO-SIC energies, and starting FOD structures derived from the Lewis theory and NBO analysis for (a) HCO and (b) HSiO. Smaller total non-Lewis orbital occupation (derived from fitting the given bonding picture to the PBE-GGA density using the `NBO` program) indicates a better Lewis-like configuration. A lower final converged FLO-SIC energy corresponds to a better starting FOD position. The Fermi contact terms are for ^{13}C and ^{29}Si.

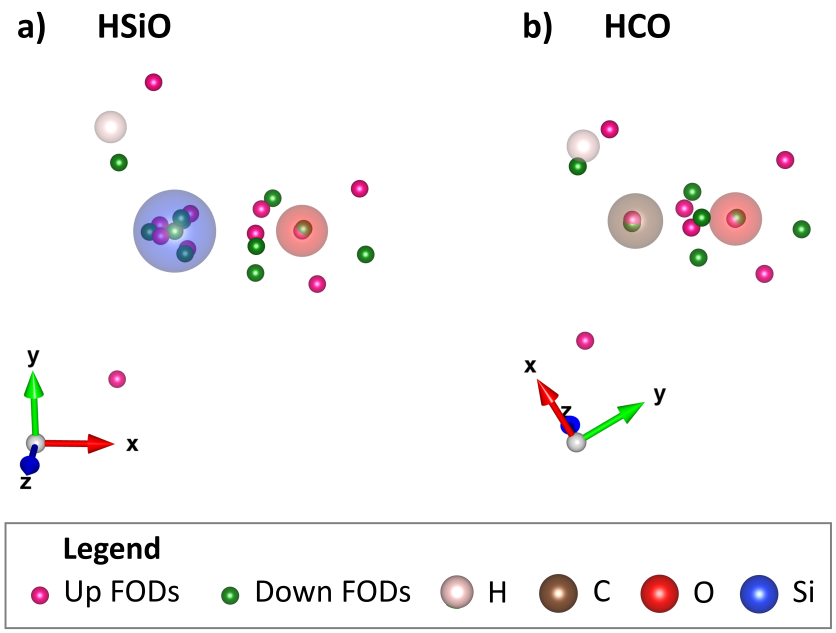

Figure 3.2: Optimized spin-up and spin-down FODs for HCO and HSiO molecules based on the NBO analysis.

of Lewis structure for HXO (X = C or Si), there is a double bond between X and O, a single bond between X and H, and an unpaired electron located on X for both the spin-up and spin-down channels. However, the NBO analysis predicts quite different orders for the spin-down channel such as a triple X-O bond and an unpaired electron at O, although orders for the spin-up channel are the same as those from the Lewis theory. After optimization, the Lewis FODs are closer to the NBO picture. Figure 3.2 shows our optimized FODs for HCO and HSiO. The optimized FOD positions are provided in the Supplementary material. Our optimized FODs for HCO reproduce the findings of previous work by Schwalbe *et al.* [55], where the bonding picture was derived from the Linnett double-quartet theory [112, 113, 114].

3.4.2 Transition-metal molecules

As mentioned earlier, the generation of FODs on TM-based molecules can be challenging compared to that on non-TM molecules. Several initial FOD guesses may be needed to reach the global energy minimum, and the bonding picture corresponding to the best FOD configuration may not be obvious. In order to generate starting FOD configurations, we employ the Lewis theory, the NBO analysis, the NRT analysis, MOLCAS calculations (for MnO_3), and a trial-and-error method. The final FOD positions upon optimization can differ significantly from the initial FOD positions. The best FOD configuration is identified based on *both* the final converged FLO-SIC energy *and* the symmetry of the FOD configuration. Figure 3.3 illustrates the optimized spin-up and spin-down FOD positions for the TM-based molecules that we consider. After many tests, the best optimized FODs giving rise to the lowest FLO-SIC energy with molecular symmetry for MnF, MnO_2, and MnO_3 are found from the NBO analysis using either the PBE-GGA density or the `MOLCAS` density, while the best optimized FODs for MnO and $Mn(H_2O)_6^{2+}$ are found from the Lewis theory. In the case of MnF_2 the NRT analysis gives rise to the best optimized FODs, and for TiF_3 the trial-and-error method produces the ideal optimized FODs. The details of the FOD optimization procedure for specific molecules are outlined in Appendix 3.9.1.

3.5 Electronic and magnetic properties

While the converged FOD positions may allow one to deduce a corresponding bonding picture of the molecule, as in HCO and HSiO, this is not always the case for TM-based systems. A better way to analyze the results is, therefore, to analyze the electronic properties of the FLO-SIC and SIC-free DFT densities. We compute Mulliken spin populations of the considered molecules.

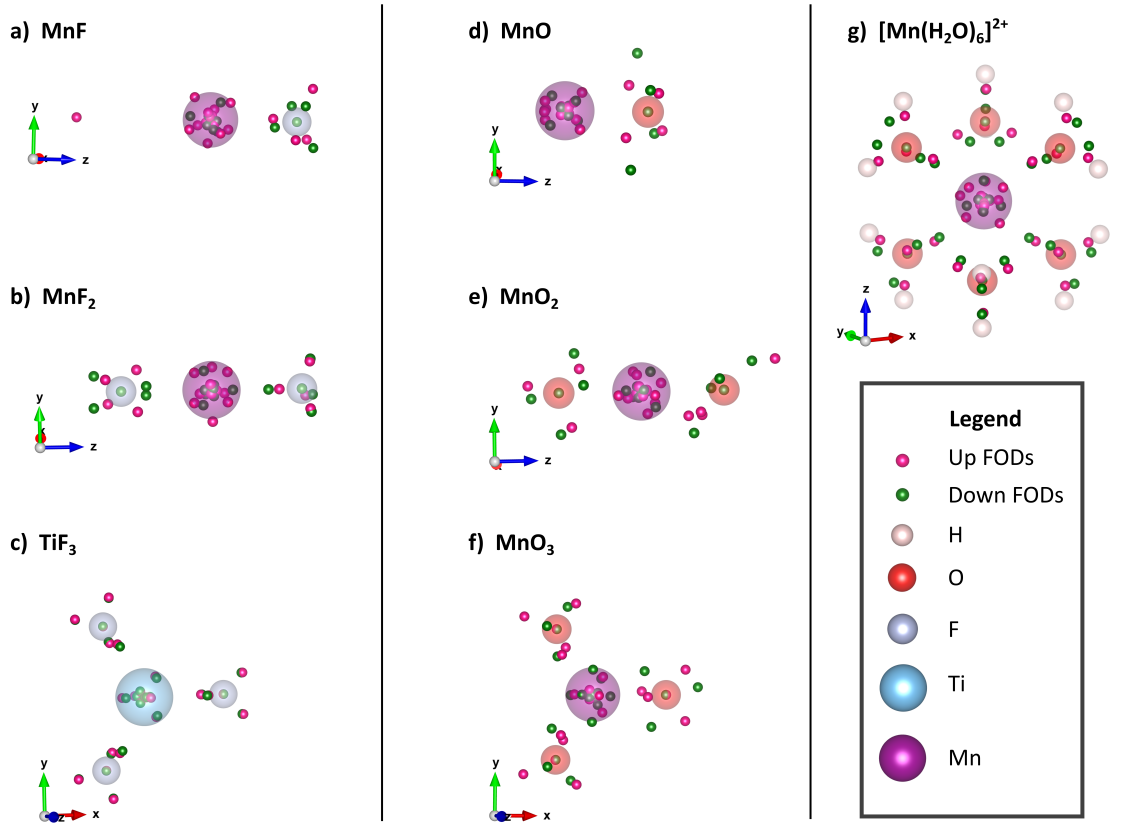

Figure 3.3: Optimized spin-up and spin-down FODs for the TM molecules.

Table 3.1: Mulliken spin moments (in units of μ_B) of all atoms in the non-TM molecules (with electron spin $S = 1/2$) based on FLOSIC-LDA, PW92-LDA, and PBE-GGA calculations. The molecular geometries are given in the Supplementary material.

Molecule	Atom	**FLOSIC-LDA**	LDA	PBE-GGA
CH_3	C	1.237	1.231	1.376
	H(1)	-0.079	-0.077	-0.125
	H(2)	-0.079	-0.077	-0.125
	H(3)	-0.079	-0.077	-0.125
HCO	O	0.223	0.241	0.232
	C	0.644	0.605	0.590
	H	0.133	0.154	0.178
$(H_2CO)^+$	O	0.876	0.712	0.757
	C	-0.088	-0.007	-0.060
	H(1)	0.106	0.147	0.151
	H(2)	0.106	0.147	0.151
HSiO	Si	0.484	0.561	0.546
	O	0.308	0.218	0.224
	H	0.207	0.222	0.230
SiH_3	Si	1.029	1.032	1.094
	H(1)	-0.010	-0.011	-0.031
	H(2)	-0.010	-0.011	-0.031
	H(3)	-0.010	-0.011	-0.031
NF_2	N	0.955	0.836	0.869
	F(1)	0.022	0.082	0.066
	F(2)	0.023	0.082	0.066

Table 3.1 shows the Mulliken spin moments of the atoms in the non-TM systems calculated using the FLO-SIC, PW92-LDA, and PBE-GGA methods. In all the cases, the FLO-SIC spin moments and associated symmetries are fairly similar to the LDA and PBE-GGA results. For CH_3, HCO, and SiH_3, the spin moments between the FLO-SIC and SIC-free LDA differ by less than $0.05\mu_B$. For NF_2 about 0.12 μ_B is shifted from the fluorine atoms to the nitrogen atom with the inclusion of SIC into the LDA. For HSiO the silicon and hydrogen atoms lose $0.08\mu_B$ and $0.014\mu_B$ to the oxygen. For $(H_2CO)^+$ the carbon and two hydrogen atoms lose about $0.08\mu_B$ and $0.04\mu_B$ each to the oxygen atom, respectively.

Table 3.2 shows the Mulliken spin moments of the atoms in the TM-based molecules calculated using the FLO-SIC, PW92-LDA, and PBE-GGA methods. The largest discrepancy between the FLO-SIC result and the SIC-free DFT results is found for MnO_3 which has threefold rotational symmetry. Interestingly, the FLO-SIC spin density distribution reveals that the polarity of the three Mn-O bonds is reversed compared to the SIC-free DFT result. In the former the three oxygen atoms individually carry spin moments of 52-65% of that of the Mn atom and so the majority spin contributions come from the oxygen atoms, while in the latter the three oxygen atoms carry negligible spin densities of the order of $0.01\mu_B$ and so the majority spin contribution arises from the Mn atom. Furthermore, the FLO-SIC spin density distribution has small symmetry breaking in the oxygen atoms, while that is not the case for the SIC-free DFT result. Another large discrepancy occurs for MnO_2. With FLO-SIC, the Mn atom (or each of the two oxygen atoms) picks up $\sim 0.8\mu_B$ (or $\sim 0.4\mu_B$) more spin moment than the SIC-free DFT calculation. Here we also observe slight symmetry breaking in the FLO-SIC spin moment distribution. For MnF and MnF_2, the inclusion of the SIC decreases the magnitude of the spin moment localized on fluorine atoms (and increases it, therefore, for the TM atom). This trend is more pronounced in MnF, where the fluorine atom loses $0.1\mu_B$ to the Mn atom. The FLO-SIC results for TiF_3, MnO, and $(Mn(H_2O)_6)^{2+}$

are very similar to the SIC-free DFT results.

Table 3.2: Mulliken spin moments (in units of μ_B) of all atoms in the TM-based molecules based on FLOSIC-LDA, LDA, and PBE-GGA calculations. The molecular geometries are given in the Supplementary material.

Molecule	Atom	**FLOSIC-LDA**	LDA	PBE-GGA
TiF_3	Ti	1.005	1.060	1.060
	F(1)	-0.002	-0.020	-0.020
	F(2)	-0.002	-0.020	-0.02
	F(3)	-0.002	-0.020	-0.02
MnF	Mn	5.947	5.843	5.854
	F	0.053	0.157	0.146
MnF_2	Mn	4.918	4.768	4.785
	F(1)	0.032	0.116	0.107
	F(2)	0.050	0.116	0.107
MnO	Mn	4.631	4.606	4.636
	O	0.369	0.394	0.364
MnO_2	Mn	4.387	3.404	3.448
	O(1)	-0.592	-0.202	-0.224
	O(2)	-0.795	-0.202	-0.224
MnO_3	Mn	-1.380	1.064	1.103
	O(1)	0.891	-0.021	-0.034
	O(2)	0.767	-0.021	-0.034
	O(3)	0.721	-0.021	-0.034
$(Mn(H_2O)_6)^{2+}$	Mn	4.898	4.818	4.883
	all O	0.085	0.140	0.105
	all H	0.017	0.042	0.012

3.6 Hyperfine Coupling Tensor

We calculate the Fermi contact $\mathbf{A}^{FC}$ and spin-dipole $\mathbf{A}^{SD}$ contributions to the HF coupling tensor for ten atoms, six light-element molecules, and seven TM-based molecules, using the FLO-SIC and the SIC-free LDA and GGA. Since the Fermi contact contribution is isotropic, we report only one parameter. The spin-dipole contribution vanishes for atomic systems. For the spin-dipole contribution, we align the molecular symmetry axis with the z axis if

applicable. In order to compare our SIC and SIC-free DFT results with the experimental data, we make histograms and compute mean absolute errors and mean absolute percentage errors. Only the difference between the calculated and experimental values enters in the error for each molecule.

3.6.1 Fermi contact contribution for atoms

Tables 3.3 and 3.4, and Fig. 3.4 show the Fermi contact contribution calculated using the FLO-SIC LDA and the SIC-free PW92-LDA and PBE-GGA for the ten atomic systems in comparison to the experimental data. One naive expectation would be that the Fermi contact contribution must be zero for atoms with doubly-occupied s-shell orbitals such as the case of the neutral Mn atom ($[\mathrm{Ar}](3d)^5(4s)^2$). However, the FLO-SIC-LDA value for the ^{55}Mn center in Mn^0 is -94.3 MHz and the SIC-free LDA and GGA values are -127.2 and -144.5 MHz, respectively. Furthermore, the experimental value is -78.1 MHz [120]. Another naive expectation would be that the FLO-SIC-LDA A^{FC} value must be always greater than the LDA value in magnitude since SIC makes the electron density (thus, spin density) more localized than the SIC-free case. For the ^{1}H center in H ($1s^1$), the ^{7}Li center in Li ($[\mathrm{He}](2s)^1$), and the ^{55}Mn center in Mn^+ ($[\mathrm{Ar}](3d)^5(4s)^1$), the FLO-SIC-LDA value is indeed greater than the LDA value. For the rest of the atomic systems, however, the SIC-free LDA value is greater than the FLO-SIC-LDA value in magnitude, in contrast to the naive expectation.

The deviation from the two naive expectations can be understood by spin polarization of paired core and valence shells by the unpaired outermost shell which is referred to as core spin polarization [122, 123]. The core spin polarization lowers the total energy by decreasing the electron-nuclear interaction or making the electron-nuclear interaction more attractive [79]. For example, the unpaired outermost $3d$-shell orbitals in Mn atom spin-polarize the

Table 3.3: Calculated Fermi contact contribution A^{FC} to the HF interaction for atoms (in units of MHz) compared to experimental data. Here S and I are electronic and nuclear spins, respectively. In the case of Cr only the magnitude was reported in the experimental data [115].

Atom/Ion	Center	g_n	Method	A^{FC}
H	^{1}H	5.5857	**FLOSIC-LDA**	**1330.4**
$S = 1/2$	$I = 1/2$		LDA	1267.5
$(1s)^1$			PBE-GGA	1377.4
			Exp. ref. 116	1420.4
Li	^{7}Li	2.1709	**FLOSIC-LDA**	**423.6**
$S = 1/2$	$I = 3/2$		LDA	392.2
$[\mathrm{He}](2s)^1$			PBE-GGA	380.6
			Exp. Ref. 117	401.8
Na	^{23}Na	1.4783	**FLOSIC-LDA**	**870.2**
$S = 1/2$	$I = 3/2$		LDA	929.5
$[\mathrm{Ne}](3s)^1$			PBE-GGA	840.2
			Exp. Ref. 117	885.8
Mg^+	$^{25}Mg^+$	-0.3422	**FLOSIC-LDA**	**-556.9**
$S = 1/2$	$I = 5/2$		LDA	-589.1
$[\mathrm{Ne}](3s)^1$			PBE-GGA	-548.7
			Exp. Ref. 118	-596.0
K	^{39}K	0.2610	**FLOSIC-LDA**	**231.6**
$S = 1/2$	$I = 3/2$		LDA	240.0
$[\mathrm{Ar}](4s)^1$			PBE-GGA	211.9
			Exp. Ref. 117	230.9
Ca^+	$^{43}Ca^+$	-0.3764	**FLOSIC-LDA**	**-772.1**
$S = 1/2$	$I = 7/2$		LDA	-816.8
$[\mathrm{Ar}](4s)^1$			PBE-GGA	-766.8
			Exp. Ref. 119	-806
Cr	^{53}Cr	-0.3164	**FLOSIC-LDA**	**-84.8**
$S = 3$	$I = 3/2$		LDA	-85.5
$[\mathrm{Ar}](3d)^5(4s)^1$			PBE-GGA	-76.5
			Exp. Ref. 115	94.6
Mn^+	^{55}Mn	1.3813	**FLOSIC-LDA**	**756.4**
$S = 3$	$I = 5/2$		LDA	737.5
$[\mathrm{Ar}](3d)^5(4s)^1$			PBE-GGA	687.9
			Exp. Ref. 101	770.0
Mn	^{55}Mn	1.3813	**FLOSIC-LDA**	**-94.3**
$S = 5/2$	$I = 5/2$		LDA	-127.2
$[\mathrm{Ar}](3d)^5(4s)^2$			PBE-GGA	-144.5
			Exp. Ref. 120	-78.1
Cu	^{63}Cu	1.4822	**FLOSIC-LDA**	**5236.9**
$S = 1/2$	$I = 3/2$		LDA	5935.1
$[\mathrm{Ar}](3d)^{10}(4s)^1$			PBE-GGA	5713.9
			Exp. Ref. 121	5867.0

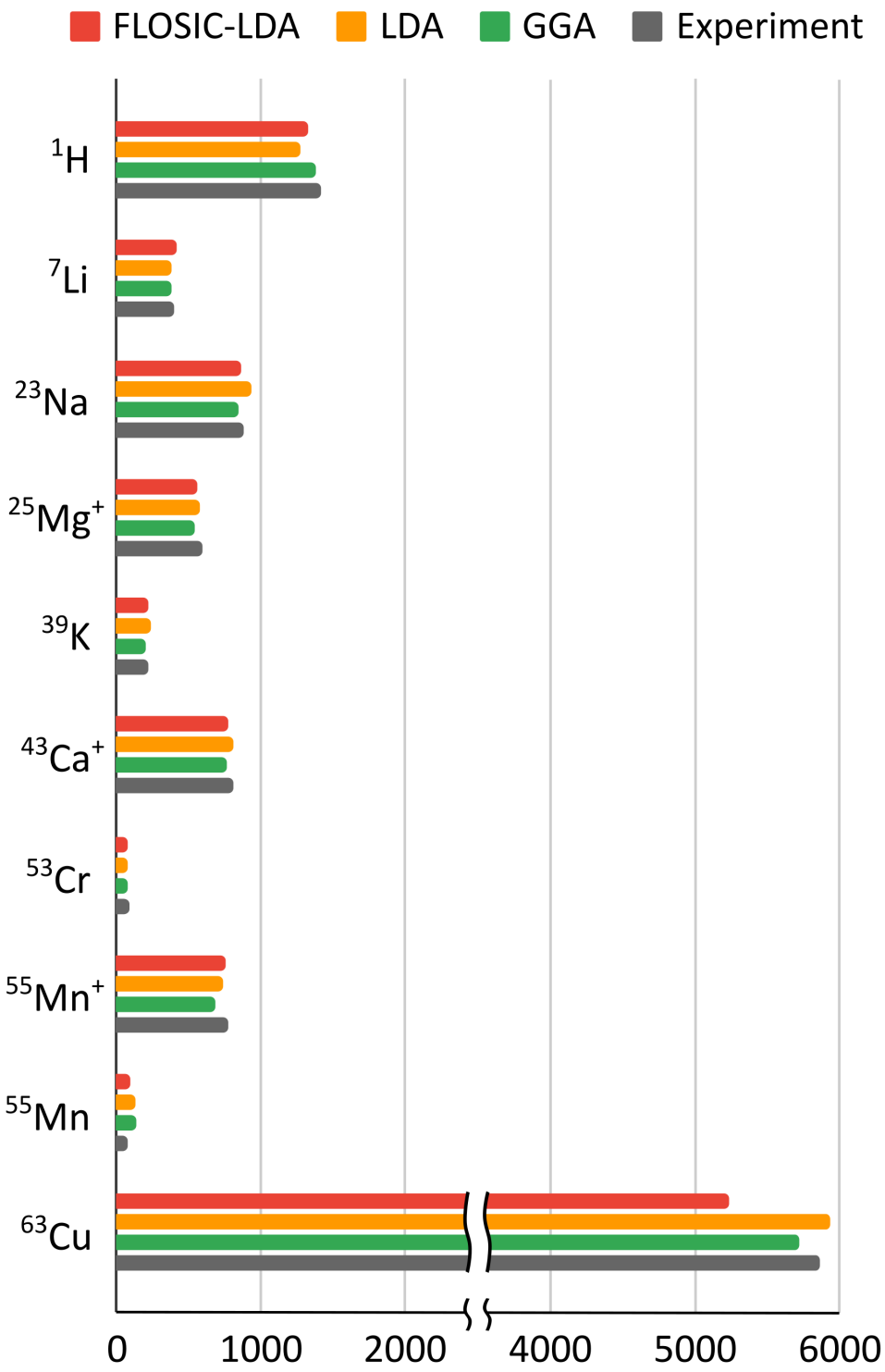

Figure 3.4: The absolute values of the Fermi Contact terms (in MHz) for the ten considered atoms in Table 3.3

Table 3.4: Mean absolute errors and mean absolute percentage errors for the considered atoms in Table 3.4, both including and excluding Cu.

Mean Absolute Error	**FLOSIC-LDA**	**87.1**
	LDA	39.2
	PBE-GGA	53.5
aMean absolute % Error	**FLOSIC-LDA**	**6.8%**
	LDA	10.2%
	PBE-GGA	15.2%
Mean Absolute Error (*without Cu*)	**FLOSIC-LDA**	**26.8**
	LDA	36.0
	PBE-GGA	42.4
Mean absolute % Error (*without Cu*)	**FLOSIC-LDA**	**6.4%**
	LDA	11.2%
	PBE-GGA	16.6%

doubly occupied core and valence shells, $1s$, $2s$, $2p$, $3s$, $3p$, and $4s$ shells [79]. This effect on the Fermi contact contribution to HF interaction is discussed in detail in the next subsection.

Overall, the FLO-SIC results are close to the LDA results within several tens of MHz, and they agree with the experimental data within a few and a few tens of MHz (a few hundred MHz for ^{63}Cu center in Cu). Comparing the FLO-SIC values to the experimental data for all considered atoms, we find that the mean absolute percentage error of the FLO-SIC values is 6.8% which is much smaller than those of the LDA and GGA results. .

3.6.2 Core spin polarization in atoms

To investigate the effect of core spin polarization for the considered atoms, we compute electron and spin densities projected onto different s orbitals as a function of radial distance r from the atomic center. Figure 3.5 shows electron density multiplied by r^2 and spin density (from only s orbitals) versus radial distance for the ^{55}Mn center in the neutral Mn atom calculated using the FLO-SIC-LDA and SIC-free LDA. As expected, the electron density

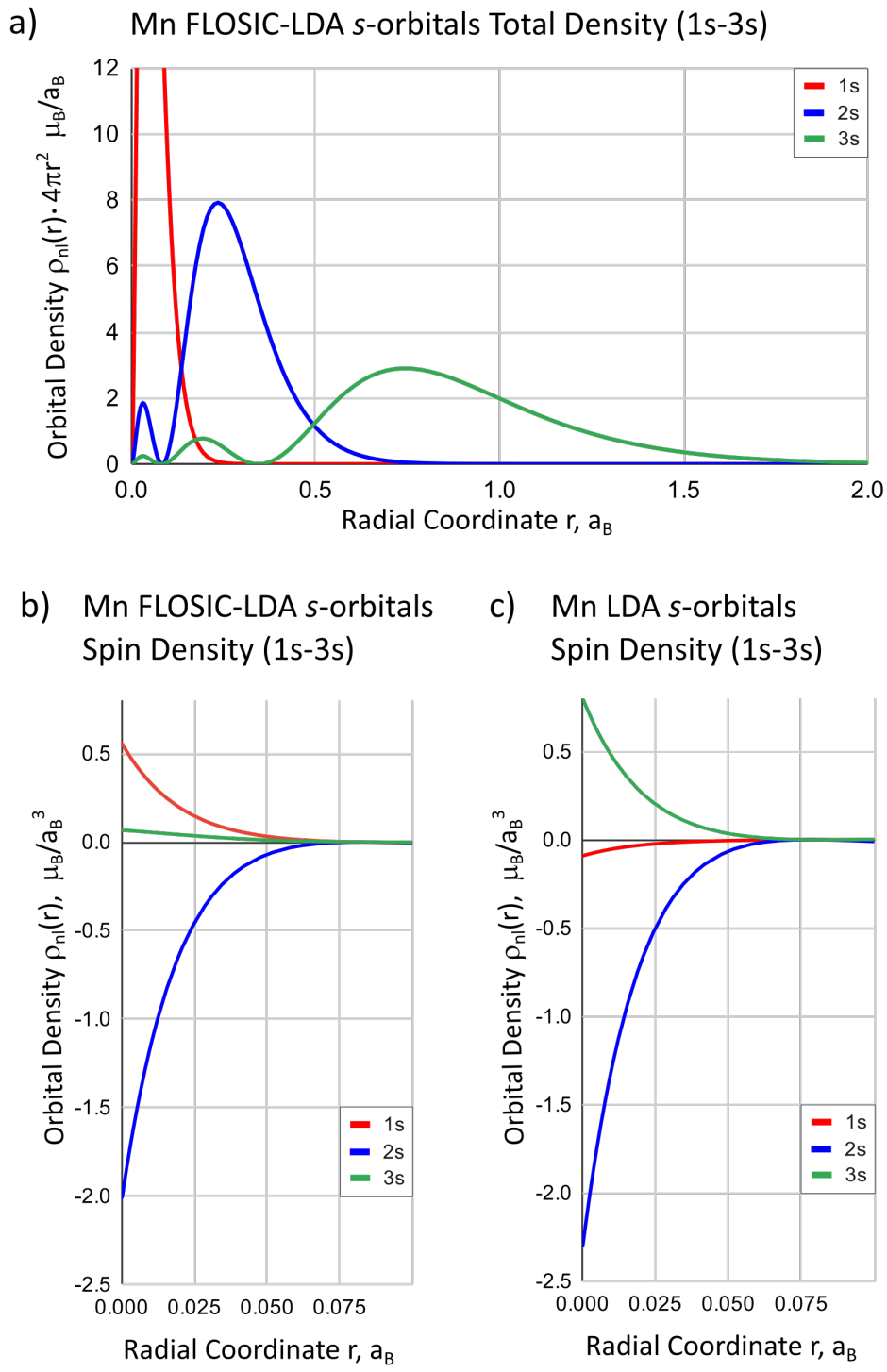

Figure 3.5: (a) FLO-SIC-LDA radial distribution of the charge densities projected onto s-orbitals near the Mn atom ($\tilde{\rho}_\sigma(r)\cdot 4\pi r^2$, where $\tilde{\rho}_\sigma(r)$ is the average electron charge density at radius r), (b) FLO-SIC-LDA and (c) LDA radial distribution of the projected spin density $\tilde{\rho}_\uparrow - \tilde{\rho}_\downarrow$ for the Mn atom.

Table 3.5: Individual s-orbital contributions to the spin density (in μ_B/a_B^3) at the ^{55}Mn center for Mn and Mn^+. Here "Total" denotes the sum of all s-orbital contributions. and "Exp" denotes experimental value.

Atom	Orbital	FLO-SIC-LDA (this work)	LDA (this work)	PBE-GGA (this work)	BP86 Ref. 79	UHF Ref. 79	Exp. Ref. 120
Mn	Total	-0.43	-0.58	-0.65	-0.07	-0.36	-0.35
$[Ar](3d)^5(4s)^2$	$1s$	0.56	-0.09	-0.05	-0.01	-0.04	
	$2s$	-2.01	-2.30	-2.41	-1.78	-2.71	
	$3s$	0.07	0.80	0.76	0.78	1.31	
	$4s$	0.96	1.02	1.05	0.93	1.08	
Mn^+	Total	4.10	4.00	3.73	4.31	-	4.12
$[Ar](3d)^5(4s)^1$	$1s$	0.83	-0.08	-0.03	0.04		
	$2s$	-2.04	-2.32	-2.43	-1.79		
	$3s$	0.30	0.78	0.70	0.76		
	$4s$	5.01	5.63	5.49	5.30		

for the $3s$ shell is more spread out than that for the $1s$ and $2s$ shells. Table 3.5 lists the calculated total s-orbital spin density as well as the individual s-orbital contributions at the ^{55}Mn center in the neutral Mn atom.

We first discuss the FLO-SIC-LDA result for the ^{55}Mn center in the neutral Mn atom. The FLO-SIC-LDA calculation shows that the $1s$ orbitals are positively spin-polarized to have $0.56\mu_B/a_B^3$ at the nuclear site, the $2s$ orbitals are *negatively* spin-polarized to have -2.01μ_B/a_B^3, and the $3s$ and $4s$ orbitals are positively spin-polarized to have 0.07 and $0.96\mu_B/a_B^3$ at the nuclear spite, respectively. The $2s$-orbital ($3s$-orbital) spin polarization is the largest (smallest) among that of the four s shells.The $2s$-orbital spin polarization has the opposite sign to that of the $3s$ orbitals due to orthogonality between the $2s$ and $3s$ orbitals [79]. The core spin polarization also gives rise to contraction and expansion of spin-up and spin-down orbitals. The spin-up $1s$ orbital is somewhat contracted toward the nuclear site, while the spin-down $1s$ orbital is a bit expanded. As a result, the net spin polarization of the $1s$ orbitals is positive at the nuclear site. The spin-up $2s$ orbital is quite expanded, while the spin-down $2s$ orbital is somewhat contracted. Consequently, the spin polarization of the $2s$ orbitals is

negative. The same logic is applied to the other orbitals. The sum of the spin density arising from all s orbitals is -0.45μ_B/a_B^3 at the nuclear site, which is close to the experimental value [79]. This leads to the Fermi contact contribution close to the experimental data.

Now we discuss the LDA result. This result is similar to the FLO-SIC-LDA case. The differences are that the 1s-orbital spin polarization has the same sign as that of the 2s-orbital spin polarization and that the 3s-orbital spin polarization is at least one order of magnitude larger than the 1s-orbital spin polarization in magnitude. The total s-orbital spin polarization is somewhat larger than the FLO-SIC-LDA and the experimental value in magnitude. The LDA result is fairly similar to those of the PBE-GGA, BP86 [79], and unrestricted Hartree-Fock (UHF) [79] calculations. The PBE-GGA result is about 85% larger than the experimental value, which results in an 85% overestimated Fermi contact contribution in magnitude.

In the case of the ^{55}Mn center in the Mn^+ cation (Table 3.5), the trend of core spin polarization for 1s, 2s, 3s, and 4s orbitals is similar to the FLO-SIC-LDA and all SIC-free DFT results for the ^{55}Mn center in the neutral Mn atom. The only difference is that the 4s-orbital spin polarization is now the largest among the four s shells because it is singly occupied. The total s-orbital spin polarization from FLO-SIC-LDA agrees better with the experimental value than the SIC-free results.

Table 3.6 shows individual s-orbital contributions to the spin density computed from the FLO-SIC-LDA and SIC-free DFT for several other atomic systems. Overall, the FLO-SIC-LDA 1s-orbital spin polarization is positive and it is much larger than the SIC-free result. We also observe that for the FLO-SIC-LDA and SIC-free DFT calculations, for a given electron configuration, the individual s-orbital spin polarization increases in magnitude as the nuclear charge number or atomic number increases. Examples are the Na atoms versus the Mg^+ cation, the K atom versus the Ca^+ cation, and the Cr atom versus the Mn^+ cation.

Table 3.6: Individual s-orbital contributions to the spin density (in μ_B/a_B^3) at the nuclear center for the Na, Mg^+, K, Ca^+, Cr, and Cu atoms. Here "Total" denotes the sum of all s-orbital contributions.

Atom	Orbital	FLOSIC-LDA	LDA	PBE-GGA
Na	Total	0.736	0.786	0.710
[Ne]$3s^1$	1s	0.0204	0.0023	0.0027
	2s	0.0062	-0.0311	-0.0494
	3s	0.709	0.815	0.757
Mg^+	Total	2.034	2.151	2.004
[Ne]$3s^1$	1s	0.051	0.011	0.012
	2s	0.030	-0.071	-0.077
	3s	1.952	2.212	2.069
K	Total	1.109	1.149	1.014
[Ar]$4s^1$	1s	0.1135	0.0044	0.0048
	2s	-0.0491	-0.0072	-0.0083
	3s	0.0182	-0.0151	-0.0213
	4s	1.027	1.167	1.039
Ca^+	Total	2.564	2.712	2.546
[Ar]$4s^1$	1s	0.139	0.014	0.015
	2s	-0.111	-0.014	-0.020
	3s	0.111	-0.026	-0.029
	4s	2.424	2.739	2.581
Cr	Total	2.004	2.027	1.812
[Ar]$3d^5 4s^1$	1s	0.773	-0.053	-0.023
	2s	-1.556	-1.767	-1.820
	3s	-0.039	0.450	0.359
	4s	2.825	3.397	3.296
Cu	Total	4.416	5.004	4.818
[Ar]$3d^{10} 4s^1$	1s	0.047	0.013	0.013
	2s	0.279	0.058	0.083
	3s	0.006	-0.054	-0.057
	4s	4.083	4.986	4.779

This trend is consistent with that from Ref. 79.

For the Na and Mg^+ atom, the FLO-SIC-LDA provides all positive core spin polarization, while the LDA and GGA give positive spin polarization from the $1s$ and $3s$ orbitals and negative spin polarization from the $2s$ orbitals. For the K and Ca^+ cases, the FLO-SIC-LDA provides positive s-orbital spin polarization except for the $2s$-orbitals which give negative spin polarization. The LDA and GGA results provide negative (positive) spin polarization from both $2s$ and $3s$ orbitals ($1s$ and $4s$ orbitals). In the case of the Cr atom, interestingly, the FLO-SIC-LDA $3s$-orbital spin polarization is negative. Other than this the FLO-SIC-LDA spin polarization is very similar to that from the Mn^+ case. In the case of Cu atom, FLO-SIC-LDA provides positive spin polarization from all s-orbitals, with the most significant contribution from the $2s$ orbital. For the SIC-free DFT calculation on the Cu atom, the $3s$ orbital spin polarization is negative and all other s orbitals contribute to positive spin polarization, with the $2s$-contribution much smaller than in FLO-SIC-LDA.. The total s-orbital spin polarization is comparable to that for the FLO-SIC-LDA value.

3.6.3 Molecules without transition-metal elements

We first discuss the Fermi contact contribution for the molecules. Table 3.7 lists the Fermi contact contribution using the FLO-SIC-LDA and SIC-free DFT in comparison to experimental data and previous theoretical results for the six non-TM molecules with the electron spin $S = 1/2$. Figure 3.6 shows the absolute values of the Fermi contact contribution for the considered molecules. For CH_3, HCO, SiH_3, and NF_2 molecules, the absolute value of the FLO-SIC Fermi contact contribution is much larger than the corresponding LDA or GGA value, while for $(H_2CO)^+$ and HSiO molecules, that is not the case. The core spin polarization also occurs for the molecules, but the description of it is more complex than for

the atomic systems. Since the focus of our work is to investigate the effect of SIC, we do not discuss the effect of core spin polarization for the molecules. The FLO-SIC Fermi contact contribution for the ^{13}C center in CH_3 and HCO is somewhat overestimated compared to the experimental data, while the corresponding value for the ^{1}H center for CH_3 and HCO agrees well with the experimental value. For the ^{14}N and ^{19}F centers in NF_2, the FLO-SIC Fermi contact term is about 100% overestimated in magnitude compared to the experimental data. For the ^{13}C and ^{1}H centers in $(H_2CO)^+$, the ^{29}Si and ^{1}H centers in HSiO, and the ^{29}Si center in SiH_3, the FLO-SIC Fermi contact term is significantly underestimated compared to the experimental data. Interestingly, for the ^{19}F center in NF_2, the LDA Fermi contact contribution has opposite sign to the experimental data and the FLO-SIC, PBE-GGA, and B3LYP results. Overall, the FLO-SIC-LDA results are close to the SIC-free LDA results, and they are somewhat worse than the PBE-GGA results, as shown in Table 3.7.

For the considered molecules, there exist spin-dipole contributions to the HF interaction which are described by $A_{\text{dip}} = \frac{1}{3}(A_3 - \frac{1}{2}(A_1 + A_2))$ considering low-symmetry molecules. Here the "3" axis is the molecular symmetry axis. For non-symmetric sites or non-symmetric molecules, A_3 is the largest-magnitude eigenvalue of A^{SD}. Table 3.7 also lists the spin-dipole term using the FLO-SIC-LDA and SIC-free DFT in comparison to experimental data and the literature for the six non-TM molecules. As discussed earlier, the spin-dipole contribution reflects molecular symmetry and spin density distribution within the molecules (see Table 3.1). It is typically much smaller in magnitude than the Fermi contact contribution except for the ^{14}N and ^{19}F centers in NF_2. The FLO-SIC-LDA results are in good agreement with the SIC-free DFT results and B3LYP results except for the ^{19}F center in NF_2. This suggests that the SIC affects mostly the spin density near the nuclear center. The deviation of the FLO-SIC-LDA results from the experimental data ranges from a few to a few tens of MHz.

Table 3.7: Calculated Fermi contact terms A^{FC} and electronic spin-dipole terms $|A_{\mathrm{dip}}|$ for small non-TM molecules (in units of MHz), compared to experimental data and theoretical values from other groups. Here $|A_{\mathrm{dip}}| = |\frac{1}{3}(A_3 - \frac{1}{2}(A_1 + A_2))|$, where the molecular symmetry axis coincides with the "3" axis (for non-symmetric sites or non-symmetric molecules, A_3 is the largest-magnitude eigenvalue of A^{SD}). The definitions of the symbols are the same as in Table 3.3. The experimental values are often reported only in magnitudes or only for isotropic Fermi contact terms. The mean absolute errors and mean absolute percentage errors are summarized in Table 3.7. For the mean absolute errors and mean absolute percentage errors in the spin-dipole contribution, CH_3 and HSiO are not included due to lack of experimental data.

Molecule	Center	Method	Starting FODs	A^{FC}	$\lvert A_{\mathrm{dip}}\rvert$
CH_3	^{13}C	**FLOSIC-LDA** (this work)	Lewis	**123.4**	**78.7**
$S = 1/2$	$I = 1/2$	LDA (this work)		26.4	78.9
		PBE-GGA (this work)		64.4	80.3
		B3LYP Ref. 80		80.8	80.4
		Exp. Ref. 124		107.5	N/A
	^{1}H	**FLOSIC-LDA** (this work)	Lewis	**-70.0**	**20.5**
	$I = 3/2$	LDA (this work)		-49.2	19.7
		PBE-GGA (this work)		-59.8	20.0
		B3LYP Ref. 80		-65.1	20.0
		Exp. Ref. 124		64.6	N/A
HCO	^{13}C	**FLOSIC-LDA** (this work)	GGA-NBO	**461.7**	**48.3**
$S = 1/2$	$I = 1/2$	LDA (this work)		356.5	42.6
		PBE-GGA (this work)		371.9	42.9
		B3LYP Ref. 80		389.1	45.6
		Exp. Ref. 125		377.5	25.2
	^{1}H	**FLOSIC-LDA** (this work)	GGA-NBO	**329.5**	**13.3**
	$I = 3/2$	LDA (this work)		316.5	12.7
		PBE-GGA (this work)		347.1	11.3
		B3LYP Ref. 80		380.0	11.8
		Exp. Ref. 125		380.6	7.7
$(H_2CO)^+$	^{13}C	**FLOSIC-LDA** (this work)	Lewis	**-41.3**	**8.2**
$S = 1/2$	$I = 1/2$	LDA (this work)		-70.3	12.6
		PBE-GGA (this work)		-86.1	11.3
		B3LYP Ref. 80		-85.0	11.2
		Exp. Ref. 126		109	7.3
	^{1}H	**FLOSIC-LDA** (this work)	Lewis	**238.2**	**7.8**
	$I = 3/2$	LDA (this work)		359.3	11.5
		PBE-GGA (this work)		370.5	9.8
		B3LYP Ref. 80		323.9	9.1
		Exp. Ref. 126		372	4.4

Table 3.7 is continued on the next page

Table 3.7 – continued from the previous page

Molecule	Center	Method	Starting FODs	A^{FC}	$\lvert A_{dip}\rvert$
HSiO	^{29}Si	**FLOSIC-LDA** (this work)	GGA-NBO	**-565.8**	**50.8**
$S = 1/2$	$I = 1/2$	LDA (this work)		-569.4	43.9
		PBE-GGA (this work)		-522.0	44.2
		B3LYP Ref. 127		-521.5	N/A
		Exp. Ref. 128		630.0	N/A
	^{1}H	**FLOSIC-LDA** (this work)	GGA-NBO	**393.8**	**2.3**
	$I = 3/2$	LDA (this work)		390.3	3.7
		PBE-GGA (this work)		405.0	3.0
		B3LYP Ref. 127		418.5	N/A
		Exp. Ref. 128		450.0	N/A
SiH_3	^{29}Si	**FLOSIC-LDA** (this work)	Lewis	**-538.2**	**84.6**
$S = 1/2$	$I = 1/2$	LDA (this work)		-425.8	85.5
		PBE-GGA (this work)		-428.0	83.6
		Exp. Ref. 128		665	166.0
	^{1}H	**FLOSIC-LDA** (this work)	Lewis	**45.1**	4.6
	$I = 3/2$	LDA (this work)		21.6	5.2
		PBE-GGA (this work)		19.6	5.1
		Exp. Ref. 128		25	4
NF_2	^{14}N	**FLOSIC-LDA** (this work)	Lewis	**96.5**	**55.1**
$S = 1/2$	$I = 1$	LDA (this work)		2.8	45.3
		PBE-GGA (this work)		21.8	46.7
		B3LYP Ref. 80		43.9	49.3
		Exp. Ref. 129		47.9	45.1
	^{19}F	**FLOSIC-LDA (this work)**	Lewis	**305.8**	**153.8**
	$I = 1/2$	LDA (this work)		-15.5	274.2
		PBE-GGA (this work)		54.0	261.0
		B3LYP Ref. 80		142.7	250.6
		Exp. Ref. 129		168.0	214.6
Mean		**FLOSIC-LDA** (this work)		**67.6**	**23.2**
Absolute		LDA (this work)		68.7	22.0
Error		PBE (this work)		53.9	20.3
Mean		**FLOSIC-LDA** (this work)		**38.6%**	**46.3%**
Absolute %		LDA (this work)		36.4%	59.5%
Error		PBE (this work)		23.8%	49.7%

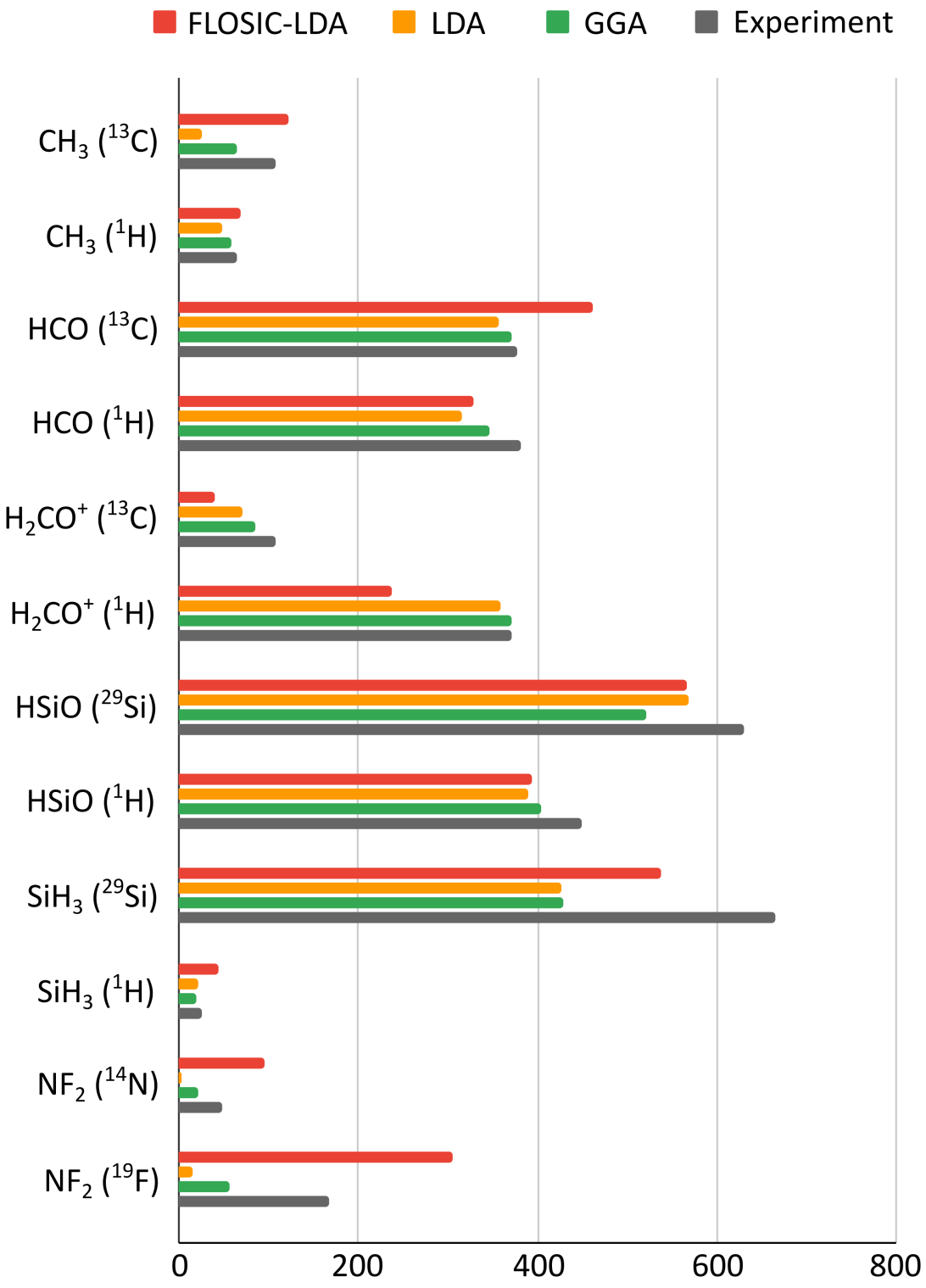

Figure 3.6: The absolute values of the Fermi contact terms for the considered molecules in Table 3.7, in MHz

3.6.4 Transition-metal molecules

Table 3.8 shows the Fermi contact contribution calculated using the FLO-SIC-LDA and SIC-free DFT for the ^{47}Ti center in TiF_3 and for the ^{55}Mn centers in the Mn-based molecules compared to experimental data and previous theoretical reports. Figure 3.7 shows the absolute value of the Fermi contact contribution for the TM-based molecules. Overall, the FLO-SIC-LDA Fermi contact contribution is underestimated compared to the LDA value except for the ^{55}Mn center for MnO. For the ^{55}Mn center in MnF_2, MnO, MnO_2, and MnO_3, the FLO-SIC Fermi contact term is closer to the experimental value than the LDA or GGA value. The FLO-SIC mean absolute percentage error for the considered TM-based molecules is about two-thirds of the LDA or GGA error. For the spin-dipole contribution, the FLO-SIC mean absolute percentage error is only slightly worse than the LDA or GGA error. This may be due to slightly broken molecular symmetry of the FLO-SIC spin density distribution as shown in Table 3.2.

Table 3.8: Calculated Fermi contact and spin-dipole contributions to the HF interaction for small Ti- and Mn-based molecules (in units of MHz) compared to experimental data and previous theoretical results. The definitions of the symbols are the same as in Tables 3.3 and 3.7. The experimental values are often reported only in magnitudes or only for isotropic Fermi contact terms.

Molecule	Center	Method	Starting FODs	A^{FC}	$\lvert A_{dip}\rvert$
TiF_3	^{47}Ti	**FLOSIC-LDA** (this work)	Trial-Error	**-118.6**	**15.6**
$S = 1/2$	$I = 5/2$	LDA (this work)		-212.7	10.9
		PBE-GGA (this work)		-195.5	10.0
		B3LYP Ref. 80		-205.6	9.9
		B3LYP Ref. 81		-197.5	10.2
		SCAN Ref. 81		48.1	15.6
		Exp. Ref. 100		-185	7

Table 3.8 is continued on the next page

Table 3.8 – continued from the previous page

Molecule	Center	Method	Starting FODs	A^{FC}	$\lvert A_{dip}\rvert$
MnF	^{55}Mn	**FLOSIC-LDA** (this work)	GGA-NBO	**375.9**	**9.3**
$S = 3$	$I = 5/2$	LDA (this work)		397.7	5.9
		PBE-GGA (this work)		356.9	6.0
		B3LYP Ref. 80		495.9	7.0
		B3LYP Ref. 81		441.8	16.5
		SCAN Ref. 81		511.2	13.7
		Exp. Ref. 130		442	24
MnF_2	^{55}Mn	**FLOSIC-LDA** (this work)	GGA-NRT	**140.9**	**1.4**
$S = 5/2$	$I = 5/2$	LDA (this work)		188.6	7.9
		PBE-GGA (this work)		159.8	7.3
		Exp. Ref. 130		134	10
MnO	^{55}Mn	**FLOSIC-LDA** (this work)	Lewis	**479.0**	**29.5**
$S = 5/2$	$I = 5/2$	LDA (this work)		435.9	27.3
		PBE-GGA (this work)		408.6	26.9
		B3LYP Ref. 80		567.7	22.8
		Exp. Ref. 131		479.9	16
MnO_2	^{55}Mn	**FLOSIC-LDA** (this work)	GGA-NBO	**491.3**	**28.1**
$S = 3/2$	$I = 5/2$	LDA (this work)		877.2	66.2
		PBE-GGA (this work)		813.9	64.1
		Exp. Ref. 101		603	126
MnO_3	^{55}Mn	**FLOSIC-LDA** (this work)	MOLCAS	**1747.5**	**111.4**
$S = 1/2$	$I = 5/2$	LDA (this work)	-NBO	1857.6	102.4
		PBE-GGA (this work)		1738.1	100.7
		B3LYP Ref. 80		-71.2	21.3
		B3LYP Ref. 81		1667.8	128.5
		SCAN Ref. 81		1828.5	97.2
		Exp. Ref. 101		1613	81
$(Mn(H_2O)_6)^{2+}$	^{55}Mn	**FLOSIC-LDA** (this work)	Lewis	**-224.3**	**0.98**
$S = 5/2$	$I = 5/2$	LDA (this work)		-268.8	0.07
		PBE-GGA (this work)		-293.9	0.14
		B3LYP Ref. 80		-173.5	0.3
		B3LYP Ref. 81		-161.3	0.1
		SCAN Ref. 81		-219.0	0.1
		Exp. Ref. 132		∼250	N/A
Mean Absolute Error		**FLOSIC-LDA** (this work)		**58.9**	**28.9**
		LDA (this work)		101.2	19.4
		PBE-GGA (this work)		81.8	19.4
Mean Absolute % Error		**FLOSIC-LDA** (this work)		**13.3%**	**78.1%**
		LDA (this work)		20.4%	49.2%
		PBE-GGA (this work)		17.0%	47.6%

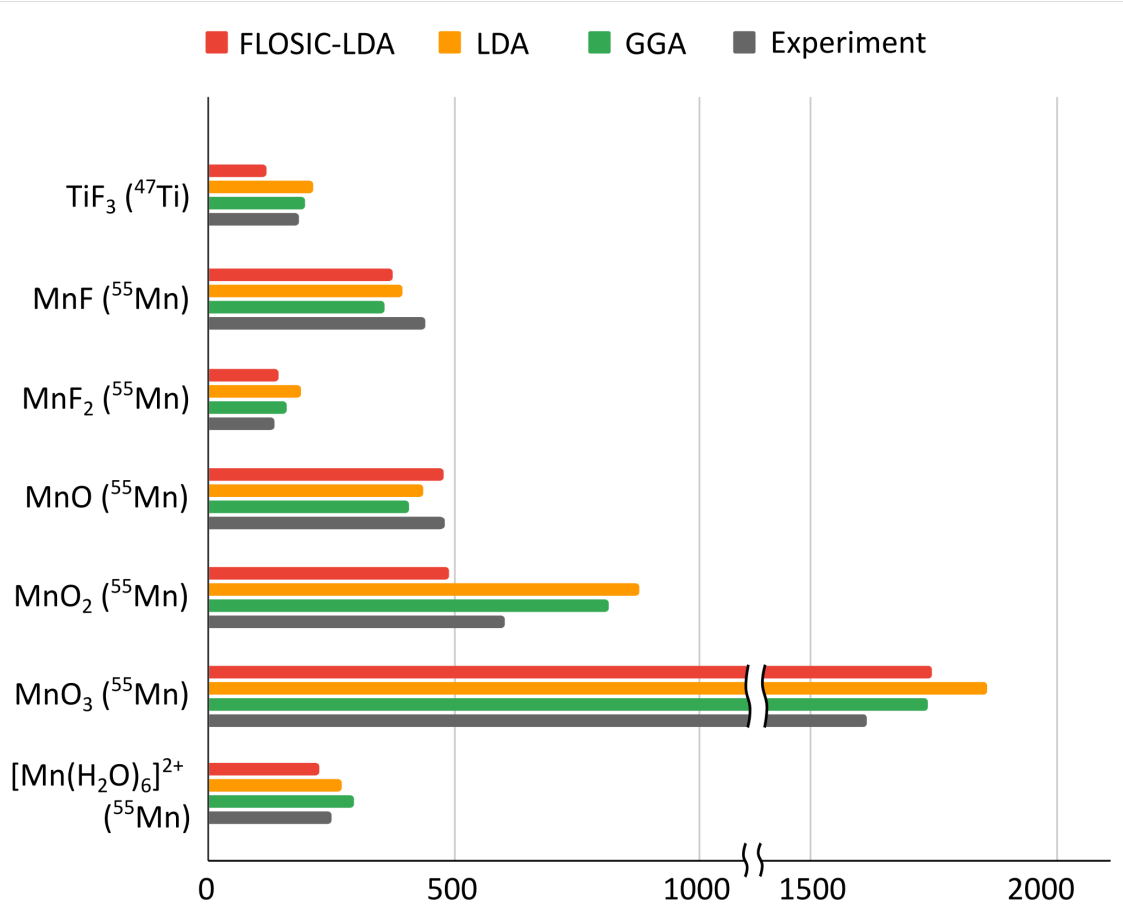

Figure 3.7: The absolute values of the Fermi contact contribution for the TM-based molecules in Table 3.8, in MHz

3.7 Basis Set Effects

Table 3.9 shows the effects of the uncontracted basis sets on the Fermi contact contribution for the considered atoms using the FLO-SIC-LDA and LDA. For the ^{7}Li, ^{25}Mg^{+}, ^{43}Ca^{+}, ^{53}Cr, and ^{63}Cu centers, the uncontracted basis sets give rise to the FLO-SIC Fermi contact contribution closer to the experimental value than the contracted basis sets. However, for

Table 3.9: Fermi contact contribution for atoms using uncontracted and contracted basis sets within the FLO-SIC and SIC-free DFT.

Atom	Method	Contracted	Uncontracted
^{1}H	**FLOSIC-LDA**	1330.4	1331.2
	LDA	1267.5	1264.4
	Exp. Ref. 116	1420.4	
^{3}Li	**FLOSIC-LDA**	423.6	409.8
	LDA	392.2	385.2
	Exp. Ref. 117	401.8	
^{23}Na	**FLOSIC-LDA**	870.2	961.1
	LDA	929.5	970.8
	Exp. Ref. 117	885.8	
^{25}Mg^{+}	**FLOSIC-LDA**	-556.9	-611.3
	LDA	-589.1	-619.4
	Exp. Ref. 118	-596.0	
^{39}K	**FLOSIC-LDA**	231.6	254.3
	LDA	240.0	241.6
	Exp. Ref. 117	230.9	
^{43}Ca^{+}	**FLOSIC-LDA**	-772.1	-832.1
	LDA	-816.8	-817.7
	Exp. Ref. 119	-806.0	
^{53}Cr	**FLOSIC-LDA**	-84.8	-98.8
	LDA	-85.5	-106.6
	Exp. Ref. 115	-94.6	
^{55}Mn^{+}	**FLOSIC-LDA**	756.4	832.9
	LDA	737.5	857.3
	Exp. Ref. 101	770.0	
^{55}Mn	**FLOSIC-LDA**	-94.3	10.3
	LDA	-127.2	16.3
	Exp. Ref. 120	-78.1	
^{63}Cu	**FLOSIC-LDA**	5236.9	5137.9
	LDA	5935.1	5923.6
	Exp. Ref. 121	5867.0	
Mean Absolute Error	**FLOSIC-LDA**	87.1	112.2
	LDA	39.2	55.4
Mean Absolute % error	**FLOSIC-LDA**	6.8%	17.1%
	LDA	10.2%	18.1%
Mean Absolute Error (w/o Mn)	**FLOSIC-LDA**	95.0	114.8
	LDA	38.1	51.0
Mean Absolute % Error (w/o Mn)	**FLOSIC-LDA**	5.3%	6.4%
	LDA	4.4%	6.6%

Table 3.10: Fermi contact contribution for the non-TM-based molecules using uncontracted and contracted basis sets within the FLO-SIC-LDA and SIC-free DFT.

Molecule	Method	Contracted	Uncontracted
CH_3 (^{13}C)	**FLOSIC-LDA**	123.4	117.7
	LDA	26.4	25.8
	Exp. Ref. 124	107.5	
CH_3 (^{1}H)	**FLOSIC-LDA**	-70.0	-70.6
	LDA	-49.2	-49.5
	Exp. Ref. 124	-64.6	
HCO (^{13}C)	**FLOSIC-LDA**	461.7	448.7
	LDA	356.5	352.9
	Exp. Ref. 125	377.5	
HCO (^{1}H)	**FLOSIC-LDA**	329.5	328.3
	LDA	316.5	316.1
	Exp. Ref. 125	380.6	
$(H2CO)^+$ (^{13}C)	**FLOSIC-LDA**	-41.3	-41.0
	LDA	-70.3	-69.0
	Exp. Ref. 125	-109.0	
$(H2CO)^+$ (^{1}H)	**FLOSIC-LDA**	238.2	238.2
	LDA	359.3	358.6
	Exp. Ref. 125	372.0	
HSiO (^{29}Si)	**FLOSIC-LDA**	-565.8	-611.0
	LDA	-569.4	-578.3
	Exp. Ref. 128	-630.0	
HSiO (^{1}H)	**FLOSIC-LDA**	393.8	390.6
	LDA	390.3	387.1
	Exp. Ref. 128	450.0	
SiH_3 (^{29}Si)	**FLOSIC-LDA**	-538.2	-589.4
	LDA	-425.8	-424.0
	Exp. Ref. 128	-665.0	
SiH_3 (^{1}H)	**FLOSIC-LDA**	45.1	44.5
	LDA	21.6	21.5
	Exp. Ref. 128	25.0	
NF_2 (^{14}N)	**FLOSIC-LDA**	96.5	102.5
	LDA	2.8	9.9
	Exp. Ref. 129	47.9	
NF_2 (^{19}F)	**FLOSIC-LDA**	305.8	338.1
	LDA	-15.5	32.8
	Exp. Ref. 129	168.0	
Mean Absolute Error	**FLOSIC-LDA**	67.6	61.6
	LDA	68.7	64.3
Mean Absolute % Error	**FLOSIC-LDA**	38.6%	39.2%
	LDA	36.4%	32.9%

Table 3.11: Fermi contact contribution for the TM-based molecules using uncontracted and contracted basis sets within the FLO-SIC-LDA and SIC-free DFT.

Molecule	Method	Contracted	Uncontracted
TiF_3 (^{47}Ti)	**FLOSIC-LDA**	-118.6	-120.7
	LDA	-212.7	-225.3
	Exp. Ref. 100	-185.0	
MnF (^{55}Mn)	**FLOSIC-LDA**	375.9	478.4
	LDA	397.7	510.1
	Exp. Ref. 130	442.0	
MnF_2 (^{55}Mn)	**FLOSIC-LDA**	140.9	226.1
	LDA	188.6	315.8
	Exp. Ref. 130	134.0	
MnO (^{55}Mn)	**FLOSIC-LDA**	479.0	548.2
	LDA	435.9	545.9
	Exp. Ref. 131	479.9	
MnO_2 (^{55}Mn)	**FLOSIC-LDA**	491.3	615.3
	LDA	877.2	1019.1
	Exp. Ref. 101	603.0	
MnO_3 (^{55}Mn)	**FLOSIC-LDA**	1747.5	1578.5
	LDA	1857.6	1995.4
	Exp. Ref. 101	1613.0	
$(Mn(H_2O)_6)^{2+}$ (^{55}Mn)	**FLOSIC-LDA**	-224.2	-140.1
	LDA	-268.8	-148.4
	Exp. Ref. 132	-250.0	
Mean Absolute Error	**FLOSIC-LDA**	58.9	59.7
	LDA	101.2	179.5
Mean Absolute % Error	**FLOSIC-LDA**	13.3%	24.9%
	LDA	20.4%	45.7%

the other atoms, the uncontracted basis sets make the deviation of the FLO-SIC result from the experimental data slightly larger. One extreme case is the Mn atom. In this case, with the uncontracted basis sets, the Fermi contact contribution even changes the sign. The mean absolute percentage error for all the considered atoms suggests that with the uncontracted basis sets, the FLO-SIC-LDA result is comparable to the LDA result.

Uncontracting the basis set provides greater variational freedom to the orbitals that can result in changes in the spin polarization of the s-orbitals at the nuclear site. However, fully uncontracting the basis to single Gaussian orbitals comes at the cost of a vastly larger basis. For the Mn atom, for example, the default basis utilizes 20 Gaussian exponents for 7 s-type, 5 p-type, and 3 d-type functions, or a total of 40 functions (3 for each p-type and 6 for each Cartesian d-type orbital). The fully uncontracted basis contains 200 functions. Since the $1s$ function has the largest amplitude at the nuclear site, it is worth considering whether the effect of uncontracting the basis can be captured by including only the effect on the $1s$ function. This can be done by substituting the $1s$ up and $1s$ down orbitals taken from an uncontracted calculation for the single $1s$ function in the default basis. We call this the modified default basis below. We find Fermi contact terms of -127 MHz, -33 MHz and +16 MHz for the default basis, the modified default basis, and the fully uncontracted basis, respectively. Thus, the modified default basis captures about 2/3 of the effect of the fully uncontracted basis, while adding only a single extra function.

Table 3.10 shows the effects of the uncontracted basis sets on the Fermi contact contribution for the considered non-TM-based molecules. For the ^{13}C center in CH_3 and HCO and the ^{29}Si center in HSiO and SiH_3, the uncontracted basis sets make the FLO-SIC result agree better with the experimental data than the contracted basis sets. For the ^{14}N and ^{19}F centers in NF_2, the uncontracted basis sets make the FLO-SIC result more overestimated than the contracted basis sets. For the rest of the molecules, the uncontracted and contracted basis

sets provide almost the same Fermi contact contribution within the FLO-SIC. Overall, the effect of the uncontracted basis sets is negligible.

Table 3.11 shows the effects of the uncontracted basis sets on the Fermi contact contribution for the considered TM-based molecules. For the ^{55}Mn center in MnF, MnO_2 and MnO_3, the FLO-SIC Fermi contact contribution with the uncontracted basis sets agree better with the experimental data than that with the contracted basis sets. However, for the ^{55}Mn center in MnF_2 and MnO, the uncontracted basis sets make the FLO-SIC result more overestimated than the contracted basis sets. For the ^{55}Mn center in $(Mn(H_2O)_6)^{2+}$, with the uncontracted basis sets, the FLO-SIC result is severely underestimated in magnitude compared to the experimental value. Overall, in the case of uncontracted basis sets, the FLO-SIC mean absolute percentage error for the molecules remains half of the corresponding LDA error, although the uncontracted basis sets increase both the FLO-SIC and LDA mean absolute percentage errors compared to the contracted basis sets.

The results for uncontracted basis sets with added narrow Gaussian functions are presented in Appendix 3.9.3. The effect from adding these narrow functions on the hyperfine constants is much smaller compared to the one from uncontracting the basis set. In the case of the Mn atom, for example, while using the uncontracted basis set changes the magnitude of the Fermi contact term by about 140 MHz and results in a change in its sign, augmenting the basis set only changes the Fermi contact term by 0.4 MHz, which is negligible in comparison.

3.8 Conclusion

We have studied the HF interaction for atomic systems and simple molecules including TM elements by applying the FLO-SIC method within the non-relativistic limit. For the considered molecules, several starting FOD positions were generated by employing the Lewis

theory, the fodMC code, the NBO analysis, the NRT analysis, MOLCAS calculations, and a trial-and-error method. The converged FOD positions with the lowest SIC energy and molecular symmetry were used to compute the HF interaction. For the light to moderately heavier atomic systems ($Z \leq 25$), the Fermi contact contribution from the FLO-SIC-LDA calculations agree much better with the experimental data than that from the LDA or GGA calculations. This might be attributed to a better description of the core spin polarization. For the non-TM-based molecules, the Fermi contact contribution from the FLO-SIC-LDA calculations is comparable to that from the LDA or GGA calculations. For the Ti- or Mn-based molecules, the FLO-SIC-LDA Fermi contact term agrees better with the experimental data than the LDA or GGA result. We confirm that the original default `FLOSIC` basis sets contain narrow enough Gaussian functions by computing the Fermi contact contribution using the uncontracted basis set. Our results may stimulate further studies of the HF interaction for other TM-based molecules using the FLO-SIC or other SIC methods.

3.9 Appendix

3.9.1 Starting FODs for some TM-based molecules

Figure 3.8 shows schematic initial FOD configurations for the TM-based molecules which are identified by using NBO, NRT, or trial-and-error methods. For the TiF_3 molecule, the Lewis picture predicts a single bond between the Ti atom and each of the F atoms, while the NBO analysis based on PBE-GGA density predicts a single bond with one of the F atoms as well as double bonds with the other two F atoms. However, this broken-symmetry configuration results in somewhat unbalanced electronic structure in terms of the spin density distribution and the Fermi contact contribution on the F sites and spin-dipole components of the Ti site.

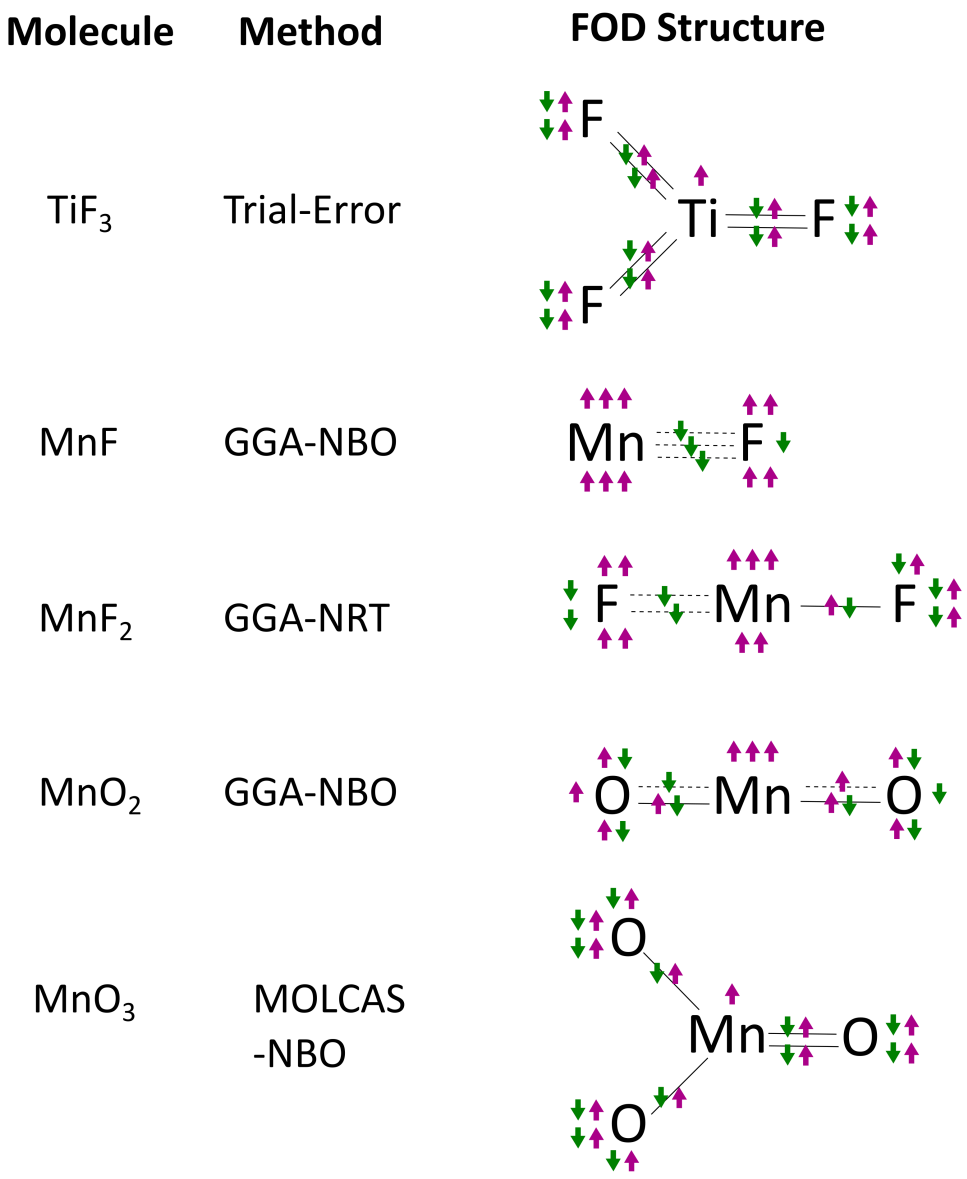

Figure 3.8: The starting FOD configurations for some TM-based molecules.

With the trial-and-error method, we find a starting FOD bonding picture which results in the lowest converged energy and a symmetric electronic structure. In this picture, there are two pairs of FODs between the Ti and every F atom. Furthermore, final bonding FODs come sufficiently close to the F atoms such that the bonds can be highly polarized or even ionic, and the bonding FODs affect more the F valence FOD orientations rather than the nature of the bonds themselves. For the MnF_2 molecule, the NBO prediction is that one of the F atoms is not bonded to the Mn atom. Therefore, we use instead the dominant configurations from NRT analysis, in which there is a double spin-down bond with one of the F atoms and single spin-up and spin-down bonds with the other F atom. For the MnO_3 molecule, the starting FOD configuration is generated based on the CASSCF calculation that is described in Appendix 3.9.2.

3.9.2 MnO_3 CASSCF calculation

The CASSCF calculation for the MnO_3 molecule is performed using the `MOLCAS` version 8.2 code [65]. The calculation is performed with an active space of nine orbitals, containing nine electrons (CAS(9,9)). The starting orbitals are taken from a preliminary restricted Hartree-Fock (CAS(1,1)) calculation. The active space is initialized from the orbitals with the largest $3d$-character. In the final calculation, the active space orbitals contain mostly the contributions from Mn $3d$ and oxygen $2p$ orbitals; the SOMO is dominated by Mn $3d_{z^2}$ (Fig.3.9). The resulting electron density from this configuration is fed into the NBO program (using the `Molden2Aim` interface [107]) to generate a bonding picture shown in Fig. 3.8.

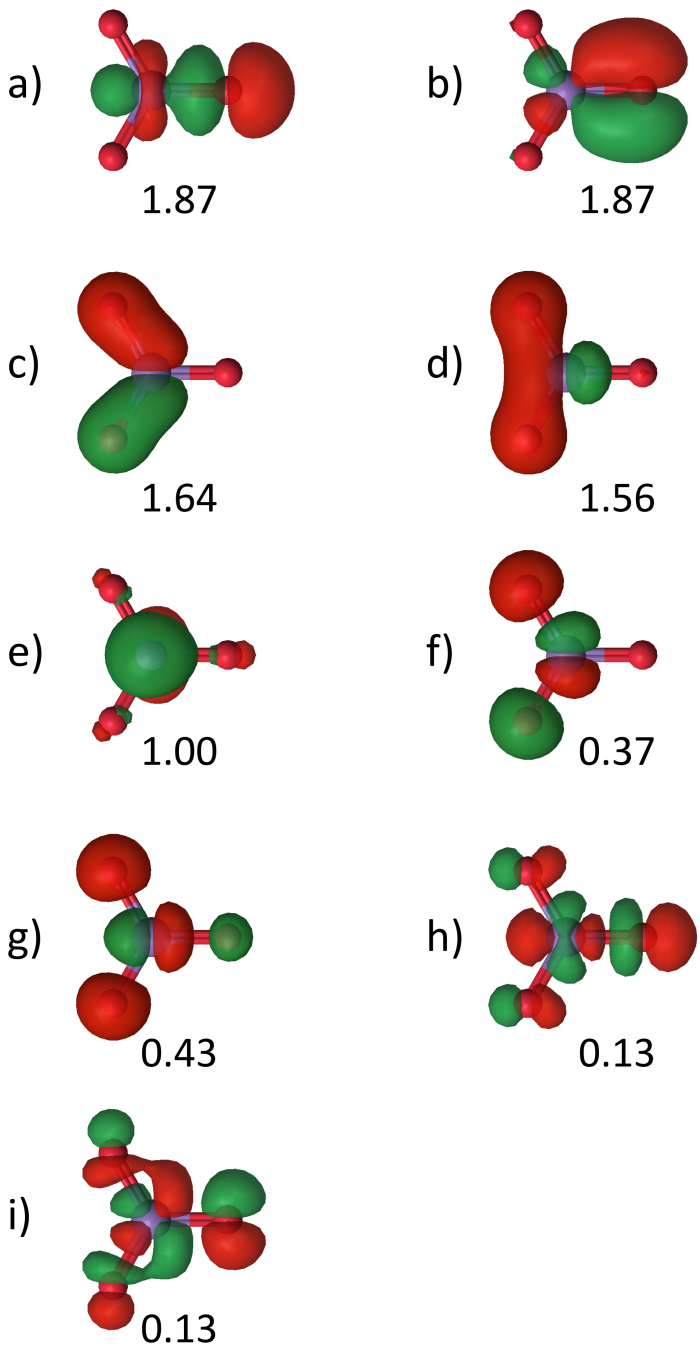

Figure 3.9: The active space for MnO_3 with average occupation numbers printed below them. Orbital (e) represents the SOMO.

3.9.3 Basis Set Added Gaussians

For a better description of the region near the nuclear site, we modify the basis set files for each atom by adding five narrow Gaussian exponents in an even-tempered way (Table 3.12). The values of the Fermi contact terms calculated on the standard, uncontracted, and uncontracted+augmented basis sets for some systems are shown in Table 3.13. We observe that the major alteration of the Fermi contract terms occur after uncontraction of the basis sets, while adding more narrow Gaussians does not seem to make much difference. This may indicate that the original default `FLOSIC` basis sets contain narrow enough Gaussian functions, and simply allowing them to vary independently from other Gaussians (achieved by uncontraction) may be sufficient for the proper description of the region near the nuclear site.

Table 3.12: Added Gaussian exponents for each atom. The first two lines show two largest exponents from the default basis set in each case (N is the total number of basis function exponents); the next line shows the ratios between these values; finally, the following five lines ($N+1$ to $N+5$) show the added exponents for the new skinny Gaussians in the augmented basis sets, with every next exponent larger than the previous one by the same ratio from the third row.

Expo #	H	Li	Na	Mg^+	K	Ca^+	Cr	Mn	Mn^+	Cu
$N-1$	1.153e+1	4.780e+2	3.801e+4	4.765e+4	2.080e+5	2.585e+5	5.168e+5	5.216e+5	5.216e+5	6.895e+5
N	7.784e+1	3.200e+3	2.515e+5	3.153e+5	1.397e+6	1.777e+6	3.490e+6	3.585e+6	3.585e+6	4.763e+6
Ratio	6.749	6.696	6.616	6.617	6.715	6.875	6.752	6.873	6.873	6.907
$N+1$	5.253e+2	2.143e+4	1.664e+6	2.087e+6	9.378e+6	1.222e+7	2.356e+7	2.464e+7	2.464e+7	3.290e+7
$N+2$	3.545e+3	1.435e+5	1.101e+7	1.381e+7	6.297e+7	8.401e+7	1.591e+8	1.693e+8	1.693e+8	2.272e+8
$N+3$	2.392e+4	9.606e+5	7.282e+7	9.136e+7	4.228e+8	5.776e+8	1.074e+9	1.164e+9	1.164e+9	1.570e+9
$N+4$	1.615e+5	6.432e+6	4.817e+8	6.045e+8	2.839e+9	3.971e+9	7.253e+9	8.000e+9	8.000e+9	1.084e+10
$N+5$	1.090e+6	4.307e+7	3.187e+9	4.000e+9	1.907e+10	2.730e+10	4.897e+10	5.498e+10	5.498e+10	7.489e+10

Table 3.13: Fermi-contact terms for several atoms, ions and molecules, with contracted, uncontracted, and uncontracted+augmented basis sets

System	Experiment	LDA			FLO-SIC-LDA		
		Contr.	Unc.	Unc.+5 Gauss.	Contr.	Unc.	Unc.+5 Gauss.
Na	885.8	929.5	970.8	982.5	870.2	961.1	972.8
Mg^+	-596	-589.1	-619.4	-626.7	-556.9	-611.3	-618.4
Cr	-94.6	-85.5	-106.6	-107.3	-84.8	-98.8	-99.8
Mn^+	770	737.5	857.3	863.7	756.4	832.9	838.7
Mn	-78.1	-127.2	16.3	16.7	-94.3	10.3	10.2
Cu	5867	5935.1	5923.6	5965.3	5236.9	5137.9	5172.0
CH_3 (^{13}C)	107.5	26.4	25.8	26.3	123.4	117.7	120.1
CH_3 (^{1}H)	-64.6	-49.2	-49.5	-52.7	-70	-70.6	-75.2
HCO (^{13}C)	377.5	356.5	352.9	360.9	461.7	448.7	460.6
HCO (^{1}H)	380.6	316.5	316.1	336.9	329.5	328.3	349.3
MnF (^{55}Mn)	442	397.7	510.1	513.8	375.9	478.4	482.7
MnO (^{55}Mn)	479.9	435.9	545.9	549.9	479	548.2	551.4

Chapter 4

Multireference study of a Si vacancy center in 4H-SiC

This chapter is based on a manuscript in progress.

4.1 Introduction

The electronic properties of deep-point defects in wide-bandgap semiconductors have been an active area of research due to their promising quantum-information science and quantum sensing applications [133, 134, 135, 136, 137, 138, 139, 140, 141, 142, 143, 144, 145]. With localized electronic states situated within the bandgap, defects combine the advantages of atomic and solid-state systems, and may have useful properties such as long spin-lattice relaxation and spin-coherence times at room temperature [138, 142, 146, 147, 148] and optical initialization, control, and read-out of quantum states [133, 139, 149]. Among these systems, negatively-charged silicon monovacancies (V_{Si}^{-}) in 4H-polytype of silicon carbide (SiC) have been of special interest due to the availability of mature-fabrication techniques [150, 151, 152], and a number of favorable properties, such as long spin coherence times at room temperature [142] and excitation wavelengths in the telecom range [140, 153].

A number of theoretical studies have been performed on the V_{Si}^{-} center [3, 154, 155, 156, 157], finding that the observed ground state has spin $S = \frac{3}{2}$ and that the calculated excitation en-

ergy of the first-excited quartet agrees reasonably with the experimental data [158]. However, most of these estimates were obtained by performing density functional theory (DFT) calculations [154, 155], or many-body perturbation theory and configuration interaction methods that were based on a preliminary DFT result [156]. However, it is known that DFT can fail to provide an accurate description of systems with strong electronic correlations. For instance, in a study of a different wide-bandgap semiconductor defect, a nitrogen vacancy in diamond (NV^--center), some published DFT calculations provided contradicting predictions for the ordering of singlet states and the energy differences between excited singlet and triplet states [159, 160, 161, 162, 163, 164, 165, 166]. However, a multiconfigurational calculation applied to hydrogen-passivated finite diamond clusters has accurately predicted both the ordering and the energies of the excited singlet states of the NV^--center [167]. For the Si vacancy in SiC, similar inconsistencies might occur for the ordering and energies of excited doublet states. Currently, it is difficult to judge whether this is the case on the basis of the published work. The reasons are that there are no available experimental data for the doublet states, and that most of DFT-based results do not discuss the doublet states. The potential discrepancies may be an obstacle to our understanding of intersystem crossings between states with different spin multiplicities which plays an important role in initialization and read-out of qubits based on the Si vacancy [168]. It is therefore evident that beyond-DFT multireference methods could be essential for the description of quantum-information-science-related properties of the defect.

In this work, we study the electronic properties of the negatively-charged silicon vacancy at the *h*-site of the 4H-SiC crystal with multireference quantum chemistry methods. The CASSCF and CASPT2 calculations were performed on hydrogen-passivated symmetric clusters of two different sizes to identify the ground and the excited states of both $S = \frac{3}{2}$ and $S = \frac{1}{2}$ spin states. Results are reported for two active space sizes, in order to analyze the

effect of the choice of active orbitals. The predicted excited-level ordering and excitation energies are compared with the experimental results and the results of previously-published calculations.

This work is structured as follows. In Section 4.2, we describe the qualitative properties of the studied silicon vacancy. In Sec. 4.3, we elaborate on how the passivated clusters were formed for our calculations. In Sec.4.4, we describe the principles of the CASSCF and CASPT2 methods, the choice of the active spaces, and the set-up for our computations. In Sec. 4.5, we discuss the results of our computations: the ordering of quartet and doublet states, the composition of the excited-level wavefunctions, and the excitation energies compared with the experimental and published theoretical results. Finally, Sec.4.6 summarizes the results.

4.2 Silicon Monovacancy Defect in 4H-SiC

The V_{Si}^{-} vacancy defect studied in this work is formed by removing a Si atom from an h-site of the 4H polytype of the SiC crystal. (The difference between the nonequivalent quasihexagonal h and quasicubic k positions of Si atoms in 4H-SiC is explained in Fig.4.1-a.) As a result, the crystal's total C_{6v} point-group symmetry is lowered to C_{3v}, with three σ mirror-symmetry planes and two threefold rotational symmetries C_3. The four carbon atoms surrounding the vacancy form a near-tetrahedral configuration, with one "axial" atom positioned along the C_3 symmetry axis, and three equivalent "lateral" ones around it (see Fig. 4.1). With the Si atom removed, four dangling carbon sp_3 bonds remain (labeled a-d, with d coming from the axial carbon), each hosting one unpaired electron. These dangling bonds contribute to the following symmetric molecular orbitals[3]: $u = \alpha_u(a+b+c) + \beta_u d$, $v = \alpha_v(a+b+c) + \beta_v d$, $e_x = \alpha_x(2c-a-b)$, and $e_y = \alpha_y(a-b)$, where $\alpha_{u,v,x,y}$ and $\beta_{u,v}$ are some coefficients. Orbitals u and v transform under the A_1 irreducible representation

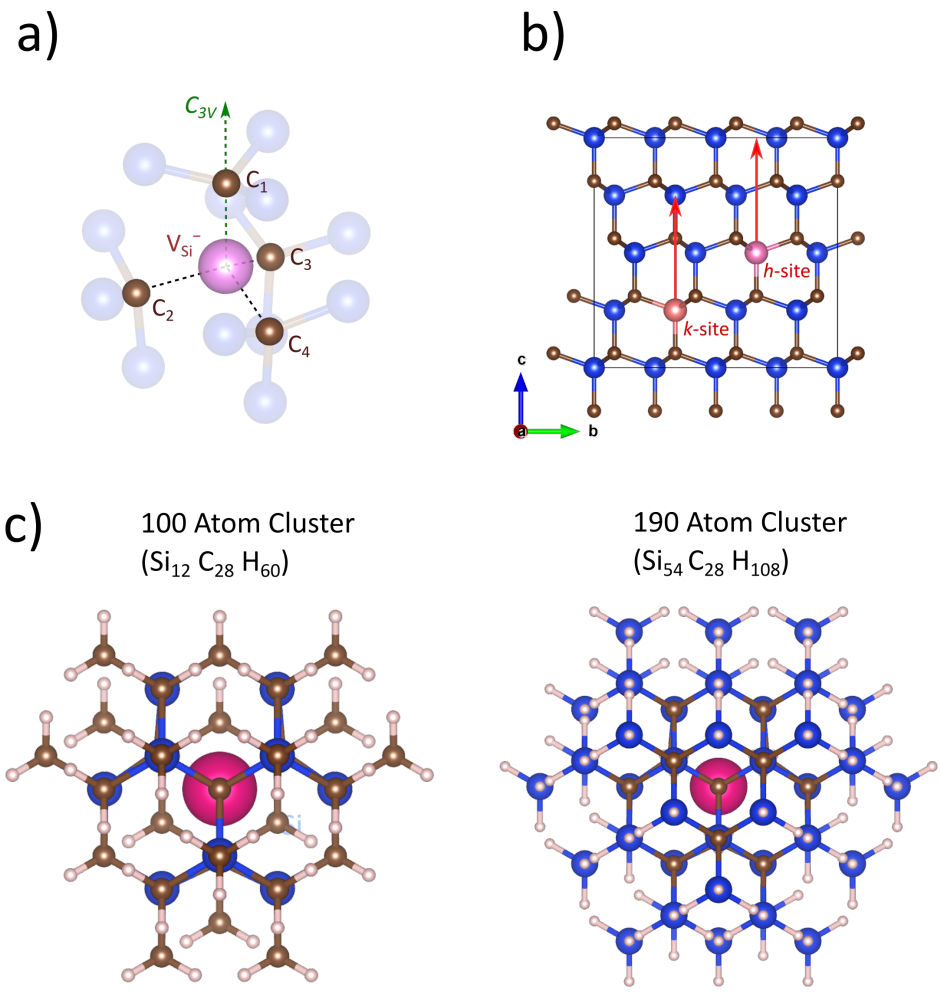

Figure 4.1: a) Silicon vacancy, h-site V_{Si}^-, marked with a purple sphere, inside a piece of SiC crystal. The four nearest-neighbor carbons ($C_1 - C_4$) are arranged in a near-tetrahedral configuration around the vacancy, with one of the carbons (C_1) positioned along the C_{3v} symmetry axis. b) The difference between nonequivalent Si h- and k-sites in 4H-SiC. For an k-site Si atom, there is a second-nearest Si atom aligned with it along the C_{3v} symmetry axis (depicted here with a red arrow). For an h-site Si atom, there is no second-nearest Si atom aligned with it along the symmetry axis. c) Geometries of the 100-atom and 190-atom hydrogen-passivated SiC clusters, as viewed flong the C_{3v} symmetry axis. The vacancy position at the center of each cluster is again marked with a purple sphere.

(IRRep) of the C_{3v} point group, and the doubly-degenerate orbitals e_x and e_y transform under the E IRRep. Furthermore, given that the four neighboring carbons have an almost-perfect tetrahedral symmetry around the vacancy site, it is expected that $\alpha_u \approx \beta_u$ and $\beta_v \approx -3\alpha_v$ [3]. The v, e_x, and e_y defect orbitals are located within the band gap, while u is slightly below the top of the valence band. These single-electron molecular orbitals are populated by 5 electrons, with one added due to the -1 charge state. As has been experimentally observed [169], the ground state of the defect has $S = \frac{3}{2}$, with the nominally doubly-occupied u-orbital and singly-occupied v, e_x, and e_y orbitals.

4.3 Molecular Cluster Description

To calculate the properties of the V_{Si}^{-} center in SiC, we performed calculations on two vacancy-centered, hydrogen-passivated symmetric clusters: $Si_{12}C_{28}H_{60}$ (containing 100 atoms) and $Si_{54}C_{28}H_{108}$ (190 atoms, see Fig. 4.1). To obtain the geometries for these clusters, we used the optimized geometry for a 576-atom supercell of SiC with a V_{Si}^{-} defect obtained from our collaborator, Pratibha Dev, from Howard University [3]. The relaxation calculation was performed with the Quantum ESPRESSO code [170], employing DFT with Perdew-Burke-Ernzerhof (PBE) GGA exchange-correlation functional [23]. A $6 \times 6 \times 2$ k-point grid and ultrasoft pseudopotentials with scalar relativistic terms and non-local core corrections were used. The symmetric cluster geometries were then "carved out" around the vacancy center from the optimized supercell, by including only the atoms near the point defect. For example, the 100-atom cluster includes the 4 C atoms closest to the vacancy, 12 Si atoms bonded to them, and another layer of 24 C atoms neighboring those Si atoms. In the 190-atom cluster, an additional layer of Si atoms is added outside. Finally, the dangling bonds of the outermost-layer atoms are passivated with hydrogens. During passivation, all C-H bond

lengths were set to a standard value of 1.09 Å, and all Si-H bond lengths were set to 1.48 Å, without further relaxation.

4.4 Quantum Chemistry Methods

All multireference calculations on the clusters were performed using **OPENMOLCAS** package [171]. We used all-electron atomic-natural-orbital basis sets with relativistic core corrections (ANO-RCC) [69, 172]. For Si and C, we used polarized double-zeta basis functions, while for H atoms we used the minimal basis. The calculations were performed in several steps: (i) state-averaged complete active-space self-consistent field (SA-CASSCF); (ii) complete active-space second order perturbation theory (CASPT2).

4.4.1 CASSCF

In multiconfigurational quantum-chemistry methods, the total wavefunction is represented by a linear combination of multiple Slater determinants (configurations). Within CASSCF [13, 14, 15, 16], these determinants are assumed to share the same set of single-electron orbitals. These orbitals are divided into three sets: (i) inactive orbitals, which are doubly-occupied for all configurations; (ii) virtual orbitals with zero occupation in all configurations; (iii) active orbitals, which have variable occupations. The CASSCF method considers the linear combination of configurations with all possible occupations within the set of chosen active orbitals (active space, or AS) and for a given number of electrons residing in the active space. The total wavefunction is then optimized with respect to the orbital shapes and the expansion coefficients of the determinants, known as the CI coefficients. The result of this calculation strongly depends on the quality and size of the active space. On the one

hand, an increased AS would allow for a more accurate estimation of electron correlation effects. On the other hand, since all possible AS excitations are considered, the complexity of these calculations will grow quickly with the size of the AS. Therefore, a wise choice of active orbitals is crucial for the successful CASSCF calculations. The result of a CASSCF calculation can provide us both the properties of the ground state and the excited states.

For each cluster, first a set of guess orbitals was generated by running a restricted open shell Hartree-Fock calculation (ROHF). Then, the converged orbitals were symmetrized using the **OPENMOLCAS** interface to the **LIBMSYM** package [173], which allows the program to operate with the C_{3v} symmetry point group. From the set of symmetrized orbitals, we selected those that were most similar to the expected u, v, e_x and e_y molecular orbitals, to form the minimal active space for CASSCF CAS(5,4) calculations. To expand the active space, we searched for orbitals in the inactive and virtual spaces with the largest contribution to the defect region, as determined by the total weight of the $2s$ and $2p$ atomic basis orbitals from the nearest four C atoms. For the CAS(7,7) calculation, we included two degenerate orbitals from the virtual space that transformed under the E IRRep (e'_x, e'_y), and one v-like from the inactive space, labeled v''. For CAS(11,11), we included two more orbitals from the virtual space (u', v') and two more from the inactive space (e''_x, e''_y). The shapes of these orbitals for the CAS(11,11) on the 190-atom cluster are presented in the Fig.4.2. By making the initial orbitals symmetric and using the SUPERSYMMETRY keyword to prevent transformations between orbitals of different IRReps during the CASSCF optimizations, we ensured that the C_{3v} symmetry of the system was preserved.

To ensure convergence for a calculation of several excited states, a state-averaged scheme is used for energy minimization. In case of the minimal active space spanned by the four carbon dangling-bond orbitals with five electrons in them, there are 4 possible quartet and 24 possible doublet configurations. Therefore, the quartet calculations are averaged over 4

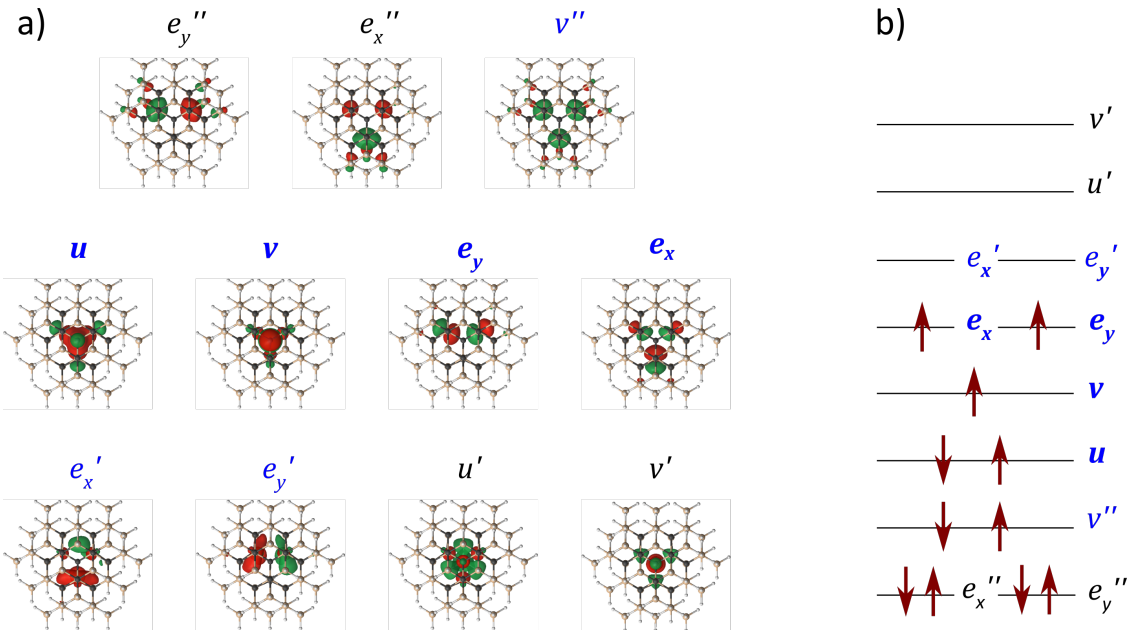

Figure 4.2: a) Molecular orbitals chosen to construct active spaces for CASSCF calculations on the 190-atom cluster. The four orbitals with labels in a bold blue font (u, v, e_x, e_y) arise mostly from the linear combination of the four dangling bonds from the vacancy's nearest-neighbor carbons. These orbitals must be included into any active space for a CASSCF calculation of the defect. In addition to these, four orbitals form the virtual space (e_x', e_y', u', v') and three from inactive space (e_x'', e_y'', v'') were chosen to expand the active space. Orbitals with blue-font labels were included in both CAS(7, 7) and CAS(11, 11), while those with black font were only in CAS(11, 11). For the 100-atom calculations, the chosen orbitals were similar to these in shape. Orbitals were visualized using the **LUSCUS** code [174]. b) Nominal distribution of electrons in these orbitals in the ground state of a ROHF calculation.

lowest states (even for larger active spaces). The doublet calculations are averaged over 8 lowest states, which includes the configurations whose energies are comparable to the quartet states, while not making the computations too time-consuming and not breaking the C_{3v} symmetry of the wavefunction (i.e., any doubly-degenerate pairs of ^2E states are wholly included into the state-averaging procedure).

4.4.2 CASPT2

Finally, CASPT2 [175, 176] calculations were performed based on the CASSCF results. Within the CASPT2 method, the interaction energy between the CASSCF configurations and the configurations involving excitations outside of the active space is estimated perturbatively. To limit the complexity of the CASPT2 calculations certain occupied orbitals can be designated "frozen", i.e. the configurations that would involve excitations from these orbitals would be not accounted for. In this work, we used the option AFREEZE = 0.001 for the four C atoms nearest-neighboring to the Si vacancy, which ensures that orbitals with less than 0.001 weight coming from these C atoms are frozen. This was done to ensure that surface orbitals do not contribute to the properties of the defect.

4.5 Results and Discussions

4.5.1 CASSCF calculations

Figure 4.3 provides a schematic representation for the calculated quartet and doublet energy levels of the V_{Si}^- center. The configurations and excitation energies are given for both CAS(7,7) and CAS(11,11) calculations on both clusters. As evident from the figure, the 190-atom cluster produces very similar results to those of the 100-atom cluster. The only

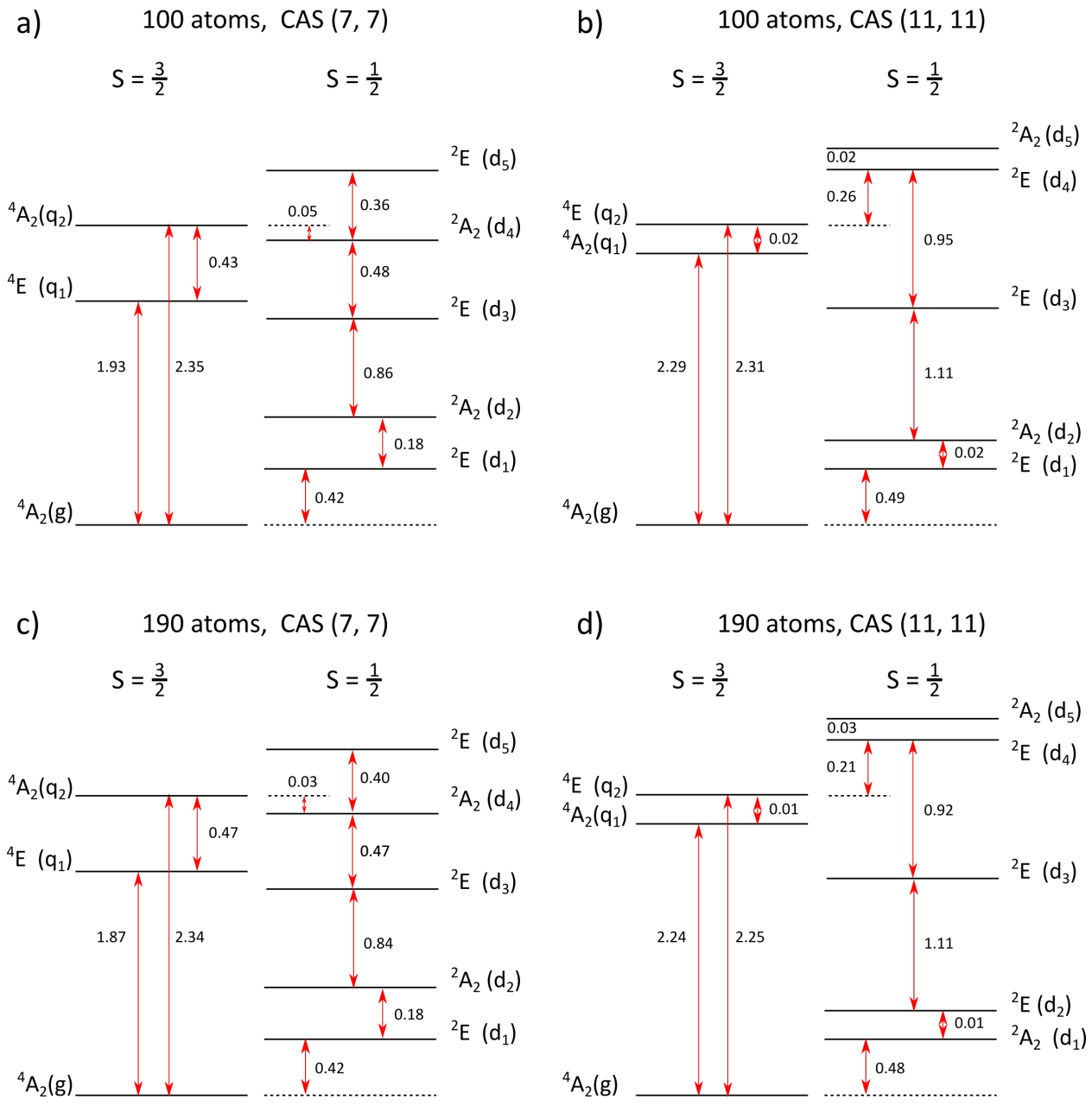

Figure 4.3: Schematic representation of quartet and doublet energy levels, for the 100-atom (a,b) and 190-atom (c,d) clusters, and for the (7,7) (a,c) and (11,11) (b,d) active spaces. The choice of active space in this case affects the results more significantly.

notable difference is the ordering of the lowest doublet states in CAS(11,11) calculations, which can be attributed to the small energy difference (0.02 eV) in these states. In all other cases, the 190-cluster-based energy levels differ from those based on 100-atom cluster no more than by 0.06 eV. Therefore, henceforth, we discuss the results for the 190-atom cluster only.

One of the biggest differences between the results from the two active spaces ((7,7) and (11,11)) is the ordering of the quartet excited states. For the CAS(7,7) calculation, the first excited quartet states are degenerate ^4E levels, which are 1.87 eV above the ground state, with another $^4A_2$ state which is 0.47 eV above the ^4E states. In the CAS(11,11) calculation, however, the first excited state is $^4A_2$ (2.24 eV above the ground state), and ^4E are 0.01 eV higher. Notice that the separation between ^4E and $^4A_2$ is also much smaller in CAS(11,11) than it is in CAS(7,7). Another difference is the ordering of the excited doublet states: CAS(7,7) predicts that the lowest-energy doublet states have E character and are located 0.42 eV above the quartet ground state, followed by a A_2 doublet level positioned 0.18 eV higher than the E states. In contrast, CAS(11,11) predicts that the lowest doublet state has A_2, character, and is 0.48 eV above the ground state, with other ^2E states at 0.01 eV above the A_2 state. Notice that the separation between these two states is again much smaller in CAS(11,11) than in CAS(7,7). Finally, CAS(7,7) predicts that the third excited doublet state (or group of states) is $^2A_2$, just 0.03 eV below the highest quartet state $^4A_2$, while in CAS(11,11) it is a ^2E state at 0.21 eV higher than ^4E.

These calculations for quartet excitation energies are compared to the experimental result for [158] and a set of previously-published DFT [155, 157], time-dependent DFT [154], and configuration interaction random-phase approximation [156] calculations on the defect, as presented in Fig.4.4. Note that the experiment and the majority of theoretical studies mentioned here only report the first-excited quartet energy. Specifically, the experimental

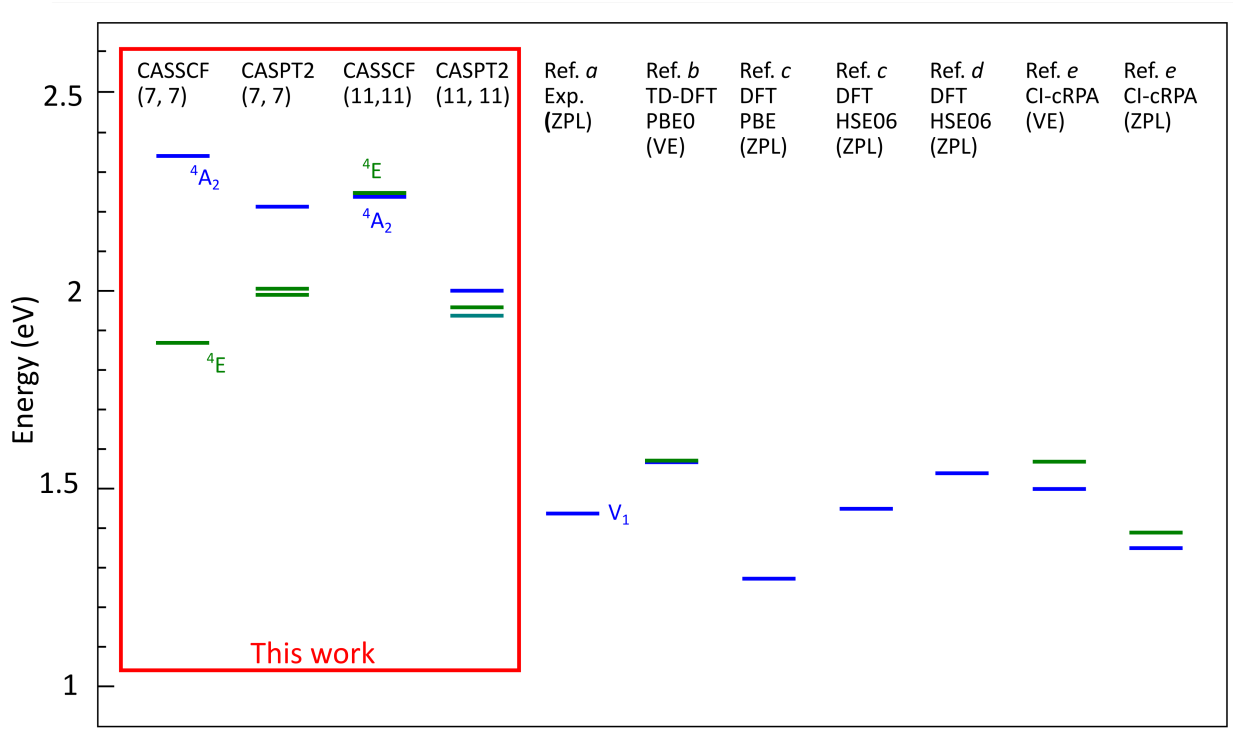

Figure 4.4: Quartet excitation energies for the V_{Si}^- predicted by our calculations, compared to the experimental result and previously-published estimates. Blue horizontal lines represent the $^4A_2$ excited state, while green lines represent pairs of ^4E states. (For CASPT2, the blue and green levels denote the levels that are closest by composition to $^4A_2$ and ^4E states in the underlying CASSCF calculation.) "ZPL" and "VE" denote the zero-phonon line, and the vertical excitation energy, respectively. The experimental result and the previously-published theoretical estimates were taken from the following references: *a*: [158], *b*: [154], *c*: [155], *d*: [157], and *i*: [156]

.

work [158] reported the photoluminescence spectrum for 4H-SiC, featuring two zero-phonon lines in the near-infrared region, at 1.438 eV and 1.352 eV, labeled as V_1 and V_2 respectively. These lines were originally identified as excitations of V_{Si}^- centers located at k- (for V_1) or h- (for V_2) sites [177]. However, a recent study [157] found that the h-site corresponds instead to V_1, and k-site to V_2. In Fig. 4.4, we follow the latter prescription. The first excitation energy from our CASSCF calculations (2.2 - 2.3 eV) appears to be significantly overestimated compared to the experimental value of 1.438 eV and the previous theoretical results (1.2 - 1.5 eV) [154, 155, 156, 157]. Note that the experiment reports the zero-phonon line (ZPL) that accounts for the geometry relaxation for the excited states. Since the geometry of our clusters was initially optimized just for the ground-state using DFT, and then kept fixed for the CASSCF calculations, the theoretical excitation energies that we report in this work correspond to vertical excitations (VE) which are expected to be slightly higher than the ZPL values.

Regarding the ordering of the quartet states, it was consistently observed in the previous DFT-based studies [3, 155] that the ^2E doublet lies closely above the $^2A_2$ state. In the TD-DFT calculation [154], the difference between these energy levels was only 4 meV. This picture is consistent with the level ordering of quartet states in the CAS(11, 11) calculation, but not with the CAS(7,7) calculation. For the doublet excited states, we have not found any experimental studies for their relative energies or ordering. However, Soykal et al. [3], using arguments from group theory and qualitative estimation of Coulomb interaction terms between orbitals, argues that the lowest-energy doublet state should be ^2E. This does not agree with the picture obtained by our CAS(11,11) calculation, in which the lowest doublet state has A_2 character. However, considering that the energy separation between this state is small, such as 0.01 eV, it is possible that this discrepancy would go away if a larger passivated cluster were used.

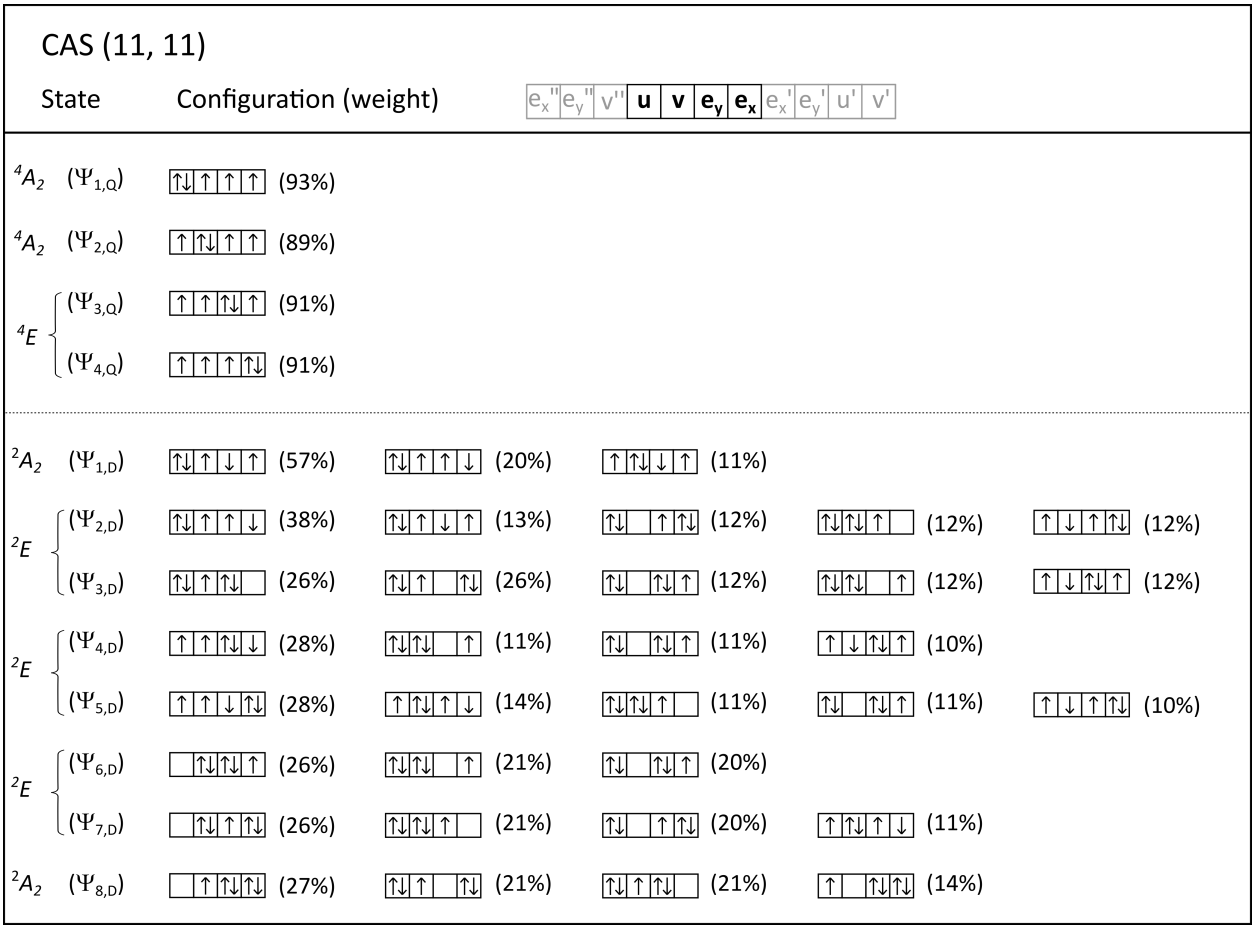

Figure 4.5: Configurations in the quartet and doublet states of the CAS(11, 11) calculation on the defect in the 190-atom cluster. Only configurations with total weights larger than 10% are shown here. Although the active space contains 11 orbitals in total, configurations with weights larger than 10% only involve excitations within the u, v, e_x, e_y orbital group. Therefore, each configuration is represented by the occupations of these orbitals only (boxes are orbitals, and $\uparrow$ and $\downarrow$ represent spin-up and spin-down electrons) .

Now, let us discuss the wavefunction composition predicted by the CASSCF calculations, starting with the CAS(11,11) case, as shown in Fig. 4.5. For the ground state, this configuration represents the expected orbital population picture following Hund's rules (assuming v and $e_{x,y}$ orbitals are very close in energy): the u level is doubly-occupied, and v, e_x, e_y have single occupancy, which creates spin 3/2. Each of the quartet's excited states represents one (spin-down) electron being excited from the u-level to the higher-lying v and e levels.

The doublet configurations for CAS(11,11) are less trivial. Each state has at least three configurations with more than 10% contribution to the total weight. The lowest doublet level is dominated by 2UDU configuration, but also has a sizeable contribution from 2UUD and U2DU configurations. (Here the letter "U" or "D" is used for occupancy of a spin-up or spin-down electron in an orbital, respectively. For a doubly-occupied or empty orbital, "2" or "0" is used, respectively.) The next ^2E state contains similar configurations, only differing in the occupation patterns of the e_x and e_y orbitals. All of these results support the observation that the doublet states have a strongly multiconfigurational character, and therefore are difficult to calculate using single-configuration methods such as DFT or Hartree-Fock.

Now, for the CAS(7,7) configuration, there are several important differences. First, the ground state is no longer dominated by one configuration. Instead, it is composed of about 75% contribution by weight from 2UUU (which is the expected configuration for the ground state), and 25% of U2UU, with the doubly-occupied v-orbital. The highest quartet state has the reversed ratios: 25% comes from 2UUU and 75% is from U2UU.

4.5.2 CASPT2 calculations

Let us now consider the effects of applying CASPT2 based on the solutions obtained in CAS(11,11) and in CAS(7,7). The quartet states obtained using CASPT2 are shown in the

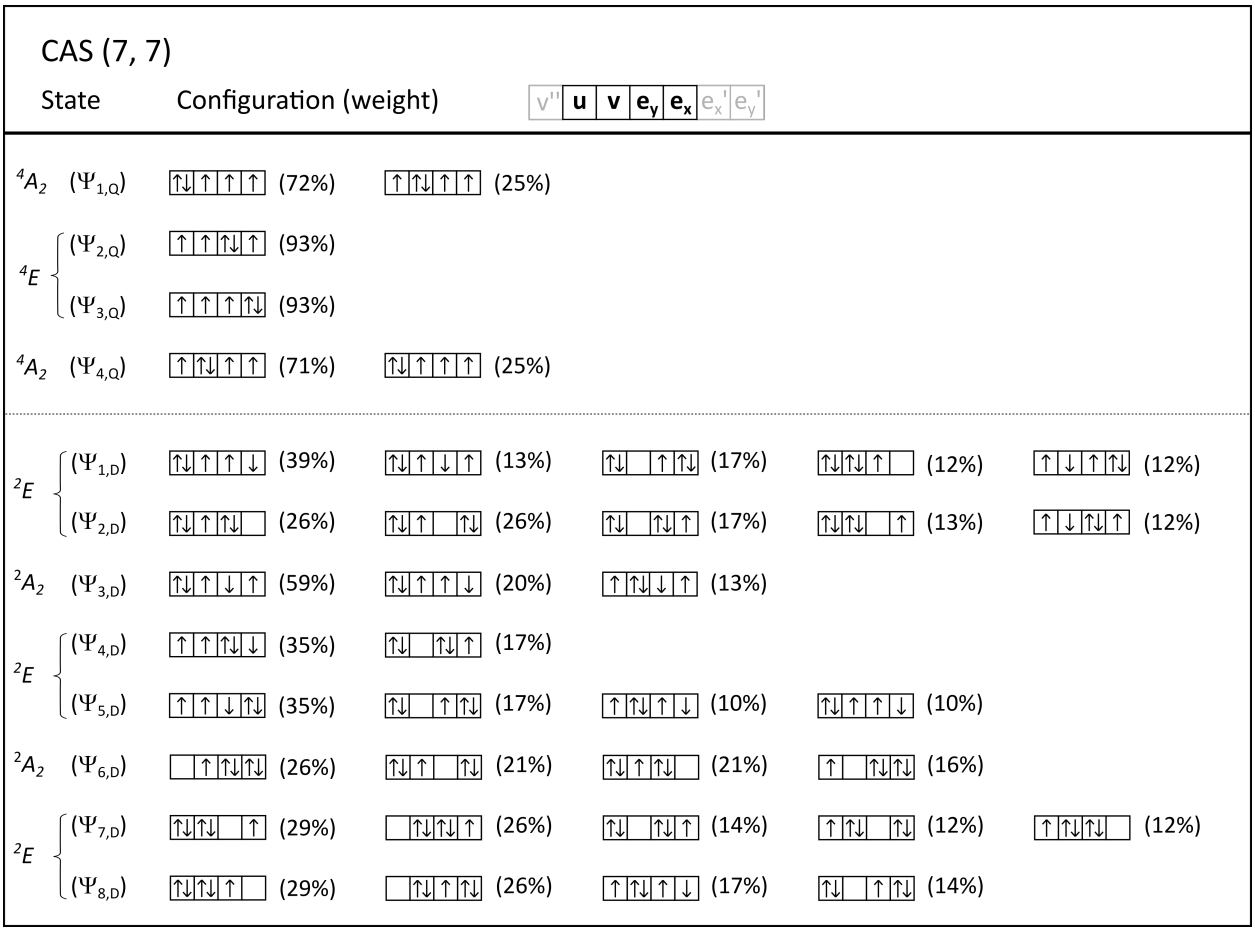

Figure 4.6: Configurations in the quartet and doublet states of the CAS(7, 7) calculation on the defect in the 190-atom cluster. Only configurations with total weights larger than 10% are shown here. Although the active space contains 7 orbitals in total, configurations with weights larger than 10% only involve excitations within the u, v, e_x, e_y orbitals. Therefore, each configuration is represented by the occupations of the orbitals (boxes are orbitals, and $\uparrow$ and $\downarrow$ represent spin-up and spin-down electrons)

Fig.4.4. First, for CAS(11,11) we observe that the energy of the first excited state has been reduced to 1.9 eV (from 2.2 eV), while for CAS(7,7) it increased by 0.12 eV. The 100-atom result has a slightly lower first excitation energy (1.88 eV vs 1.94 eV for 190-atom cluster), although its CASSCF-only estimate was a bit higher.

The structure of the CASPT2 states can be analyzed from their CI-coefficient expansions. Figure 4.7 shows the wavefunction composition of the CASPT2 eigenstates (based on the CAS(11,11) calculation) for the 190-atom cluster. Note that these states do not exactly coincide with those of the unperturbed CASSCF calculation, although most of them can be associated mostly with one of the CASSCF states (with the exception of the three lowest doublets, which appear to be mixtures of the lowest $^2A_2$ and ^2E doublet states from CASSCF). Furthermore, since in the OPENMOLCAS code there is no option to restrict the symmetry in CASPT2 calculations similar to **SUPERSYMMETRY** for CASSCF, the degeneracies of all orbitals have been slightly broken. Considering these, CASPT2 predicts a different order for the ^4E- and $^4A_2$- like states in quartet excitations than CASSCF CAS(11,11). In CAS(7, 7), the CASPT2-calculated ^4E state also has a lower energy than the $^4A_2$ state, which is now consistent with the CASSCF (7,7) calculation.

As shown in Fig. 4.4, for the CAS(11,11), the ^4E - like states lie about 0.04 eV below the $^4A_2$ state, while in CASSCF ^4E states are 0.02 eV above the $^4A_2$ state. The energy splitting between the two ^4E-like states in CASPT2 is about 0.02 eV. In both CASSCF(7,7) and CASPT2(7,7) the doubly-degenerate ^4E state has a lower energy than the $^4A_2$ state (by 0.47 eV in CASSCF, 0.21 eV in CASPT2). The degeneracy of the ^4E level is split by 0.02 eV.

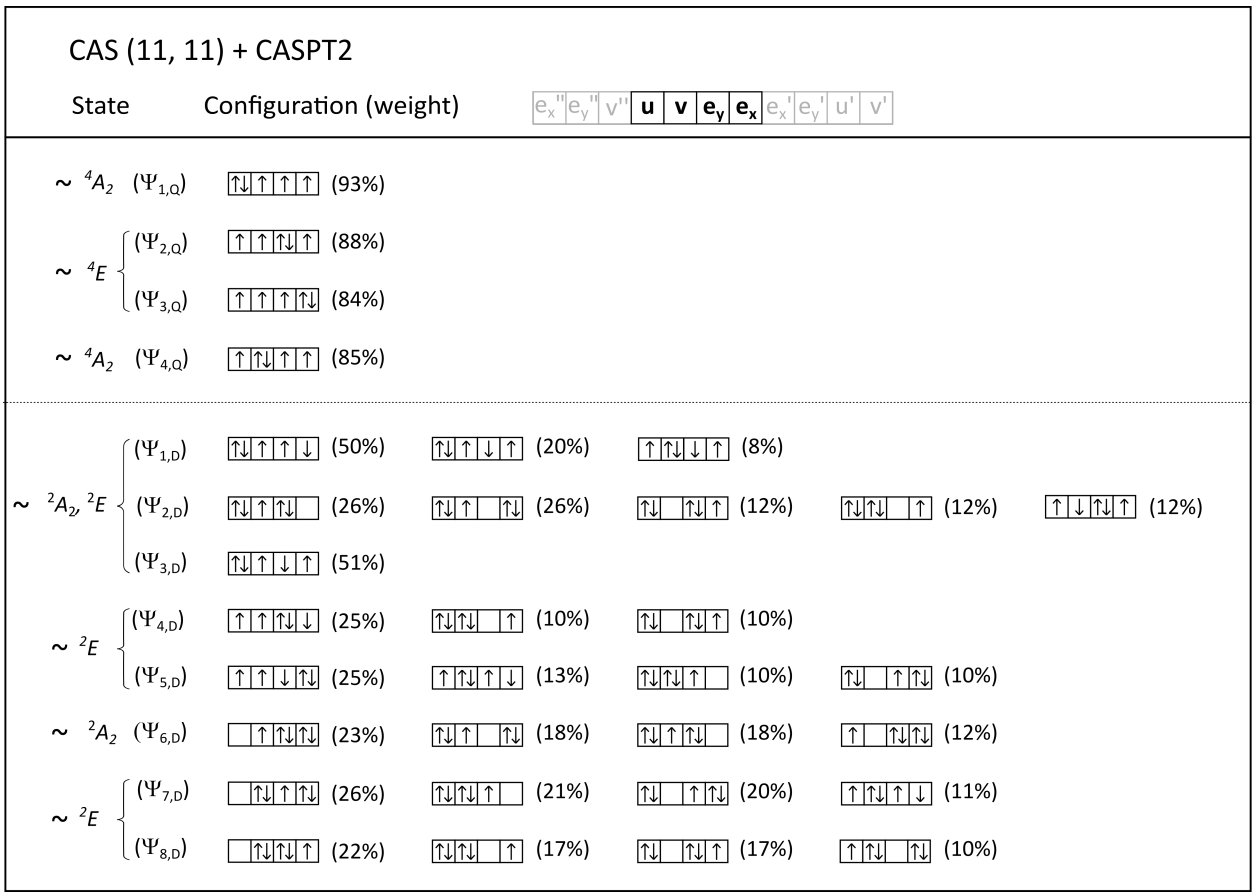

Figure 4.7: Structure of the CASPT2 states, computed based on the preliminary CASSCF (CAS(11, 11)) calculation performed on the 190-atom cluster. Each of the new eigenfunctions, in general, is a linear combination of the original CASSCF states, but in most cases can be identified with mostly one original state based on the similarity of the CI coefficients. This identification here is denoted by ${}^nE$ or ${}^nA_2$ (n = 4 or 2). This is except for the lowest three doublet states ($\Psi_{1-3,D}$), which together are some mixtures of the lowest ${}^2E$ and ${}^2A_2$ states of CAS(11,11).

4.6 Summary

In this work, we performed multireference quantum-chemistry calculations on the h-site charged Si vacancy in 4H-SiC, using passivated molecular clusters. The lowest excitation energies in our CASPT2 results are overestimated by at least 0.5 eV compared to the reported experimental value [158] Some part of this is related by the fact that we report the vertical excitation energies, while the experiment provides only the ZPL, which is expected to be lower. However, the computed vertical excitations from TD-DFT [154] and ci-RPA [156] overestimate the experimental value by 0.22eV and 0.15 eV, correspondingly.

One of the potential reasons for this discrepancy is related to the limitations of the finite-cluster models. While methods like Kohn-Sham DFT can be formulated to calculate electronic levels in solid systems, with periodic boundary conditions and plane-wave basis sets, most implementations of multiconfigurational methods like CASSCF or CAPST2 can only work with finite-electron systems, and thus are limited to calculations of moderately-sized molecules and clusters. Using a large-enough passivated cluster can sometimes work for defects in large-bandgap systems, especially if the lowest excitations only involve electrons moving between orbitals located within the bandgap [167]. In the case of V_{Si}^{-} in 4H-SiC, however, the lowest excitation involves an electron from the u orbital, whose energy lies within the valence band of the SiC crystal. Therefore, it might be crucial to accurately calculate the crystalline electron states and their effect on with the defect orbitals to obtain a decent estimate for the excited states of the defect. Increasing the size of the molecular SiC cluster would not significantly lower the excitation energies unless several tens of thousand atoms are included, which is too computationally expensive to be treated within multireference methods.

One of the potential ways to resolve this issue would be to use one of the quantum embedding

algorithms [178], which allow treating a small portion of the extended system, such as the defect and its surroundings within a crystal, with a high-level theory (e.g. CASSCF, CASPT2 etc.), while modeling the effect of rest of the system with an effective Hamiltonian, as has been successfully demonstrated for the NV-center in diamond [179]. This could be a good direction for further work in the multireference treatment of the silicon vacancy in SiC.

Chapter 5

Conclusions

The goal of the work presented in this thesis is to assess and report the applicability and performance of several electronic-structure computational methods that attempt to account for the electron correlation effects more accurately than can be done with standard DFT schemes. One of the methods (FLOSIC) involves a modification to the DFT method, to correct for the nonphysical electron self-interaction which occurs due to the approximate nature of the exchange-correlation functional. Other methods, such as CASSCF and CASPT2, model the electron wavefunction with more than one Slater determinant or account for the correlation effects perturbatively.

In Chapter 2, we applied the FLOSIC-DFT method to study the electronic properties of two charge states of a Cu-based molecule. It was observed that FLOSIC-DFT predicts the spin-density distribution among the Cu atom and the four nearest S atoms that is consistent with multiconfigurational studies, but it is reversed to that predicted by the standard (SIC-free) DFT methods. However, the composition of the HOMO is changed in the FLOSIC calculation since the $3d$-electron orbital energies are decreased more significantly. The validity of the FLOSIC-calculated HOMO composition can be addressed in future work.

In Chapter 3, we applied the FLOSIC-DFT method to the computation of hyperfine coupling parameters for a set atoms and molecules. We tested several approaches to generate the starting FOD sets for each system, and confirmed that the default basis sets for the FLOSIC calculation contain sufficiently narrow Gaussian functions for calculation of hyperfine pa-

rameters. For sufficiently light atoms ($Z \leq 25$), the FLOSIC-based predictions for the Fermi contact (FC) term agree with experiment significantly better than the predictions based on SIC-free DFT. The FLOSIC-based FC terms are also closer to the experimental values for transition-metal based molecules, and are comparable to the standard-DFT predictions for molecules without transition-metal elements.

In Chapter 4, we applied multireference quantum-chemistry methods (CASSCF and CASPT2) to analyze the electronic properties of a silicon vacancy defect in 4H polytype of silicon carbide. We constructed several hydrogen-passivated clusters of SiC containing the defect and performed the calculations with several sizes of the active space. Our results overestimate the first excitation energy of the defect by about 0.5-0.9 eV, and predict a different ordering of quartet states than has been proposed in the previous studies on the defect. This demonstrates that for some point defects in semiconductors, in which excited states are involved with levels below the top of the valence band or above the bottom of the conduction band, CASSCF and CASPT2 with hydrogen-passivated cluster may not be the best models for treating the static correlation effects, potentially because they do not model the environment of the defect sufficiently well.

The work presented in this dissertation has improved our understanding of the electronic correlation effects and the performance of several computational methods that attempt to calculate them. This knowledge can be used for the development of more advanced computational methods, which would allow us to compute the physical and chemical properties of materials more accurately and efficiently. This will contribute to further advances in the fields of quantum information science, drug and material discovery, development of alternative sources of energy, and other areas of scientific and technological progress.

Bibliography

[1] A. Karanovich, Y. Yamamoto, K. A. Jackson, and K. Park, J. Chem. Phys. **155**, 014106 (2021).

[2] A. Karanovich, K. A. Jackson, and K. Park, J. Chem. Phys. **161**, 014102 (2024).

[3] Ö. Soykal, P. Dev, and S. E. Economou, Phys. Rev. B **93**, 081207 (2016).

[4] E. Schrödinger, Phys. Rev. **28**, 1049 (1926).

[5] M. Born and J. R. Oppenheimer, Ann. Phys. **389**, 457 (1927).

[6] D. R. Hartree, Math. Proc. Camb. Philos. Soc. **24**, 89 (1928).

[7] D. R. Hartree, Math. Proc. Camb. Philos. Soc. **24**, 111 (1928).

[8] R. Arnowitt and S. Deser, J. Math. Phys. **3**, 637 (1962).

[9] J. C. Slater, Phys. Rev. **34**, 1293 (1929).

[10] V. Fock, Z. Phys. **61**, 126 (1930).

[11] D. R. Hartree and W. Hartree, Proc. R. Soc. Lond. A **150**, 9 (1935).

[12] A. Szabo and N. S. Ostlund, *Modern Quantum Chemistry: Introduction to Advanced Electronic Structure Theory* (Courier Corporation, 1996).

[13] B. O. Roos, R. Lindh, P.-Å. Malmqvist, V. Veryazov, and P.-O. Widmark, *Multiconfigurational Quantum Chemistry* (John Wiley & Sons, 2016).

[14] B. O. Roos, P. R. Taylor, and P. E. Sigbahn, Chem. Phys. **48**, 157 (1980).

[15] P. Siegbahn, A. Heiberg, B. Roos, and B. Levy, Phys. Scr. **21**, 323 (1980).

[16] P. E. Siegbahn, J. Almlöf, A. Heiberg, and B. O. Roos, J. Chem. Phys. **74**, 2384 (1981).

[17] P. Hohenberg and W. Kohn, Phys. Rev. **136**, B864 (1964).

[18] M. Levy, Proc. Natl. Acad. Sci. U.S.A. **76**, 6062 (1979).

[19] W. Kohn and L. J. Sham, Phys. Rev. **140**, A1133 (1965).

[20] J. P. Perdew and Y. Wang, Phys. Rev. B **45**, 13244 (1992).

[21] S. H. Vosko, L. Wilk, and M. Nusair, Can. J. Phys. **58**, 1200 (1980).

[22] J. P. Perdew, J. A. Chevary, S. H. Vosko, K. A. Jackson, M. R. Pederson, D. J. Singh, and C. Fiolhais, Phys. Rev. B **46**, 6671 (1992).

[23] J. P. Perdew, K. Burke, and M. Ernzerhof, Phys. Rev. Lett. **77**, 3865 (1996).

[24] R. A. Heaton, J. G. Harrison, and C. C. Lin, Phys. Rev. B **28**, 5992 (1983).

[25] J. P. Perdew, Int. J. Quantum Chem. **28**, 497 (1985).

[26] S. Patchkovskii and T. Ziegler, J. Chem. Phys. **116**, 7806 (2002).

[27] E. Ruiz, S. Alvarez, J. Cano, and V. Polo, J. Chem. Phys. **123**, 164110 (2005).

[28] J. P. Perdew and A. Zunger, Phys. Rev. B **23**, 5048 (1981).

[29] M. R. Pederson, R. A. Heaton, and C. C. Lin, J. Chem. Phys. **80**, 1972 (1984).

[30] M. R. Pederson, R. A. Heaton, and C. C. Lin, J. Chem. Phys. **82**, 2688 (1985).

[31] M. R. Pederson, A. Ruzsinszky, and J. P. Perdew, J. Chem. Phys. **140**, 121103 (2014).

[32] P.-O. Löwdin, J. Chem. Phys. **18**, 365 (1950).

[33] Z.-h. Yang, M. R. Pederson, and J. P. Perdew, Phys. Rev. A **95**, 052505 (2017).

[34] D.-y. Kao, K. Withanage, T. Hahn, J. Batool, J. Kortus, and K. Jackson, J. Chem. Phys. **147**, 164107 (2017).

[35] V. I. Anisimov, F. Aryasetiawan, and A. I. Lichtenstein, J. Phys. Condens. Matter **9**, 767 (1997).

[36] H. J. Kulik, M. Cococcioni, D. A. Scherlis, and N. Marzari, Phys. Rev. Lett. **97**, 103001 (2006).

[37] M. R. Pederson, J. Chem. Phys. **142**, 064112 (2015).

[38] M. R. Pederson, T. Baruah, D.-y. Kao, and L. Basurto, J. Chem. Phys. **144**, 164117 (2016).

[39] S. Adhikari, B. Santra, S. Ruan, P. Bhattarai, N. K. Nepal, K. A. Jackson, and A. Ruzsinszky, J. Chem. Phys. **153**, 184303 (2020).

[40] J. Vargas, P. Ufondu, T. Baruah, Y. Yamamoto, K. A. Jackson, and R. R. Zope, Phys. Chem. Chem. Phys. **22**, 3789 (2020).

[41] K. A. Jackson, J. E. Peralta, R. P. Joshi, K. P. Withanage, K. Trepte, K. Sharkas, and A. I. Johnson, J. Phys. Conf. Ser. **1290**, 012002 (2019).

[42] A. I. Johnson, K. P. K. Withanage, K. Sharkas, Y. Yamamoto, T. Baruah, R. R. Zope, J. E. Peralta, and K. A. Jackson, J. Chem. Phys. **151**, 174106 (2019).

[43] R. P. Joshi, K. Trepte, K. P. K. Withanage, K. Sharkas, Y. Yamamoto, L. Basurto, R. R. Zope, T. Baruah, K. A. Jackson, and J. E. Peralta, J. Chem. Phys. **149**, 164101 (2018).

[44] S. Schwalbe, T. Hahn, S. Liebing, K. Trepte, and J. Kortus, J. Comput. Chem. **39**, 2463 (2018).

[45] D.-y. Kao, M. R. Pederson, T. Hahn, T. Baruah, S. Liebing, and J. Kortus, Magnetochemistry **3**, 31 (2017).

[46] M. S. Fataftah, M. D. Krzyaniak, B. Vlaisavljevich, M. R. Wasielewski, J. M. Zadrozny, and D. E. Freedman, Chem. Sci. **10**, 6707 (2019).

[47] B. K. Maiti, L. B. Maia, K. Pal, B. Pakhira, T. Avilés, I. Moura, S. R. Pauleta, J. L. Nuñez, A. C. Rizzi, C. D. Brondino, S. Sarkar, and J. J. G. Moura, Inorg. Chem. **53**, 12799 (2014).

[48] K. Ray, T. Weyhermüller, F. Neese, and K. Wieghardt, Inorg. Chem. **44**, 5345 (2005).

[49] N. Robertson and L. Cronin, Coord. Chem. Rev. **227**, 93 (2002).

[50] M. R. Pederson and K. A. Jackson, Phys. Rev. B **41**, 7453 (1990).

[51] K. Jackson and M. R. Pederson, Phys. Rev. B **42**, 3276 (1990).

[52] M. R. Pederson, D. V. Porezag, J. Kortus, and D. C. Patton, Phys. Status Solidi B **217**, 197 (2000).

[53] R. R. Zope, T. Baruah, Y. Yamamoto, L. Basurto, C. M. Diaz, J. E. Peralta, and K. A. Jackson, FLOSIC 0.2, based on the NRLMOL code of M. R. Pederson, The code is available to download at https://github.com/FLOSIC/PublicRelease_2020.

[54] D. Porezag and M. R. Pederson, Phys. Rev. A **60**, 2840 (1999).

[55] S. Schwalbe, K. Trepte, L. Fiedler, A. I. Johnson, J. Kraus, T. Hahn, J. E. Peralta, K. A. Jackson, and J. Kortus, J. Comput. Chem. **40**, 2843 (2019).

[56] P. J. Hay and W. R. Wadt, J. Chem. Phys. **82**, 270 (1985).

[57] A. D. Becke, J. Chem. Phys. **98**, 5648 (1993).

[58] C. Lee, W. Yang, and R. G. Parr, Phys. Rev. B **37**, 785 (1988).

[59] P. J. Stephens, F. J. Devlin, C. F. Chabalowski, and M. J. Frisch, J. Phys. Chem. **98**, 11623 (1994).

[60] J.-L. Bredas, Mater. Horiz. **1**, 17 (2014).

[61] I. Rudra, Q. Wu, and T. Van Voorhis, J. Chem. Phys. **124**, 024103 (2006).

[62] S. Klüpfel, P. Klüpfel, and H. Jónsson, Phys. Rev. A **84**, 050501 (2011).

[63] S. Lehtola, M. Head-Gordon, and H. Jónsson, J. Chem. Theory Comput. **12**, 3195 (2016).

[64] S. Romero, Y. Yamamoto, T. Baruah, and R. R. Zope, Phys. Chem. Chem. Phys. **23**, 2406 (2021).

[65] F. Aquilante, J. Autschbach, R. K. Carlson, L. F. Chibotaru, M. G. Delcey, L. De Vico, I. Fdez. Galván, N. Ferré, L. M. Frutos, L. Gagliardi, M. Garavelli, A. Giussani, C. E. Hoyer, G. Li Manni, H. Lischka, D. Ma, P.-Å. Malmqvist, T. Müller, A. Nenov, M. Olivucci, T. B. Pedersen, D. Peng, F. Plasser, B. Pritchard, M. Reiher, I. Rivalta, I. Schapiro, J. Segarra-Martí, M. Stenrup, D. G. Truhlar, L. Ungur, A. Valentini, S. Vancoillie, V. Veryazov, V. P. Vysotskiy, O. Weingart, F. Zapata, and R. Lindh, J. Comput. Chem. **37**, 506 (2016).

[66] M. Douglas and N. M. Kroll, Ann. Phys. **82**, 89 (1974).

[67] B. A. Hess, Phys. Rev. A **33**, 3742 (1986).

[68] P.-O. Widmark, P.-Å. Malmqvist, and B. O. Roos, Theor. Chem. Acc. **77**, 291 (1990).

[69] B. O. Roos, R. Lindh, P.-Å. Malmqvist, V. Veryazov, and P.-O. Widmark, J. Phys. Chem. A **108**, 2851 (2004).

[70] I. Bertini, C. Luchinat, and G. Parigi, *Solution NMR of Paramagnetic Molecules* (Elsevier, Amsterdam, 2001).

[71] A. Abragam and B. Bleaney, *Electron Paramagnetic Resonance of Transition Ions* (Clarendon Press, Oxford, 1970).

[72] N. M. Atherton, *Principles of Electron Spin Resonance* (Ellis Horwood, New York, 1993).

[73] S. Thiele, F. Balestro, R. Ballou, S. Klyatskaya, M. Ruben, and W. Wernsdorfer, Science **344**, 1135 (2014).

[74] M. Atzori, A. Chiesa, E. Morra, M. Chiesa, L. Sorace, S. Carretta, and R. Sessoli, Chem. Sci. **9**, 6183 (2018).

[75] C. Godfrin, A. Ferhat, R. Ballou, S. Klyatskaya, M. Ruben, W. Wernsdorfer, and F. Balestro, Phys. Rev. Lett. **119**, 187702 (2017).

[76] A. Ruskuc, C.-J. Wu, J. Rochman, J. Choi, and A. Faraon, Nature **602**, 408 (2022).

[77] C.-J. Yu, S. von Kugelgen, D. W. Laorenza, and D. E. Freedman, ACS Cent. Sci. **7**, 712 (2021).

[78] M. Munzarová and M. Kaupp, J. Phys. Chem. A **103**, 9966 (1999).

[79] M. L. Munzarová, P. Kubáček, and M. Kaupp, J. Am. Chem. Soc. **122**, 11900 (2000).

[80] S. Kossmann, B. Kirchner, and F. Neese, Mol. Phys. **105**, 2049 (2007).

[81] D. A. Pantazis, Magnetochemistry **5**, 69 (2019).

[82] S. Ghassemi Tabrizi, A. V. Arbuznikov, C. A. Jiménez-Hoyos, and M. Kaupp, J. Chem. Theory Comput. **16**, 6222 (2020).

[83] S. A. Perera, J. D. Watts, and R. J. Bartlett, J. Chem. Phys. **100**, 1425 (1994).

[84] K. Sharkas, B. Pritchard, and J. Autschbach, J. Chem. Theory Comput. **11**, 538 (2015).

[85] T. Shiozaki and T. Yanai, J. Chem. Theory Comput. **12**, 4347 (2016).

[86] P. K. Samanta and A. Köhn, J. Chem. Phys. **149**, 064101 (2018).

[87] A. L. Wysocki and K. Park, Inorg. Chem. **59**, 2771 (2020).

[88] R. Feng, T. J. Duignan, and J. Autschbach, J. Chem. Theory Comput. **17**, 255 (2021).

[89] A. L. Wysocki and K. Park, J. Chem. Phys. **160**, 224102 (2024).

[90] A. D. Becke, Phys. Rev. A **38**, 3098 (1988).

[91] J. P. Perdew, Phys. Rev. B **33**, 8822 (1986).

[92] J. Sun, A. Ruzsinszky, and J. P. Perdew, Phys. Rev. Lett. **115**, 036402 (2015).

[93] P. C. Redfern, P. Zapol, L. A. Curtiss, and K. Raghavachari, J. Phys. Chem. A **104**, 5850 (2000).

[94] S. F. Sousa, P. A. Fernandes, and M. J. Ramos, J. Phys. Chem. A **111**, 10439 (2007).

[95] S. Grimme, J. Phys. Chem. A **109**, 3067 (2005).

[96] J. Sun, R. C. Remsing, Y. Zhang, Z. Sun, A. Ruzsinszky, H. Peng, Z. Yang, A. Paul, U. Waghmare, X. Wu, M. L. Klein, and J. P. Perdew, Nat. Chem. **8**, 831 (2016).

[97] M. Ekholm, D. Gambino, H. J. M. Jönsson, F. Tasnádi, B. Alling, and I. A. Abrikosov, Phys. Rev. B **98**, 094413 (2018).

[98] D. A. Pantazis, Inorganics **7** (2019).

[99] W. J. Childs and T. C. Steimle, J. Chem. Phys. **88**, 6168 (1988).

[100] T. C. De Vore and W. Weltner, J. Am. Chem. Soc. **99**, 4700 (1977).

[101] R. F. Ferrante, J. L. Wilkerson, W. R. M. Graham, and W. Weltner, J. Chem. Phys. **67**, 5904 (1977).

[102] M. R. Pederson, K. P. K. Withanage, Z. Hooshmand, A. I. Johnson, T. Baruah, Y. Yamamoto, R. R. Zope, D.-Y. Kao, P. B. Shukla, J. K. Johnson, J. E. Peralta, and K. A. Jackson, J. Chem. Phys. **159**, 154112 (2023).

[103] C. M. Diaz, L. Basurto, S. Adhikari, Y. Yamamoto, A. Ruzsinszky, T. Baruah, and R. R. Zope, J. Chem. Phys. **155**, 064109 (2021).

[104] C. G. Van de Walle and P. E. Blöchl, Phys. Rev. B **47**, 4244 (1993).

[105] C. M. Diaz, L. Basurto, Y. Yamamoto, T. Baruah, and R. R. Zope, UTEP-NRLMOL code, https://quantum.utep.edu/?q=nrlmol.

[106] E. D. Glendening, J. K. Badenhoop, A. E. Reed, J. E. Carpenter, J. Bohmann, C. M. Morales, P. Karafiloglou, C. R. Landis, and F. Weinhold, *NBO 7.0*, Theoretical Chemistry Institute, University of Wisconsin, Madison, WI (2018).

[107] W. Zou, D. Nori-Shargh, and J. E. Boggs, J. Phys. Chem. A **117**, 207 (2013).

[108] E. D. Glendening and F. Weinhold, J. Comput. Chem. **19**, 593 (1998).

[109] E. D. Glendening and F. Weinhold, J. Comput. Chem. **19**, 610 (1998).

[110] E. D. Glendening, J. K. Badenhoop, and F. Weinhold, J. Comput. Chem. **19**, 628 (1998).

[111] T. Helgaker, M. Jaszuński, and K. Ruud, Chem. Rev. **99**, 293 (1999).

[112] J. W. Linnett, Nature **187**, 859 (1960).

[113] J. W. Linnett, J. Am. Chem. Soc. **83**, 2643–2653 (1961).

[114] J. W. Linnett, *Electronic Structure of Molecules* (Methuen & Co. Ltd., London, 1964).

[115] P. H. Kasai, Phys. Rev. Lett. **21**, 67 (1968).

[116] S. N. Foner, E. L. Cochran, V. A. Bowers, and C. K. Jen, J. Chem. Phys. **32**, 963 (1960).

[117] C. K. Ien, V. A. Bowers, E. L. Cochran, and S. N. Foner, Phys. Rev. **126**, 1749 (1962).

[118] W. M. Itano and D. J. Wineland, Phys. Rev. A **24**, 1364 (1981).

[119] F. Arbes, M. Benzing, T. Gudjons, F. Kurth, and G. Werth, Z. Phys. D **31**, 27 (1994).

[120] P. H. Kasai, Acc. Chem. Res. **4**, 329 (1971).

[121] P. H. Kasai and D. McLeod, J. Chem. Phys. **55**, 1566 (1971).

[122] A. Abragam, J. Horowitz, M. H. L. Pryce, and K. W. Morton, Proc. R. Soc. Lond. A Math. Phys. Sci **230**, 169 (1955).

[123] R. E. Watson and A. J. Freeman, Phys. Rev. **123**, 2027 (1961).

[124] R. W. Fessenden, J. Phys. Chem. **71**, 74 (1967).

[125] E. L. Cochran, F. J. Adrian, and V. A. Bowers, J. Chem. Phys. **44**, 4626 (1966).

[126] L. B. Knight and J. Steadman, J. Chem. Phys. **80**, 1018 (1984).

[127] L. Hermosilla, P. Calle, J. M. Garcí'a de la Vega, and C. Sieiro, J. Phys. Chem. A **109**, 1114 (2005).

[128] R. J. Van Zee, R. F. Ferrante, and W. Weltner, J. Chem. Phys. **83**, 6181 (1985).

[129] C. A. McDowell, H. Nakajima, and P. Raghunathan, Can. J. Chem. **48**, 805 (1970).

[130] T. C. DeVore, R. J. Van Zee, and W. Weltner, J. Chem. Phys. **68**, 3522 (1978).

[131] K.-i. Namiki and S. Saito, J. Chem. Phys. **107**, 8848 (1997).

[132] S. K. Smoukov, J. Telser, B. A. Bernat, C. L. Rife, R. N. Armstrong, and B. M. Hoffman, J. Am. Chem. Soc. **124**, 2318 (2002).

[133] E. Togan, Y. Chu, A. Imamoglu, and M. Lukin, Nature **478**, 497 (2011).

[134] H. Bernien, B. Hensen, W. Pfaff, G. Koolstra, M. S. Blok, L. Robledo, T. H. Taminiau, M. Markham, D. J. Twitchen, L. Childress, and R. Hanson, Nature **497**, 86 (2013).

[135] M. S. Grinolds, S. Hong, P. Maletinsky, L. Luan, M. D. Lukin, R. L. Walsworth, and A. Yacoby, Nat. Phys. **9**, 215 (2013).

[136] B. Hensen, H. Bernien, A. E. Dréau, A. Reiserer, N. Kalb, M. S. Blok, J. Ruitenberg, R. F. Vermeulen, R. N. Schouten, C. Abellán, W. Amaya, V. Pruneri, M. W. Mitchell, M. Markham, D. J. Twitchen, D. Elkouss, S. Wehner, T. H. Taminiau, and R. Hanson, Nature **526**, 682 (2015).

[137] J. R. Maze, P. L. Stanwix, J. S. Hodges, S. Hong, J. M. Taylor, P. Cappellaro, L. Jiang, M. G. Dutt, E. Togan, A. S. Zibrov, A. Yacoby, R. L. Walsworth, and M. D. Lukin, Nature **455**, 644 (2008).

[138] G. Balasubramanian, I. Y. Chan, R. Kolesov, M. Al-Hmoud, J. Tisler, C. Shin, C. Kim, A. Wojcik, P. R. Hemmer, A. Krueger, T. Hanke, A. Leitenstorfer, R. Bratschitsch, F. Jelezko, and J. Wrachtrup, Nature **455**, 648 (2008).

[139] T. Häberle, D. Schmid-Lorch, K. Karrai, F. Reinhard, and J. Wrachtrup, Phys. Rev. Lett. **111**, 170801 (2013).

[140] D. Riedel, F. Fuchs, H. Kraus, S. Väth, A. Sperlich, V. Dyakonov, A. A. Soltamova, P. G. Baranov, V. A. Ilyin, and G. V. Astakhov, Phys. Rev. Lett. **109**, 226402 (2012).

[141] H. Kraus, V. A. Soltamov, F. Fuchs, D. Simin, A. Sperlich, P. G. Baranov, G. V. Astakhov, and V. Dyakonov, Sci. Rep. **4**, 5303 (2014).

[142] M. Widmann, S.-Y. Lee, T. Rendler, N. T. Son, H. Fedder, S. Paik, L.-P. Yang, N. Zhao, S. Yang, I. Booker, A. Denisenko, M. Jamali, S. A. Momenzadeh, I. Gerhardt, T. Ohshima, A. Gali, E. Janzén, and J. Wrachtrup, Nat. Mater. **14**, 164 (2015).

[143] A. N. Anisimov, D. Simin, V. A. Soltamov, S. P. Lebedev, P. G. Baranov, G. V. Astakhov, and V. Dyakonov, Sci. Rep. **6**, 33301 (2016).

[144] D. Simin, V. A. Soltamov, A. V. Poshakinskiy, A. N. Anisimov, R. A. Babunts, D. O. Tolmachev, E. N. Mokhov, M. Trupke, S. A. Tarasenko, A. Sperlich, P. G. Baranov, V. Dyakonov, and G. V. Astakhov, Phys. Rev. X **6**, 031014 (2016).

[145] C. J. Cochrane, J. Blacksberg, M. A. Anders, and P. M. Lenahan, Sci. Rep. **6**, 37077 (2016).

[146] A. Jarmola, V. M. Acosta, K. Jensen, S. Chemerisov, and D. Budker, Phys. Rev. Lett. **108**, 197601 (2012).

[147] N. Bar-Gill, L. M. Pham, A. Jarmola, D. Budker, and R. L. Walsworth, Nat. Commun. **4**, 1743 (2013).

[148] D. Simin, H. Kraus, A. Sperlich, T. Ohshima, G. Astakhov, and V. Dyakonov, Phys. Rev. B **95**, 161201 (2017).

[149] C. G. Yale, B. B. Buckley, D. J. Christle, G. Burkard, F. J. Heremans, L. C. Bassett, and D. D. Awschalom, Proc. Natl. Acad. Sci. U.S.A. **110**, 7595 (2013).

[150] R. Maboudian, C. Carraro, D. G. Senesky, and C. S. Roper, J. Vac. Sci. Technol. A **31**, 050805 (2013).

[151] B.-S. Song, S. Yamada, T. Asano, and S. Noda, Opt. express **19**, 11084 (2011).

[152] S. Dimitrijev, Microelectron. Eng. **83**, 123 (2006).

[153] P. G. Baranov, A. P. Bundakova, A. A. Soltamova, S. B. Orlinskii, I. V. Borovykh, R. Zondervan, R. Verberk, and J. Schmidt, Phys. Rev. B **83**, 125203 (2011).

[154] A. Gali, J. Mater. Res. **27**, 897 (2012).

[155] A. Csóré, N. Son, and A. Gali, Phys. Rev. B **104**, 035207 (2021).

[156] M. Widmann, M. Niethammer, D. Y. Fedyanin, I. A. Khramtsov, T. Rendler, I. D. Booker, J. Ul Hassan, N. Morioka, Y.-C. Chen, I. G. Ivanov, N. T. Son, T. Ohshima, M. Bockstedte, A. Gali, C. Bonato, S.-Y. Lee, and J. Wrachtrup, Nano Lett. **19**, 7173 (2019).

[157] V. Ivády, J. Davidsson, N. T. Son, T. Ohshima, I. A. Abrikosov, and A. Gali, Phys. Rev. B **96**, 161114 (2017).

[158] M. Wagner, B. Magnusson, W. Chen, E. Janzén, E. Sörman, C. Hallin, and J. Lindström, Phys. Rev. B **62**, 16555 (2000).

[159] A. Gali, M. Fyta, and E. Kaxiras, Phys. Rev. B **77**, 155206 (2008).

[160] A. Gali, M. Fyta, and E. Kaxiras, Phys. Rev. B **78**, 239902 (2008).

[161] J. P. Goss, R. Jones, S. J. Breuer, P. R. Briddon, and S. Öberg, Phys. Rev. Lett. **77**, 3041 (1996).

[162] A. Lenef and S. C. Rand, Phys. Rev. B **53**, 13441 (1996).

[163] P. Delaney, J. C. Greer, and J. A. Larsson, Nano Lett. **10**, 610 (2010).

[164] P. Kehayias, M. W. Doherty, D. English, R. Fischer, A. Jarmola, K. Jensen, N. Leefer, P. Hemmer, N. B. Manson, and D. Budker, Phys. Rev. B **88**, 165202 (2013).

[165] M. L. Goldman, A. Sipahigil, M. W. Doherty, N. Y. Yao, S. D. Bennett, M. Markham, D. J. Twitchen, N. B. Manson, A. Kubanek, and M. D. Lukin, Phys. Rev. Lett. **114**, 145502 (2015).

[166] M. L. Goldman, M. W. Doherty, A. Sipahigil, N. Y. Yao, S. D. Bennett, N. B. Manson, A. Kubanek, and M. D. Lukin, Phys. Rev. B **96**, 039905 (2017).

[167] C. Bhandari, A. L. Wysocki, S. E. Economou, P. Dev, and K. Park, Phys. Rev. B **103**, 014115 (2021).

[168] W. Dong, M. W. Doherty, and S. E. Economou, Phys. Rev. B **99**, 184102 (2019).

[169] T. Wimbauer, B. Meyer, A. Hofstaetter, A. Scharmann, and H. Overhof, Phys. Rev. B **56**, 7384 (1997).

[170] P. Giannozzi, S. Baroni, N. Bonini, M. Calandra, R. Car, C. Cavazzoni, D. Ceresoli, G. L. Chiarotti, M. Cococcioni, I. Dabo, A. D. Corso, S. de Gironcoli, S. Fabris, G. Fratesi, R. Gebauer, U. Gerstmann, C. Gougoussis, A. Kokalj, M. Lazzeri, L. Martin-Samos, N. Marzari, F. Mauri, R. Mazzarello, S. Paolini, A. Pasquarello,

L. Paulatto, C. Sbraccia, S. Scandolo, G. Sclauzero, A. P. Seitsonen, A. Smogunov, P. Umari, and R. M. Wentzcovitch, J. Phys. Condens. Matter **21**, 395502 (2009).

[171] I. Fdez. Galván, M. Vacher, A. Alavi, C. Angeli, F. Aquilante, J. Autschbach, J. J. Bao, S. I. Bokarev, N. A. Bogdanov, R. K. Carlson, L. F. Chibotaru, J. Creutzberg, N. Dattani, M. G. Delcey, S. S. Dong, A. Dreuw, L. Freitag, L. M. Frutos, L. Gagliardi, F. Gendron, A. Giussani, L. González, G. Grell, M. Guo, C. E. Hoyer, M. Johansson, S. Keller, S. Knecht, G. Kovačević, E. Källman, G. Li Manni, M. Lundberg, Y. Ma, S. Mai, J. P. Malhado, P.-Å. Malmqvist, P. Marquetand, S. A. Mewes, J. Norell, M. Olivucci, M. Oppel, Q. M. Phung, K. Pierloot, F. Plasser, M. Reiher, A. M. Sand, I. Schapiro, P. Sharma, C. J. Stein, L. K. Sørensen, D. G. Truhlar, M. Ugandi, L. Ungur, A. Valentini, S. Vancoillie, V. Veryazov, O. Weser, T. A. Wesołowski, P.-O. Widmark, S. Wouters, A. Zech, J. P. Zobel, and R. Lindh, J. Chem. Theory Comput. **15**, 5925 (2019).

[172] B. O. Roos, R. Lindh, P.-Å. Malmqvist, V. Veryazov, P.-O. Widmark, and A. C. Borin, J. Phys. Chem. A **112**, 11431 (2008).

[173] M. Johansson and V. Veryazov, J. Cheminform. **9**, 8 (2017).

[174] G. Kovačević and V. Veryazov, J. Cheminform. **7**, 16 (2015).

[175] K. Andersson, P.-Å. Malmqvist, B. O. Roos, A. J. Sadlej, and K. Wolinski, J. Phys. Chem. **94**, 5483 (1990).

[176] K. Andersson, P.-Å. Malmqvist, and B. O. Roos, J. Chem. Phys. **96**, 1218 (1992).

[177] N. Mizuochi, S. Yamasaki, H. Takizawa, N. Morishita, T. Ohshima, H. Itoh, and J. Isoya, Phys. Rev. B **68**, 165206 (2003).

[178] Q. Sun and G. K.-L. Chan, Acc. Chem. Res. **49**, 2705 (2016).

[179] S. Haldar, A. Mitra, M. R. Hermes, and L. Gagliardi, J. Phys. Chem. Lett. **14**, 4273 (2023).